Unclassified **EP 2001-**

Modelling Hot Fractured Rock systems.
Case study of Soultz-sous-Forêts HFR reservoir
by
D. Coumou

Reviewed by: C.K. Harris
Approved by: C.K. Harris
Date of issue: January 2001
ECCN number:

This report documents student work

SHELL TECHNOLOGY EP, RIJSWIJK

Further copies can be obtained from the Global EP Library, Rijswijk

SUMMARY

A seven months research has been performed to determine the modelling capabilities of the GEOCRACK [Swenson et al., 1997] finite element code and to make predictions on the performance of the HFR reservoir at Soultz-sous-Forêts (France).

Based on the 'Lauwerier' problem, a plane fracture in a infinite rock volume, two new analytic solutions are proposed. The first, including diffusion in the direction parallel to the fracture, has been tested for simple geometry's. Results show that, as expected, at low flow rates the solution deviates from the 'Lauwerier' solution up to 18% of the solution. The correctness of the new analytic formula has been proved by the far better fit with numerically (2D diffusion) generated data. A second analytic solution has been derived for a fracture with a finite extend. However, it is shown that its results violate the assumptions made.

GEOCRACK2D as well as GEOCRACK3D have been benchmarked successfully. The GEOCRACK3D generated curve fits the analytic 'Gringarten' solution exact. The mesh independence of the 2D code has been proved.

Some simple numerical experiments showed that the risk of short-circuiting in HFR-systems exists. This phenomena can, in some fracture geometry's, even result in thermal recovery of the production water. This has been observed in the thermal results of the 4 proposed models of the HFR reservoir at Soultz-sous-Forêts (Fr.).

Three 2D models, based on the general geology and micro-seismic data, representing the Soultz-sous-Forêts HFR-system, are proposed. Besides, a 3D 6-fracture model is constructed by extenuating fractures observed in the boreholes. Both 2D and 3D models assume the reservoir to be a closed system. The model results correlate well with the data generated with models by P. Audigane [Audigane, 2000].

Interpretation of the data, resulted in an estimation that the 1.1 MW_e production of the shallow reservoir would decrease to 0.6 MW_e after 20 years of production. A planned 3 well HFR system at 5 km depth would generate 5MWe at the start of production and 3.9 MW_e after 20 years.

Although GEOCRACK is still a work in process, it has proved to be a suitable modelling code for HFR systems.

TABLE OF CONTENTS

1. INTRODUCTION

1.1. What is HFR-energy?

For several centuries people have been using geothermal energy resources. Especially in volcanic regions the conventional geothermal energy potential is moderately large. Conventional geothermal energy is the exploitation of hot water from a near surface reservoir. We call this type of geothermal energy exploitation, hydrothermal energy. The energy can be used directly (heating) or it can be converted to electricity. World-wide, about 50 TWh of electricity is currently generated annually from hydrothermal reservoirs (total electricity production is about 13500 TWh). There is one serious limitation to the expansion of hydrothermal energy for electricity production; the low availability of naturally-occurring hydrothermal reservoirs. Reservoirs have to satisfy to a range of conditions; a shallow heat source, presence of water, sufficient permeability to allow for circulation of water between heat source and reservoir and a 'cap rock' seal. This is the reason that exploitable hydrothermal reservoirs are rather scarce throughout the world. Economic use has been confined to a few locations, generally those with active volcanism. Countries are Iceland, Italy and Greece in Europe, Indonesia, the Philippines and Japan in Asia and USA and Mexico in Northern America. In the USA geothermal electricity production is confined to four states; California, Nevada, Utah, and Hawaii, which is of course far from the US landmass.

Hot Fractured Rock (HFR) energy is an extension of the conventional hydrothermal energy described above, with far larger potential resources. However, HFR energy is not yet commercial. Scientists from the Los Alamos National Laboratory in New Mexico were the first to try the HFR-concept in the early 1970s. By circulating water between two wells, through a network of interconnected joints, one can extract the heat from a thermal reservoir. The reservoir-requirements are less restrictive than those needed for hydrothermal energy. Water does not have to be present and permeability can be stimulated. Only a high thermal gradient is necessary to decrease drilling depth and hence reduce the costs of the project to acceptable levels. These facts increase the potential of geothermal energy by orders of magnitude.

HFR energy requires the creation of a subsurface heat exchanger. By definition of an HFR resource, permeability values are far too low to allow significant fluid flow at reasonable over-pressures. To increase permeability, hydrofracturing, a well-known technique to improve oil-field performance, can be applied. The subsurface heat-exchanger created needs to be several thousands of cubic meters in volume with a fracture surface area of several square kilometers, to be of economic interest.

1.2. The Geothermal Team within Shell Technology E & P

The Geothermal Energy Team was set up at the start of 1998. Its main goal was to obtain insight into the geothermal market and to look for future opportunities in this area. The extensive untapped HFR resource was quickly identified as the one to focus on. Shell

supports the Kyoto process, which implies it made a commitment to take actions to reduce greenhouse gases. Further Shell is committed to 'Sustainable Development', which implies, among other things, an undertaking to minimize the impact of its activities on the environment. Geothermal energy can contribute to the realization of these good intentions.

Although presently the technology required to exploit HFR geothermal energy has not reached a commercial phase, a significant future is expected. The team activities focus on three areas; learn from past and present HFR pilot projects, identify potential cost reduction in the entire HFR lifecycle and to learn and understand the Geothermal Business. The Geothermal Team participates in the French-German HFR pilot project at Soultz-sous-Forêts. Of the ongoing HFR pilot projects, Soultz, situated in the Rhine Graben (northeastern France), is by far the most successful, mainly due to its large heat exchange surface area.

1.3. Geothermal Energy: The Market

As described in the first paragraph, potential HFR sites are widely spread. Huge areas in Europe (From France to Romania, Greece and Italy), Asia (Turkey, Afghanistan, Japan, Philippines, Indonesia), Africa (Ethiopia, Egypt, Eritrea, Sudan), Australia and New Zealand, as well as almost half of America, are suitable for HFR energy production. Besides, a growing concern about the use of fossil fuels will fuel the demand for more and more alternative and clean energy resources. Since HFR energy is free of the produce of any greenhouse gases, pollutants and waste materials, its future can be significant. From the known renewables, so far only wind energy seems to be competitive with carbon energy sources (around $55 /MWh). HFR exploitation incurs high capital costs since at least two wells are required and these usually need to be quite deep (drilling-expenses rise exponentially with depth). Besides HFR reservoirs are commonly found in hard granite rock, which make drilling costs even higher. Currently, drilling costs for HFR wells are, on an equal depth basis, over twice that of oil and gas. However it seems realistic that well-costs can be reduced by 50% over the coming years, according to Shell's Geothermal Energy Team. Further cost reductions can be made in the power plant costs and by improving the reservoir creation technology. Then, prices in the order of $50-$65 per MWh could be reached.

1.4. Soultz-sous-Forêts HFR-site

Currently there are five HFR pilot projects throughout the world. There are another two projects (Switzerland and Australia) in the planning stage. Table 1.4.1 compares the existing sites for a few key parameters. The most striking thing we see is the enormous relative volume of the Soultz stage 1 HFR reservoir. This is even more remarkable when we look at the low over-pressure needed, only 2 MPa. Another advantageous feature is the fluid recovery of 100%. The relatively deep depth and moderate temperatures are merely secondary features. Adding up these features makes Soultz the most promising of the HFR-sites nowadays.

Site	Period	z (km)	T (°C)	V (m³)	$P_{inj.}$(MPa)	Q (l/s)	Losses (%)	k
Fenton Hill 1 (US)	1974-1980	2.9	180	0.6×10^6	8	6	10	Low
Fenton Hill 2 (US)	1980-…	3.5	240	6.5×10^6	27	6	7	Low
Rosmanowes (UK)	1980-1989	2.6	90	3.5×10^6	10	25	20	Low
Hijori (Jap.)	1985-…	1.8	240	0.7×10^6	5	13	21	Strong
Ogachi (Jap.)	1989-…	1.0	200	1.3×10^6	7	8	75	Strong
Soultz 1 (Fr.)	1987-1999	3.5	150-160	240×10^6	2	24	0	Average
Soultz 2 (Fr.)	2000-…	5.0	200	?	?	?	?	?

Table 1.4.1: Comparison of current pilot project HFR-sites [Duchane, 1998].

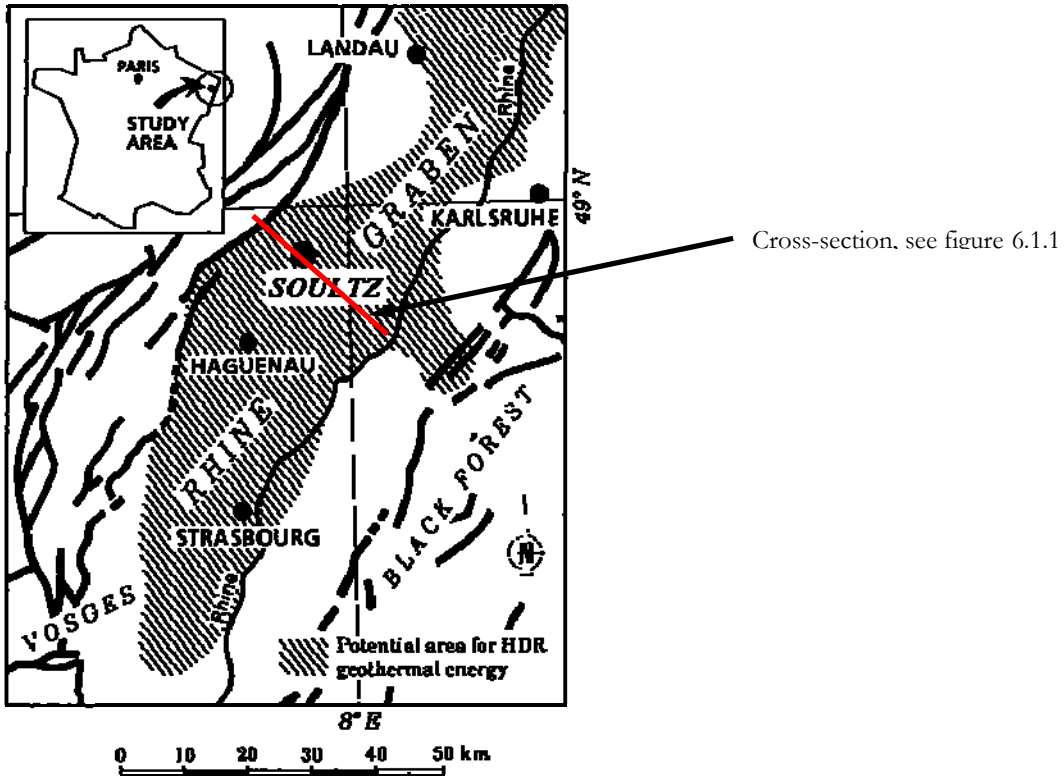

Figure 1.4.1: Location of Soultz in Rhine Graben

The HFR-site at Soultz is located in the northern part of the Rhine Graben. The observed anomalous temperature gradient [J. Bresee, 1992] (in the sediments more than 100°C per km.) is part of a large geothermal anomaly with an extension of 150 km by 20 km, covering French and German territory. The general geology is very well known thanks to centuries of oil-exploration (more than 250 years, making it the world's oldest oil-field). The existence of numerous wells in the vicinity, useful for seismic observations, contributed to the decision to carry out the experiments here.

The general geology is a typical Graben-structure, characterized by sub-vertical generally North-South trending faults. The cross-section (fig. 6.1.1) shows large sub-vertical faults, reaching to depths of 4 km, dipping either east or west.

1.5. Numerical modelling

In general HFR system are highly complex systems. Several physical processes happen simultaneously including the following:

- (Multi-phase) fluid flow (through porous rock, fractures and well bore) due to pressure difference.
- Conductive heat transport through rock.
- Conductive and convective heat transport through fluid.
- Heat exchange between rock and fluid.
- Chemical reactions (corrosion and scaling).
- Thermal contraction of rock.

All these processes occur in a highly heterogeneous medium. Because of this complexity, analytic solutions cannot provide detailed solutions, although they are useful for benchmarking numerical solutions. Analytic solutions are available for heat transfer but always make severe assumptions on geometry and physical processes.

In this research, I have made use of the finite element software GEOCRACK [Swenson et al., 1997]. GEOCRACK was specifically built for modeling HFR heat exchangers. It has been applied to the HFR-sites of Fenton Hill and Hijori [Swenson et al., 1999]. It incorporates of course pressure/fluid-flow calculations and heat transfer (convective and conductive). The feature that makes GEOCRACK especially useful for HFR-modeling is the incorporation of rock deformation due to thermal contraction. This is important as most of the fluid will travel through fractures in HFR systems due to the low overall permeability. These fractures will cool down much faster than other parts of the rock, influencing the stress regime through thermal contraction. During the first months of research, a GEOCRACK executable, which could only handle fracture flow, has been used. Later on a new executable including porous flow became available

1.6. Goals and objectives

One of the main objectives of the research is to determine whether GEOCRACK is a suitable and stable numeric code. This includes benchmarking it against existing analytic solutions for heat exchange. Further analytic solutions are derived, one that accounts for 2 dimensional heat transport through the rock and one that is based on a medium.of finite extend. The mesh dependency has been quantified using different meshes generated by different mesh generators.

Subsequently, GEOCRACK is applied to the 3.5-km deep HFR system at Soultz-sous-Forêts. It is being used to simulate the post-stimulation or production phase during a

extended period of operation (> 20 years). Results are compared with experimental data obtained during the circulation test of 1997 and with results from another numerical code. The 3D version of GEOCRACK (a beta-release) is successfully benchmarked. A 3D model, geometrically more realistic, is proposed and compared with the 2D models as well as a 3D numerical model proposed by Audigane [Audigane, 2000].

The experience gained by performing the above computations will be used to devise reservoir management strategies for the deep heat exchanger at Soultz sous Forêts.

2. THEORY

2.1. General formulation: The heat equation

The first law of thermo-dynamics states that the total change in energy inside a specified volume, is the result of the work done and the heat added during a certain time:

$$\frac{dE_{tot}}{dt} = \frac{dW}{dt} + \frac{dQ}{dt} \tag{1}$$

The term dQ/dt can be subdivided in a part describing internal heat production and a part describing the flux through the boundary of the volume:

$$\frac{dQ}{dt} = \int_V \rho H dV - \int_S q_j n_j dS \tag{2}$$

With H the density of heat sources in the medium, q the heat flux defined by:

$$q = -k\partial_j T \tag{3}$$

Equation (3) can be substituted in equation (2). Using the divergence theorem, we obtain:

$$\frac{dQ}{dt} = \int_V \left(\partial_j (k\partial_j T) + \rho H\right) dV \tag{4}$$

For the internal energy we can write (thermal energy plus dissipation of mechanical energy due to friction):

$$\frac{dE_{in}}{dt} = \int_V \sigma_{ij}\partial_j u_i dV + \frac{dQ}{dt} \tag{5}$$

The left part of equation (5) can be rewritten in the entropy-form. Further using that σ_{ij} (strain tensor) can be written in terms of the hydrostatic pressure:

$$\sigma_{ij} = -p\delta_{ij} + \tau_{ij} \tag{6}$$

will give us the following equation for the energy equation in T, p form:

$$\rho c_p \frac{dT}{dt} - \alpha T \frac{dp}{dt} = \tau_{ij} \partial_j u_i + \partial_j (k \partial_j T) + \rho H \tag{7}$$

The first term on the right side of equation (7) is the dissipative term that accounts for viscous dissipation effects. The second term on the right accounts for the diffusion of heat. The third term on the right side is the source term. The first term on the left is the transient term. The second term on the left is the adiabatic term This term accounts for adiabatic decompression due to pressure differences.

Equation (7) describes the transport of heat in both reservoir and fracture. Using equation (7) for a HDR environment allows us to reduce the formula substantially. We make the following assumptions:

- Neglect adiabatic decompression: Pressure difference are very low
- Neglect dissipative term: The fluid is expected to be non-viscous. This assumption is valid since the water is filtered each time it is recycled at the surface.
- Neglect source terms: The heat production due to radioactive decay is assumed to be negligible.

Equation (6) becomes:

$$\rho c \frac{dT}{dt} = \partial_j (k \partial_j T) \tag{8}$$

The time-dependence in the left-hand side can be written according to the Reynolds transport theorem:

$$\frac{dT}{dt} = \frac{\partial T}{\partial t} + v_j \partial_j T \tag{9}$$

The rock velocity is zero. Assuming that the conductivity k is constant, we obtain the following equations for the heat transport in rock and fluid in rectangular coordinates:

$$\frac{\partial T_r}{\partial t} = \frac{k}{\rho c} \left(\frac{\partial^2 T_r}{\partial x^2} + \frac{\partial^2 T_r}{\partial y^2} + \frac{\partial^2 T_r}{\partial z^2} \right) \tag{10}$$

$$\frac{\partial T_f}{\partial t} = -v \left(\frac{\partial T_f}{\partial x} + \frac{\partial T_f}{\partial y} + \frac{\partial T_f}{\partial z} \right) + \frac{k}{\rho c} \left(\frac{\partial^2 T_f}{\partial x^2} + \frac{\partial^2 T_f}{\partial y^2} + \frac{\partial^2 T_f}{\partial z^2} \right) \tag{11}$$

In the following paragraphs we discuss some analytic solutions of these differential equations. The numeric implementation of equations (10) and (11) is explained in chapter 3 *Theory on Geocrack*.

2.2. Analytic solutions

Several analytical solutions concerning fluid-rock heat exchange have been proposed since the 1950's. Due to the complexity of the problem, all of them have to make lots of geometric and physical assumptions. The book 'Stromung, Stoff- und Warmtetransport im Kluftgestein' Kolditz [Kolditz, 1997] gives an overview of what has been done on this subject. To obtain enough degrees of freedom, physical as well as geometrical assumptions have to be made. Geometries are generally, either 2D rectangular coordinates or 3D cylindrical coordinates, with symmetry in the horizontal plane. We intend to use the analytic solutions for benchmarking GEOCRACK2D, which uses rectangular 2D coordinates. For this reason it is more practical using geometries like figure 2.2.1.

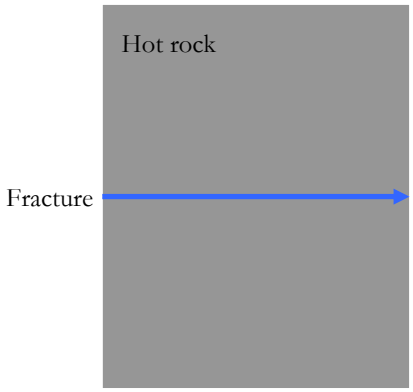

Fig. 2.2.1: System used by Lauwerier: Plane fracture in a finite 2D rock volume.

In 1955 Lauwerier [H.A. Lauwerier, 1955] presented a first solution describing this problem. He assumed 1-D heat diffusion through the rock perpendicular to the fracture plane and 1D heat advection through the fracture in an infinite half-space. I have adapted this solution in two different ways:

1st : Added 2D heat-diffusion in the rock.

2nd : Solution with a finite extent in the x direction.

These three analytic solutions will be described in the following three paragraphs. The last paragraph (§ 2.2.4) of this chapter describes the Gringarten [Gringarten,] solution. This analytic solution will be used to benchmark the 3D version of GEOCRACK.

2.3. Lauwerier solution

Lauwerier made the following assumptions

- 1-D linear flow through fracture

- 1-D heat advection through fracture
- 1-D heat diffusion through rock, orthogonal to fracture
- infinite half-space ($0 \le x < \infty$; $-\infty < z < \infty$)

The fluid-rock contact is at z = ½. The temperature is non-dimesionalised as follows:

$$T_D = \frac{T - T_0}{T_1 - T_0} \tag{12}$$

Here T_0 is the initial rock temperature, which is set to 0. T_1 is the inlet fluid temperature, which is set to 1. We convert all the other parameters to dimensionless values as well, denoted by the subscript D:

$$t_D = \frac{v}{b}t, \qquad x_D = \frac{x}{b}, \qquad z_D = \frac{z}{b}, \tag{13}$$

$$\alpha = \frac{\lambda^r}{c^r \rho^r}\frac{1}{bv}, \qquad \beta = \frac{\lambda^r}{c^w \rho^w}\frac{1}{bv}.$$

In fracture ($-b \le z \le b$) the temperature is assumed to be constant with z. At the fracture wall holds $T_{\text{Fluid}} = T_{\text{Rock}}$.

The heat equations (10 & 11) become:

$$\frac{\partial T_D}{\partial t_D} = \alpha \frac{\partial^2 T_D}{\partial z^2} \qquad x_D \ge 0, z_D > \frac{1}{2} \tag{14}$$

$$\frac{\partial T_D}{\partial t_D} = 2\beta \frac{\partial T_D}{\partial z_D} - \frac{\partial T_D}{\partial x_D} \qquad x_D \ge 0, z_D = \frac{1}{2} \tag{15}$$

In the Laplace domain these equation can be solved (see Appendix A.1) using the appropriate boundary conditions:

$$T_D(0, x_D, z_D) = 0, \qquad T_D(t_D, 0, \frac{1}{2}) = 1, \tag{16}$$

$$\lim_{x\to\infty} T_D(t_D, x_D, z_D) = 0, \qquad \lim_{z\to\infty} T_D(t_D, x_D, z_D) = 0.$$

$$\lim_{z\to 1/2-0} T_D(t_D, x_D, z_D) = \lim_{z\to 1/2+0} T_D(t_D, x_D, z_D)$$

By taking the Laplace transform, solve the solution and taking the inverse Laplace transform according to Carslaw & Jeager [Carslaw, 1960](see Appendix A.1), Lauwerier finds the following equation:

$$T_D = H(t_D - x_D)erfc\left\{\left\{\frac{\beta}{\sqrt{\alpha(t_D - x_D)}}\left[x_D + \frac{1}{2\beta}(z_D - \frac{1}{2})\right]\right\}\right\} \quad (17)$$

With H(t) the Heavyside function (≡ 0 if t < 0, 1 otherwise).

2.4. Isotropic diffusion in rock

The assumption of 1D heat diffusion perpendicular to the fracture plane (Lauwerier) is valid when isotherms in the rock are approximately parallel to the fracture plane. This is the case when large flow rates are present and/or the thermal anomaly is relatively small (i.e. not too close to the inlet). In HDR situations both conditions could be violated. Thus, an analytic solution with isotropic diffusion through the rock is useful. So far no analytical solutions have been proposed including x-diffusion, although according to Kolditz [Kolditz, 1997] this could influence the solution up to 11%. We can approximate this extra component in the heat equation with a perturbation expansion in which it is assumed that the thermal diffusion in the rock parallel to the fracture is small but non-zero. The assumptions made are:

- 1-D linear flow through fracture
- 1-D heat advection through fracture
- 2-D heat diffusion through rock, orthogonal to fracture
- infinite half-space ($0 \le x < \infty$; $-\infty < z < \infty$)

Again the equations can be solved in the Laplace domain. The exact computations can be found in Appendix A.2. We, however, have to remember that the solution contains a linearization in the x-diffusion component. The dimensionless solution becomes

$$T_D = T_L - H(t_D - x_D)\frac{\gamma}{\sqrt{\pi\alpha(t_D - x_D)^3}}\left(-\frac{\alpha}{4} + \frac{\gamma^2}{8(t_D - x_D)} + \beta\gamma + 2\beta^2(t_D - x_D)\right)\cdot e^{-\frac{\gamma^2}{4\alpha(t_D - x_D)}} \quad (18)$$

Where T_L stands for the temperature solution derived by Lauwerier (17) and $\gamma = 2\beta x + z - \frac{1}{2}$.

2.5. Finite extent in the x direction.

When you compare numerical results (e.g. GEOCRACK) with the classic Lauwerier-solution, you will see that near the domain boundaries the numerical results will deviate from the analytical ones. The zero-flux temperature boundary conditions in the numerical solution will force the temperature gradient towards zero as the boundary is approached. It is possible to derive an analytic solution with a finite extent in the x direction, containing a zero-flux boundary condition. The analytic curves will tend to a zero-gradient close to the boundary as well.

To do this we start with different heat equations:

$$\frac{\partial T_D}{\partial t_D} = \alpha \frac{\partial^2 T_D}{\partial z^2} \qquad x_D \geq 0, z_D > \frac{1}{2} \tag{19}$$

$$\frac{\partial T_D}{\partial z_D} = 2\beta \frac{\partial T_D}{\partial z_D} - \frac{\partial T_D}{\partial x_D} + \gamma \frac{\partial^2 T_D}{\partial x_D^2} \qquad x_D \geq 0, z_D = \frac{1}{2} \tag{20}$$

On comparing equation (20) with equation (15), we note that equation (20) allows for diffusion as well as advection of heat along the fracture. We use this equation to obtain an extra degree of freedom, which we have in the third term of the right-hand side of equation (20).

The boundary conditions implemented are the same as used by Lauwerier, except that the temperature does not go to zero when x goes to zero, but:

$$\left.\frac{\partial T_D}{\partial x_D}\right|_{x=L} = 0 \tag{21}$$

The equations (19 & 20) can be solved in the Laplace domain. Inversion to time requires a linearization, this is all described and explained in Appendix A.3. The final lengthy formula can be written out as follows:

$$
\begin{aligned}
T = {} & H(t-x)erfc\left(\frac{k_1}{2\sqrt{\alpha(t-x)}}\right) \\
& - H(t')e^{-\frac{L}{\gamma}}e^{-\frac{k_2^2}{4\alpha t'}}\left(\gamma\frac{k_2}{2\sqrt{\pi\alpha t'^3}} + \frac{2\gamma\beta}{\sqrt{\alpha\pi t'}} + \gamma^2\left(-\frac{3k_2}{2t'} + \frac{k_2^3}{4\alpha t'^2} - 4\beta + \frac{4\beta k_2^2}{2\alpha t'} + \frac{4\beta k_2}{\sqrt{\alpha}}\right)\right) \\
& + H(t'')e^{-\frac{k_3^2}{4\alpha t''}}e^{-\frac{L-x}{\gamma}}\left(\gamma\frac{k_2}{2\sqrt{\pi\alpha t''^3}} + \frac{2\gamma\beta}{\sqrt{\alpha\pi t''}} + \frac{\gamma^2}{2\sqrt{\alpha\pi t''^3}}\left(-\frac{3k_2}{2t''} + \frac{k_2^3}{4\alpha t''^2} - 4\beta + \frac{4\beta k_2^2}{2\alpha t''} + \frac{4\beta k_2}{\sqrt{\alpha}}\right)\right) \\
& - H(t''')e^{-\frac{2L-x}{\gamma}}\gamma^2\frac{e^{-\frac{k_3}{4\alpha t'''}}}{2\sqrt{\pi\alpha t'''}}G(t''')
\end{aligned}
\tag{22}
$$

With $G(t)$ given by:

$$
\begin{aligned}
G(t) = {} & \left(-c_2 + \frac{3c_4}{2t} - \frac{15c_6}{4t^2}\right) + k_4\left(-\frac{3c_1}{2t} + \frac{4\beta^2}{\alpha} + \frac{15c_3}{4t^2} - \frac{105c_5}{8t^3}\right) \\
& + k_4^2\left(\frac{c_2}{2\alpha t} - \frac{6c_4}{4\alpha t^2} + \frac{45c_6}{8\alpha t^3}\right) + k_4^3\left(\frac{c_1}{4\alpha t^2} - \frac{5c_3}{4\alpha t^3} + \frac{105c_5}{16\alpha t^4}\right) \\
& + k_4^4\left(\frac{c_4}{8\alpha^2 t^3} - \frac{15c_6}{16\alpha^2 t^4}\right) + k_4^5\left(\frac{c_3}{16\alpha^2 t^4} - \frac{21c_5}{32\alpha^2 t^5}\right) \\
& + k_4^6\left(\frac{c_6}{32\alpha^3 t^5}\right) + k_4^7\left(\frac{c_5}{64\alpha^3 t^6}\right)
\end{aligned}
\tag{24}
$$

and :

$$
\begin{aligned}
k_1 &= z - \frac{1}{2} + 2\beta x & t' &= t - (2L + x) \\
k_2 &= z - \frac{1}{2} + 2\beta x + 4\beta L & t'' &= t - (2L - x) \\
k_3 &= z - \frac{1}{2} - 2\beta x + 8\beta L & t''' &= t - (4L + x)
\end{aligned}
\tag{23}
$$

The four ‘c’ functions are all dependent of α, β and γ (see Appendix A3, equations A63 – A66)

2.6. Gringarten solution

During the research a suitable 3D version of the numeric code used became available. For benchmarking this 3D code the Gringarten solution [Gringarten & Sauty, 1975] can

be used. The system consists of a plane fracture with a source and sink (two wells) in a 3D infinite rock volume. In the fracture 2D advection is allowed and in the rock only 1D diffusion and no porous flow. Some authors, e.g. Kolditz [Kolditz, 1997], call this solution the 2½ D solution.

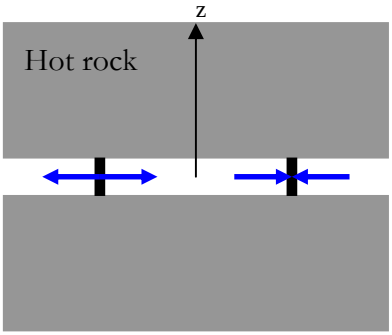

Fig. 2.2.4.1: System by Gringarten.

The heat equations (9 & 10) become:

$$\frac{\partial T_D}{\partial t_D} = \alpha \frac{\partial^2 T_D}{\partial z_D^2} \qquad z_D > \frac{1}{2} \tag{25}$$

$$\frac{\partial T_D}{\partial t_D} = 2\beta \frac{\partial T_D}{\partial z_D} - v_D^2 \frac{\partial T_D}{\partial \phi_D(x_D, y_D)} \qquad z_D = \frac{1}{2} \tag{26}$$

The parameters can be made dimensionless in the following way:

$$t_D = \frac{Q}{b^3} t, \quad x_D = \frac{x}{a}, \quad y_D = \frac{y}{a}, \quad z_D = \frac{z}{a}, \quad \phi_D = \frac{1}{2} \ln \frac{(x_D+1)^2 + y_D^2}{(x_D-1)^2 + y_D^2} \tag{27}$$

$$\psi_D = \arctan\left(\frac{2y_D}{1 - x_D^2 - y_D^2}\right), \quad \alpha = \frac{\lambda^r b}{c^r \rho^r Q}, \quad \beta = \frac{\lambda^r b}{c^w \rho^w Q},$$

$$v_D^2 = \frac{b^2}{2\pi a^2} \left\{ \left[\frac{x_D+1}{(x_D+1)^2} - \frac{x_D-1}{(x_D-1)^2 + y_D^2} \right]^2 + \left[\frac{y_D}{(x_D+1)^2} - \frac{y_D}{(x_D-1)^2 + y_D^2} \right] \right\}$$

Where *a* is half the distance between injection and production well. The boundary conditions of the problem are:

$$T_D(0, x_D, y_D, z_D) = 0, \qquad T_D(t_D, -1, 0, 0) = 1, \tag{28}$$

$$\lim_{x_D^2 + y_D^2 \to \infty} T(t_D, x_D, y_D, z_D) = 0, \quad \lim_{z_D \to \infty} T(t_D, x_D, y_D, z_D) = 0,$$

$$\lim_{z_D \to 1/2 - 0} T(t_D, x_D, y_D, z_D) = \lim_{z_D \to 1/2 + 0} T(t_D, x_D, y_D, z_D)$$

With (28), the following solution for T_D can be found, which looks similar as the Lauwerier (17) solution except for the integral I_D:

$$T_D = u(t_D - I_D)erfc\left\{\left\{\frac{\beta}{\sqrt{\alpha(t_D - I_D)}}\left[I_D + \frac{1}{2\beta}(z_D - \frac{1}{2})\right]\right\}\right\} \tag{29}$$

I_D is given by the integral:

$$I_D(\phi_D, \psi_D) = \int_{-\infty}^{\phi_D} \frac{d\phi_D}{v_D^2} \tag{30}$$

This integral can be solved analytically. For $y_D = 0$ the solution becomes:

$$I_D(\phi_D, \psi_D) = \frac{2\pi a^2}{3b^2}\left\{1 - \frac{\sinh\phi_D}{\cosh\phi_D + 1}\left(1 + \frac{1}{\cosh\phi_D + 1}\right)\right\} \tag{31}$$

3. THEORY BEHIND GEOCRACK

3.1. Numerical Modelling of HFR Reservoirs

Numerous physical processes occur simultaneously in an active HFR reservoir. Uncertainty surrounds ad-hoc predictions about reservoir lifetime, thermal drawdown etc. Analytic analyses are far too simplistic to represent reservoirs in detail, so numerical models are crucial. Since the 1980s several numerical codes have been proposed with different capabilities. An ideal numerical code would have the following list of capabilities:

- Heat diffusion and advection in porous as well as fractured media.
- Multi-phase fluid flow.
- Explicit representation of fractures.
- Channeling of flow in fractures.
- Changes in fracture aperture due to changes in the stress-field and the hydraulic pressure.
- A relationship between fracture aperture and fracture conductivity (inclusion of wall roughness and non-Darcy flow).
- Thermal contraction of rock, causing fracture aperture changes.
- Rock/water chemical interactions
- Tracer transport.

So far there is no numerical model which includes all these features. The GEOCRACK2D finite-element code was developed to solve coupled thermal, hydraulic and mechanical problems where the flow is in fractures. From the above capabilities, GEOCRACK2D currently does *not* account for:

- Multi-phase fluid flow.
- Non-Darcy flow.
- Chemical interactions.

A porous matrix version became available four months into the present project. Until that time a version without the possibility to implement matrix porosity has been used. A 3D version is also available, which is also crucial for a detailed representation of a HDR reservoir.

3.2. Theory and Implementation

The GEOCRACK2D finite-element model consists of continuum elements (representing rock), fluid elements (representing fluid flow in fractures) and interface elements (representing the joint stiffness) [Swenson et al, 1997].

3.3. Structural Model

The continuum elements are derived using standard elasticity practice [Hughes, 1987]. The assembled element contributions result in the following matrix equation:

$$\mathbf{K_S u} = \mathbf{f} \tag{32}$$

In which $\mathbf{K_S}$ is the structural stiffness matrix, **u** the nodal displacement and **f** is the global force vector, the load on the structure. Interface elements are used to describe the non-linear relationship between fracture opening and fracture stress (Gangi):

$$a = a_0 - a_{disp.} = a_0 - a_0\left(\frac{\sigma}{\sigma_c}\right)^m \tag{33}$$

In equation (33) a_0 is the zero-stress fracture opening, σ is the effective stress and σ_c a critical stress at which the fracture is assumed to be closed, and m is a constant (Gangi constant).

3.4. Fluid Flow Model

In a fracture the fluid is assumed to be one-dimensional (planar), given by the cubic-law:

$$q = \frac{a^3 w}{12\mu L}\Delta P = k_p \frac{w}{L}\Delta P \tag{34}$$

Here w is the width, a the aperture (equation (33)), μ the viscosity, L the length of the fracture and ΔP the pressure difference between the start and end point of the fracture. This is actually the same equation as *Ohm's Law* in electrodynamics. ΔP corresponds to the potential difference, q to the electric current and the right-hand side pre-factor to the conductance (= inverse resistance). In a network of interconnecting fractures, the flow through the whole network can be calculated in the same way as the current through an electric circuit.

Further the fluid is assumed incompressible:

$$-\frac{\partial q}{\partial x} = \frac{\partial a}{\partial t} \tag{35}$$

Substituting equation (34) into equation (35) gives:

$$\frac{\partial}{\partial x}\left(k_p \frac{\partial p}{\partial x}\right) = \frac{\partial a}{\partial t} \tag{36}$$

The global matrix equations become:

$$\mathbf{K_p p} = \mathbf{q} - \mathbf{S}\frac{\partial \mathbf{a}}{\partial \mathbf{t}} \tag{37}$$

Where $\mathbf{K_P}$ is the fluid permeability matrix, $\mathbf{p}$ is the nodal pressure vector, $\mathbf{q}$ is the flow-rate vector, $\mathbf{S}$ the fracture opening storage matrix, and $\partial\mathbf{a}/\partial$t is the fracture-opening velocity vector.

3.5. Heat-Transfer Model

In the rock, heat transport is conductive. The energy equation (11) in a two-dimensional medium, which velocity can be neglected, becomes:

$$\frac{\partial T}{\partial t} = \frac{k}{\rho c_p}\left(\frac{\partial^2 T}{\partial x^2} + \frac{\partial^2 T}{\partial z^2}\right) \tag{38}$$

c_p and ρ are respectively specific heat and density of the rock. In the fluid, the heat-equation becomes (one-dimensional heat transport including convection):

$$k\frac{\partial}{\partial x}\left(a\frac{\partial T}{\partial x}\right) - \rho v c_p \frac{\partial T}{\partial x} + h\left(T_{S1} + T_{S2} - 2T\right) = \rho a c_p \frac{\partial T}{\partial t} \tag{39}$$

Where T_{Sx} is the structure temperature at the two bounding surfaces and T the fluid temperature. h is the convection coefficient. Using the standard finite-element procedures, two sets of equations are obtained for the structure and the fluid:

$$[\mathbf{K_S^{th}} + \mathbf{H_S} + \mathbf{C_S}]\mathbf{T_S} - \mathbf{H_S T_{Fh}} = \mathbf{C_S T_S^{prev}} \tag{40}$$

$$[\mathbf{K_F^{th}} + \mathbf{2H_F} + \mathbf{C_F} + \mathbf{E_F}]\mathbf{T_F} - \mathbf{H_F T_{Fh}} = \mathbf{C_F T_F^{prev}}$$

Where **K** is the conductivity, **H** represents the transfer of heat between rock and fluid, **C** is heat-capacity matrix and **T** is the node-temperature vector. The superscript 'prev' indicates the values at the previous time step.

3.6. Coupling of Three Model Equations

The equations (32) and (37) of the structure and fluid model, are interconnected in the way that joint displacement affects the fluid solution ($\mathbf{K}_p(\mathbf{u})$ and $\partial\mathbf{a}/\partial t(\mathbf{u})$), and the fluid solution then applies a different load on the structure ($\mathbf{f}(\mathbf{p})$). These equations are therefor solved simultaneously using an iterative procedure. For the structure, the functions to be zeroed are the summation of forces on each structural node. For the fluid, the total flow at a node has to be zeroed. This is done using a Newton-Raphson scheme:

$$\begin{bmatrix} \frac{\partial \sum \mathbf{f}}{\partial \mathbf{u}} & \frac{\partial \sum \mathbf{f}}{\partial \mathbf{p}} \\ \frac{\partial \sum \mathbf{q}}{\partial \mathbf{u}} & \frac{\partial \sum \mathbf{q}}{\partial \mathbf{p}} \end{bmatrix} \begin{bmatrix} \frac{\Delta \mathbf{u}}{\Delta \mathbf{p}} \end{bmatrix} = -\begin{bmatrix} \frac{\sum \mathbf{f}}{\sum \mathbf{q}} \end{bmatrix} \tag{41}$$

With $\frac{\partial \sum \mathbf{f}}{\partial \mathbf{u}} = \mathbf{K}_S$ and $\frac{\partial \sum \mathbf{q}}{\partial \mathbf{p}} = \mathbf{K}_p$. The other two submatrices are the so-called coupling matrices. The right-hand side matrix is iteratively zeroed.

When convergence is reached in the Newton-Rhapson scheme described above, the parameters of the structure and fluid flow model are passed on to the temperature model. Conversely the calculated temperature affects the fluid density, viscosity and the structure thermal contraction.

4. ANALYTIC RESULTS

4.1. Isotropic versus anisotropic diffusion

In the theory a suitable analytic solution for isotropic diffusion has been presented (§2.2.2). This solution is an extension of the solution proposed by Lauwerier [Lauwerier, 1955] which assumes zero diffusion in the direction of the fracture. In this section these two analytic solutions will be compared. Further, they will be compared with numerical results from GEOCRACK2D.

In figure 4.1.1, results obtained from Swenson [Swenson et al., 1997] are plotted; numerical results from GEOCRACK2D (black dotted lines) and analytic results (black solid lines). For flow rate coefficients of 0.1 m^3/day, the analytic isotropic solution (red) and anisotropic solution (green) are plotted as well. Note at first that my version of the 'Lauwerier' solution (green line) does not coincide with the analytic solution from Swenson, who claims to use the same analytic solution. The reason for this remains unclear, but the exact fit of Swenson's analytic solution with the numeric results of the anisotropic diffusion solutions is surprising as the analytic equation assumes an infinite half space. Further we see that the isotropic (red) curve fairly well approaches the GEOCRACK2D isotropic results. Until about 12000 days (32 years) the fit is even exact. We see that the difference between isotropic and anisotropic solution can build up to 40^0C after 30.000 days, which corresponds to a percentage of 16%. This is in rough correspondence with the 11% derived by Kolditz [Kolditz, 1997] for a slightly different geometry. We now shall further quantify the behaviour of the new analytic solution.

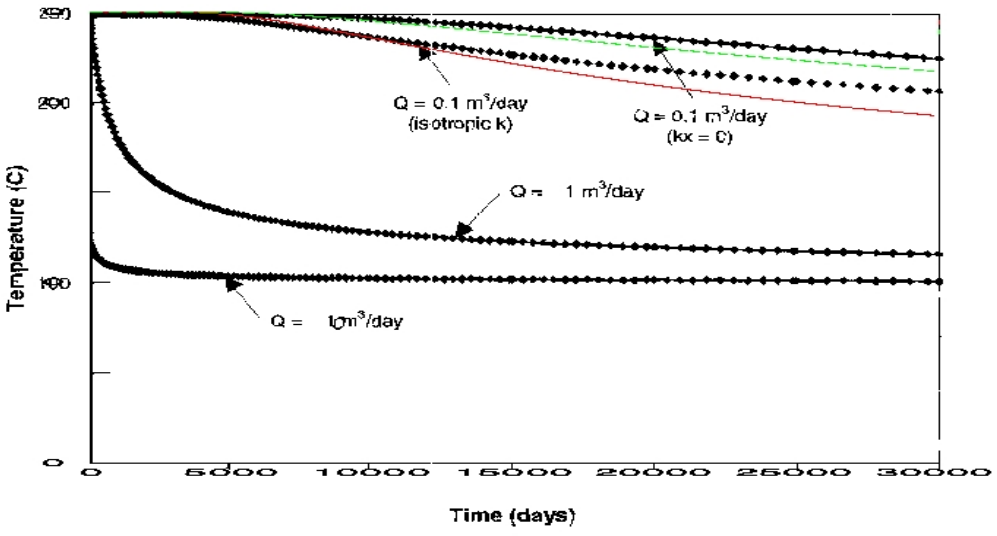

Fig. 4.1.1: Picture from Swenson et al. [Swenson et al., 1997] with superimposed the anisotropic (green) and isotropic (red) analytic solutions. Dotted black lines are produced by GEOCRACK. Solid black lines are analytic solution from Swenson et al.

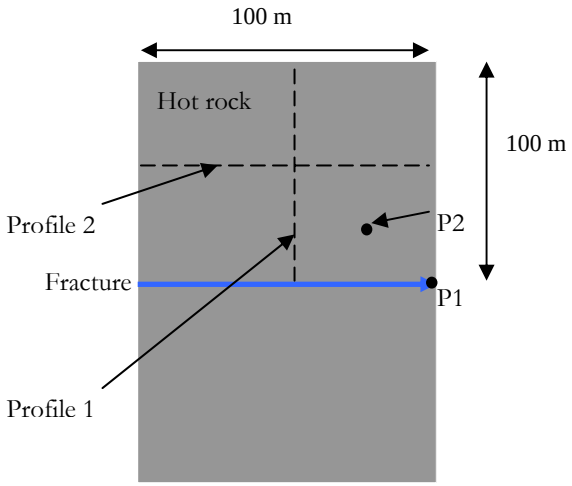

Fig. 4.1.2: Geometry used by Lauwerier.

The influence of diffusion in the x direction is a strong function of the flow rate. High flow rates cause the influence of the diffusion in x direction to diminish. The geometry depicted in figure 4.1.2 has been used to carry out several experiments. The temperature decline in location P1 has been tested for different (constant) flow rates. Figure 4.1.3 shows the difference between isotropic and anisotropic diffusion solutions after 25000 days for three locations. Only for flow rates up to 0.8 m^3/day (= 0.01 l/s) the difference is evident with peaks around 0.1 m^3/day. At these low flow rates the difference between isotropic and anisotropic is in the order of 10% (fig. 4.1.4). In HDR environment flow rates are in the order of tens to hundreds of litres per second, far larger than flow rates shown in figures 4.1.3 and 4.1.4. However, the fluid will be divided among several fractures in a HDR system, possibly reducing the flow per fracture to the range where lateral diffusion is contributing a significant part to the heat transfer.

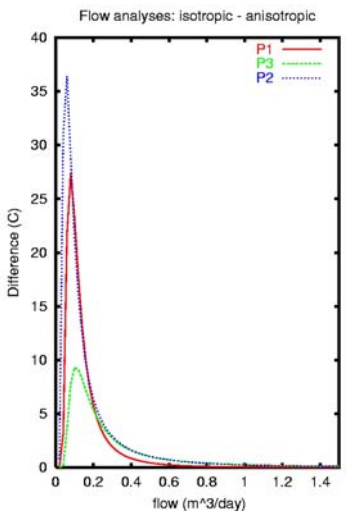

Fig. 4.1.3: Influence of flow rate (t = 25000 days)

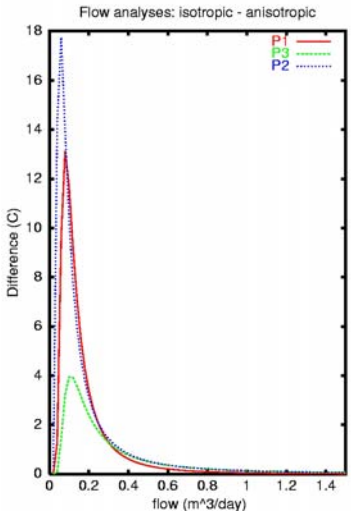

Fig. 4.1.4: Influence of flow rate (%) (t = 25000 days)

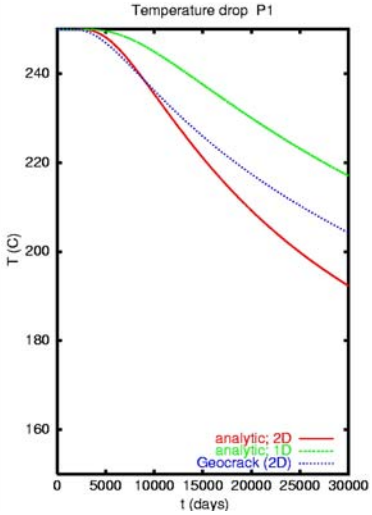

Fig. 4.1.5: Temperature decay of location P1 (outlet).

The curves in figures 4.1.3 and 4.1.4, will go to infinity if we approach a zero flow rate when we would look at infinite great times. The fact that it does not show this asymptotic behaviour in the plots is caused by the heavysight functions in both analytical solutions.

Further tests are carried out using a flow rate of 0.1 m^3/day. Analytic temperature decline curves of locations P1 and P2, and the two temperature cross-sections curves are compared with numerical data. The mesh shown in Appendix C, figure C4, has been used to generate numerical data. Element size increases linearly from 1.7m to 8.3m perpendicular to the fracture and decrease linearly from 8.3m to 4.2m towards the vertical boundaries. The results of these tests are given in figures 4.1.5 till 4.1.8.

The temperature decline curves of the isotropic solution match the GEOCRACK solutions better (figures 4.1.5 & 4.1.6). On the other hand, it is remarkable how the isotropic (red) and GEOCRACK (blue) solution diverge after 10000 days. We observe of course exactly the same in figure 4.1.1. Boundary effects within GEOCRACK could be the cause. This is confirmed by the fact that the numeric and 2D-diffusion analytic temperature decline curves of P2 (figure 4.1.6), lying 25m from the boundaries match each other much better than the curves of P1 (figure 4.1.5), lying on the right boundary.

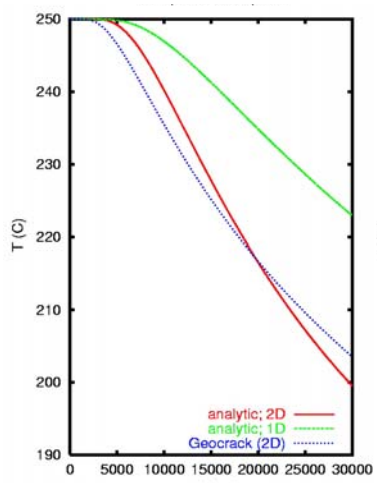

Fig. 4.1.6: Temperature P2.

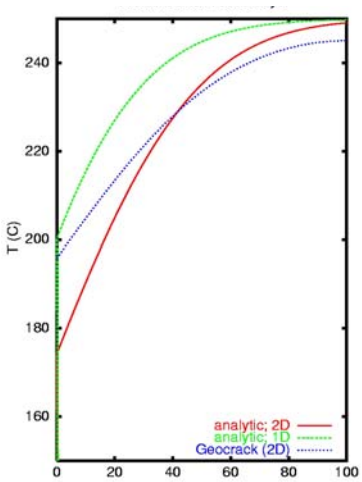

Fig. 4.1.7: Temperature profile 1.
x = 60m, t = 15000days

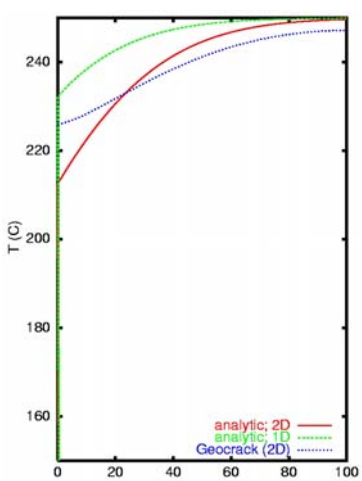

Fig 4.1.8: Temperature profile 2.
z = 50m, t = 15000days

Figure 4.1.7 shows the temperature change in the direction perpendicular to the fracture after 15000 days. The final graph plots the temperature profile in the lateral direction at a normal distance of 60m from the fracture, after 15000 days. In both plots, the new analytical solution better fits with the numerical solution. The fit is still not exact. This is probably caused by the different boundary conditions used for the numerical and analytical data. The numerical solution has a symmetry boundary condition at x = 0 and a zero heat flux at x = 100m (see figure 4.1.8) The analytic solutions assume an infinite half space. This is further discussed in the next paragraph.

In general we can say that the new analytic solution is an improvement especially for low flow rates.

4.2. Finite Space Analytic Solution

Numerical solutions always make use of a finite solution space. GEOCRACK uses Neumann boundary conditions on the vertical boundaries:

$$\partial T / \partial x = 0 \qquad x = 0 \cup x = L$$

L is the extent of the system in the x direction. This results in the flattened edges of x-profile temperature curves. On the other hand, the analytic solution addressed by Lauwerier, assumes an infinite space. As it is impossible to compute an infinite space numerically, I have looked for a finite analytic solution. This finite solution has a zero temperature gradient at the right boundary of the system ($x = L$). The mathematics involved are explained in the theory (§ 2.2.3 and Appendix A3).

In figures 4.2.1 and 4.2.2, the finite analytic solution and infinite analytic solution are compared. Both figures are of the same 10-meter-geometry ($L = 10m$), and show the temperature along a fracture. No obvious differences can be seen on the 10-metre scale (fig 4.2.1). Only if we zoom in on the right boundary (figure 4.2.2. Note x-axis scale!) we can see that the finite analytic temperature gradient tends to zero at the edge. It is obvious that the influence of the boundary conditions is of minor importance. The magnitude of $\frac{\partial^2 T}{\partial x^2}$ (curvature) is very large near the boundary. This is in contradiction with the assumptions made that diffusion parallel to the fracture is negligible. Future analytic work could include the combination of finite extend and isotropic diffusion.

As the boundary effects hardly affect the solution (influence in the order of a few millimetres) there is no use comparing this solution with the numerical data.

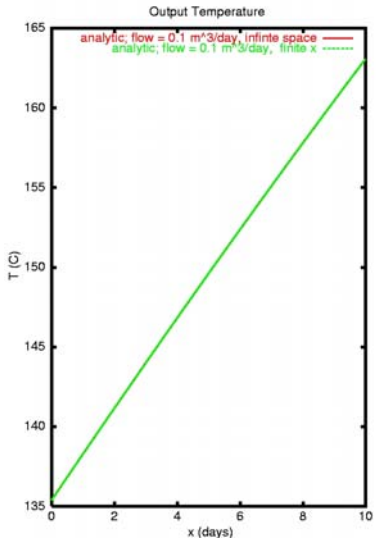

Fig. 4.2.1: Temperature along fracture.

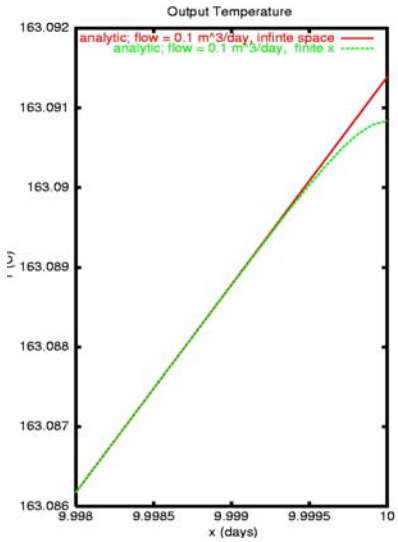

Fig. 4.2.2: Zoomed in on right boundary.

4.3. Soultz-sous-Forêts analytic analysis

As a first approximation, the subsurface heat exchanger at Soultz-sous-Forêts can be represented using a single fracture. According to data given by Steve Oates [S. Oates,

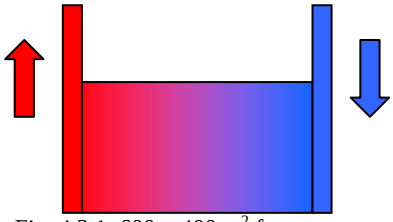

Fig. 4.3.1: 600 × 400 m^2 fracture.

2000], this fracture would have a length of 600m and a hight of 400m. Further data can be found in table 4.2.1. For a moderate energy production flow rates around 30 l/s are needed. As we see in figure 4.3.2, such a flow rate would drop the production temperature to 100^0C in less than four years. On the other hand we might have several parallel heat exchanger like the one showed in figure 2. In that case each fracture only produces a small part of the total production. For lower flow rates the temperature drop is far less. With a flow of 15 l/s, the production temperature does not drop to 100^0C until 16 years. Figure 4.3.3 shows temperature drops of even lower flow rates. For Flow rates of 10 l/s, even after 12000 days (32 years) the temperature has not dropped below 100^0C. A production of 2 l/s results in a constant heat exchanger; as much heat is supplied through the rock as is carried off with the water.

One would think that the assumption of 1D-diffusion is not valid with these low flow rates. It has been tested however that this effect is minimal; less than 1^0C after 30000 days. The reason for this will be discussed in the paragraph on Anisotropic / isotropic diffusion.

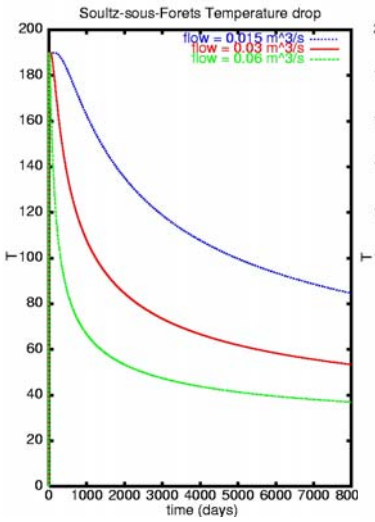

Fig. 4.3.2: Analytic T decay Soultz-sous-Forêts.

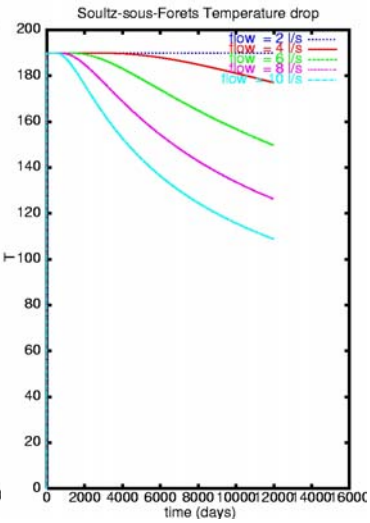

Fig. 4.3.3: Low flow rates

Fracture length = 600 m
Fracture height = 400 m
flow rate = see plot
fracture aperture = 0.001 m
density of rock = 2.66 E3 kg/m^3
density of water = 950 kg/m^3
specific heat water = 4300 $JK^{-1}Kg^{-1}$
specific heat rock = 1100 $JK^{-1}Kg^{-1}$
water inlet Temperature = 20°C
in situ Temperature of rock = 190°C
Thermal conductivity = 2.58 $Wm^{-1}K^{-1}$
Thermal diffusivity = 0.89×10^{-6} m^2/s

Table 4.3.1: Parameters.

5. GEOCRACK 2D/3D, BENCHMARKS AND TESTS

5.1. Numerical issues

When applying a numerical integration method, several problems can occur. Their causes can be threefold:

1. Stability: A numerical scheme is called unstable when errors increase at every iteration step without bound. Small errors in the steady state solution can grow dramatically in the transient solutions. To prevent instability the largest eigenvalue in the error-propagation matrix should be smaller than 1. Further the timestep (Δt) must be smaller than a certain amount, dependent on the spatial discretisation (Δx) and the fluid velocity (V):

$$Co = \frac{V\Delta t}{\Delta x} \leq 1$$

   Co is the Courant number, which is physically interpreted as the ratio of the advective distance during one time step to the spatial discretisation. A fluid particle may not travel beyond a full rock element in one time step.

2. Convergence: A scheme is said to be convergent when it is not only stable but also consistent. This means that the difference between numerical and analytic solution can be made arbitrarily small by choosing a sufficiently small transient and spatial discretisation.

3. Numerical dispersion: The approximations of first-order derivatives generate errors in the order of second-order derivatives. These add up with the hydrodynamic dispersion (also 2nd order derivative) and are thus called numerical dispersion. For an implicit (backwards) iteration scheme the numeric dispersion coefficient is:

$$D_{num} = V\frac{\Delta x}{2} + V^2\frac{\Delta t}{2}$$

   The numeric dispersion coefficient varies with iteration scheme, but it is always dependent on velocity V and spatial and temporal discretisations Δx and Δt. The remedy to reduce the effect of numerical dispersion is to make Δx and Δt smaller. When the total dispersion (numerical + hydrodynamic) is negative, the solution may exhibit unphysical oscillations, leading to over- and undershoot.

5.2. Mesh Dependency of GEOCRACK

Simple tests have been performed to obtain an impression of the mesh dependency of GEOCRACK2D. A single plane fracture problem has been solved with six meshes with different element size, ranging from 1m to 20m (total length of the fracture). The mesh with element size 2 (h = 2m) is shown in figure C6 (Appendix C). Three points, P1, P2 and P3, are measured, located respectively on the fracture at 10m from the inlet, on the fracture at 20 m from the inlet and P3 located 10 m above the fracture on a line crossing the fracture with a straight angle at 10 m. Besides these points, the numeric results of a cross-section perpendicular to the fracture at 10m from the inlet are compared.

The flow through the fracture is constant, initial rock temperature is 250 ^{0}C and the inlet water temperature is 100 ^{0}C. The numerical results of the different meshes with different element sizes are compared with each other. First of all the temperature decline curves of points P1, P2 and P3, given respectively in figures 5.2.1, 5.2.2 and 5.2.3. Although in graphs 5.2.1 and 5.2.2 the analytic function (isotropic diffusion in infinite half space) is plotted, a comparison between this analytic solution and the numerical solutions is difficult; all numerical temperature curves decay more slowly than the analytic. This is in agreement with curves from chapter 4, e.g. figure 4.1.1, 4.1.5 and 4.1.6. Up to mesh element sizes of 4m, the numeric results compare reasonably well, for all temperature drawdown curves. Above 4m-element size, curves are not smooth anymore. These curve show a slower temperature drop in early times (up to 50 days), after which the temperature drops below the curves generated with the finer meshes. The horizontal component of the stress (figure 5.2.4) is calculated correctly up to meshes with a size of 6.7 m. This test has been performed with very low velocities to be sure not to violate the *Courant*-criterium. Δt has been chosen sufficiently fine as well.

Element size (m)	Cal. Time of 1 iteration(s)	Cal. Time 1 year (min.) on a SUN UltraSparc 333MHz
2	0.33	15
4	0.06	2.5
10	0.01	0.4

Table 5.2.1: Increased calculation time with decreasing mesh size

I have also tested GEOCRACK with larger meshes. Meshes with a geometry (100x200m) in the range of HDR-reservoirs have been used (see figure C5). Figures 5.2.5 and 5.2.6 show respectively cross-sections in the x and z direction. Figure 5.2.5 shows a cross-section parallel to the fracture at a distance of 10 m after 7000 days. The flatness of the graphs near the borders is caused by symmetry boundary conditions. The analytic solution in contrary makes use of an infinite space. This difference between analytic and numeric solution is addressed sections 4.3. It is remarkable how much better the fit is of mesh 'l1' (red curve), especially when noted that this mesh asks only about a third of the calculation time needed for 'l2' (green curve). The reason must be the mesh refinement of mesh 'l2' near the fracture. In figure 5.2.6 a cross-section in vertical direction,

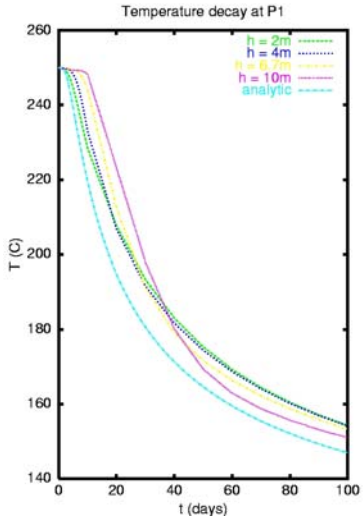

Fig. 5.2.1: Temperature P1.

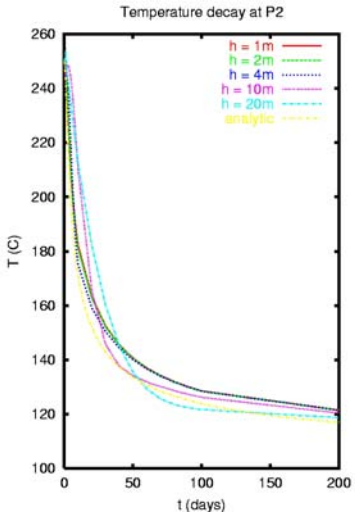

Fig. 5.2.2: Temperature P2.

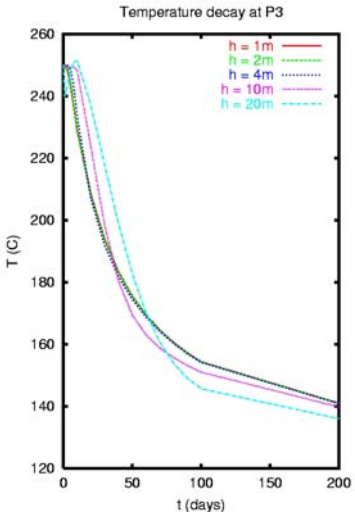

Fig. 5.2.3: Temperature P3.

through the source (x=0) after 7000 days, is shown. Both numerical solutions show good comparison with the analytic solution.

Further I have done tests with a contracting rock environment. According to Swenson [Swenson, 1997b] this phenomena seems to play an important role. Due to the cooling and contraction of the rock, the fractures widen. Figures 5.2.7 gives output temperatures of this test. Errors are of the same order as without contraction (note the scale difference). This is illustrated by figure 5.2.9. This figure shows the increase of the fluid volume in the crack. This is a measure of the contraction of the rock and the accompanying widening of the fracture. The fit between the two numerical solutions is exact, from which we can conclude that calculations on structure displacement are far less mesh dependent.

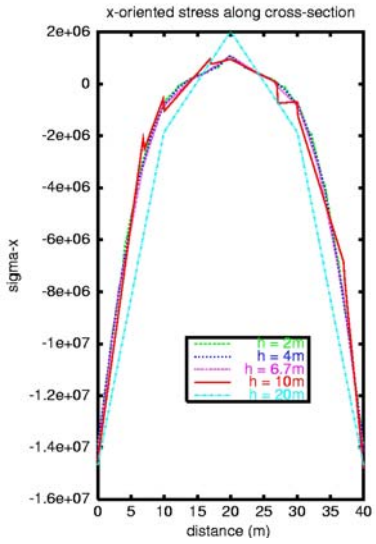

Fig. 5.2.4: Stress regime.

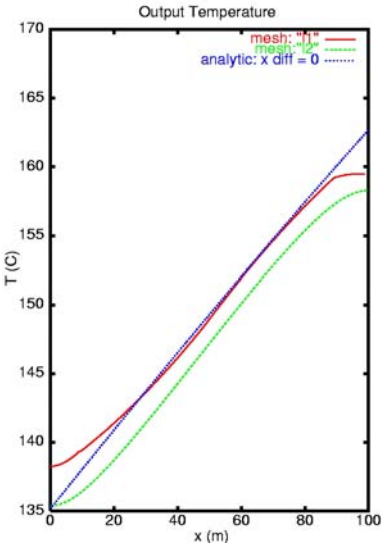

Fig. 5.2.5: Temperature, z = 10 m.

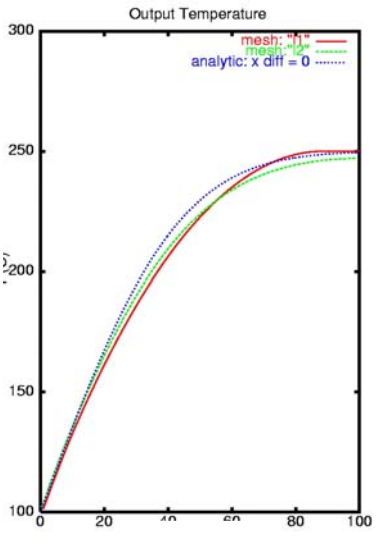

Fig. 5.2.6: Temperature, x = 0 m.

Mesh 'l1' is generated with the mesh generator 'level3_mesh_exe'. This mesh generator generates brick-wall structured fracture systems, with mesh refinement at the fractures. It was built to represent typical HDR-environments. Mesh 'l2' is generated with 'CASCA', another more general mesh generator, with more possibilities. Some experience with the meshes taught that, in general, the meshes generated with 'level3_mesh_exe' are more

stable and require less computation time. The problem with the CASCA-meshes is that fluid-elements have to be added in GEOCRACK, which (sometimes) leads to problems (see Appendix E).

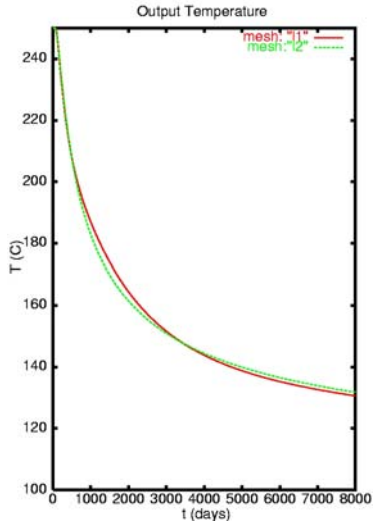

Fig. 5.2.7: T decay, no thermal contraction.

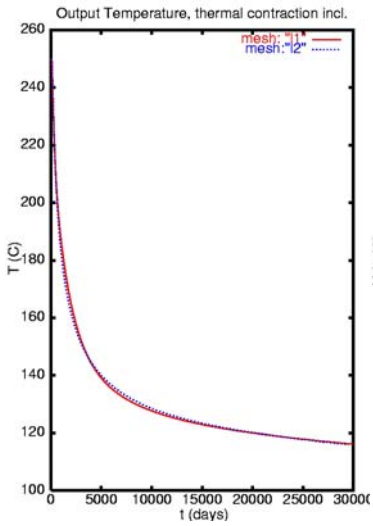

Fig. 5.2.8: T decay, inc. thermal contraction.

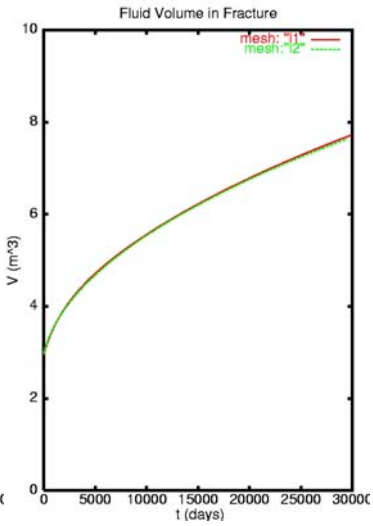

Fig. 5.2.9: Fluid volume.

5.3. Gringarten benchmark.

The Gringarten analytic solution has been discussed in the theory (§ 2.2.4). It can be used to benchmark the 3D-version of GEOCRACK. The system consists of a plane fracture intersected by two wells (see fig. 2.2.4.1). In the fracture 2D advection in x and z direction is allowed, in the rock 1D diffusion orthogonal to the fracture. The total flow through the system is constant. The following parameters have been used to benchmark the GEOCRACK finite element code (see also Appendix C, figures C8 till C11:

- System boundaries: x × y × z = 400 × 400 × 400 m
- Well-distance = 100 m
- Benchmark point located on the line injection well - production well at a distance of 50.8 m from injection well.
- Fracture aperture = b = 0.1 mm
- Total flow = Q = 1 l/s
- Initial rock temperature = T_R = 250 ^{0}C
- Water inlet temperature = T_W = 50 ^{0}C

Figure 5.3.1 shows the temperature decline at the production well for a period of 1000 days. It shows that the fit between the two curves is exact. This is a remarkably good result, even more when we consider the differences between numerical and analytical solution:

- The analytic solution does not consider 2D heat-diffusion through the rock.
- The analytic solution assumes an infinite volume and fracture (see Appendix A4)

This result gives confidence in the further use of the GEOCRACK3D finite element code.

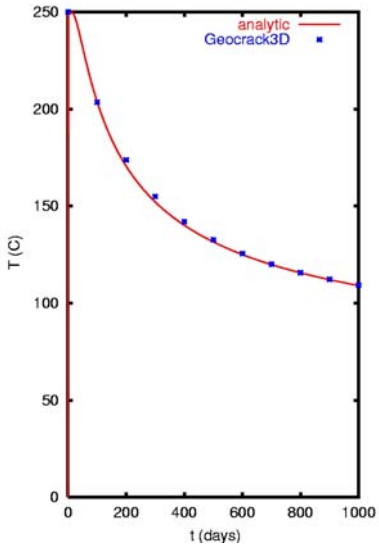

Fig. 5.3.1: Analytic and numeric results of the Gringarten-problem.

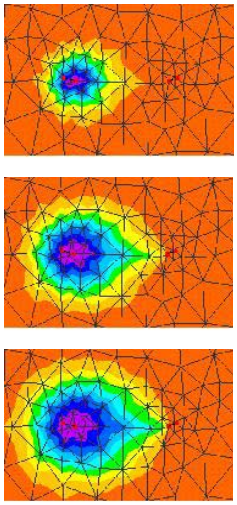

Fig. 5.3.2: Temperature contours at 100, 500 and 1000 days

5.4. Standard Galerkin versus Petrov-Galerkin

Several times during the research we had to deal with over- and undershoot problems as well as oscillation problems, sometimes leading to convergence problems. Four months after the start of the research, a new executable became available containing a Petrov-Galerkin (PG) discretisation algorithm. PG-discretisation should prevent the solution from oscillating. Tests were performed to check the effects of this improvement. Oscillations can occur when over- and undershoot are severe, for example when a sharp thermal gradient is present in the system. A simple geometry containing two vertical fractures at a distance of 60 m, interconnected by two horizontal fractures at a distance of 40 m (see figure 5.4.1) has been tested. The rock has an initial temperature of 250 ^{0}C. In the left fracture a constant flow of cold water (20 ^{0}C) is injected. The results show (figure 5.4.1) that temperature profiles after 15 days are similar. Both Standard Galerkin (SG) and Petrov-Galerkin (PG) show severe overshoot, up to 40 ^{0}C above the background temperature of 250 ^{0}C. This is due to the sharp temperature gradient near the fracture edges, caused by the high flow rates and low input temperature (20 ^{0}C). Using elements with a smaller size perpendicular to the fracture could reduce this overshoot.

Halfway along the right vertical fracture, relatively cold water (flowing horizontal) meets up with relatively hot water (travelling up-ward). This is due to the difference in travel path of both fluids. This results in a sharp thermal gradient, causing numerical errors. This is best shown in figure 5.4.1, where the temperature along this part of the fracture is plotted for both a SG and PG iteration scheme. The SG solution gives heavy oscillations, next to over- and undershoots, with a period of one mesh length (10 m), whereas the PG solution is very smooth, with no oscillations and only small overshoot. Both algorithms converged within the same number of iterations (202 iterations for t = 100 days). The PG-algorithm iteration time is about one-and-a-half times the SG-algorithm iteration time (0.36 s vs. 0.24 s).

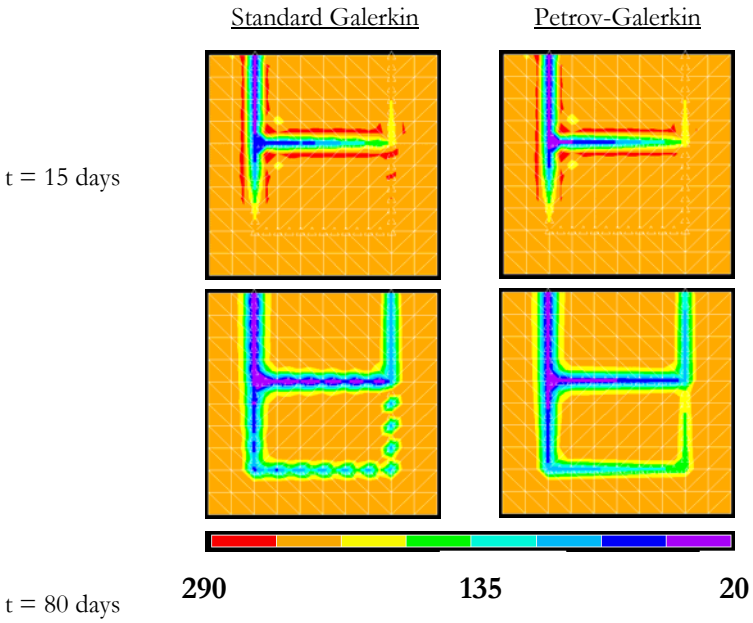

Fig. 5.4.1: Comparison of temperature contour plots between Standard Galerkin and Petrov-Galerkin discretisation.

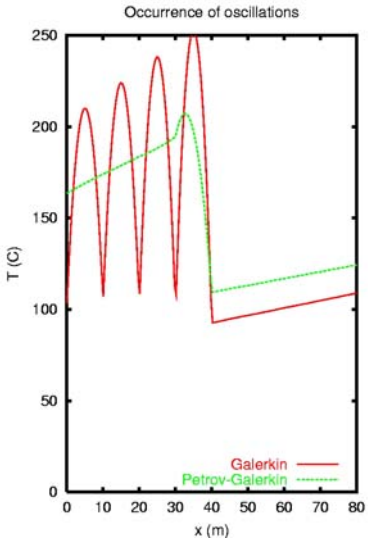

Fig. 5.4.2: Temperature along right vertical fracture, t = 80 days

5.5. Rock deformation experiments

One of the main benefits of the GEOCRACK finite element code is that it performs rock deformation calculations. This is especially important as in HFR-systems there is always the risk of so called 'short-circuiting'. By this expression we refer to the concept that a dominant fracture carrying the bulk of the fluid, will become more and more dominant due to its faster increase in aperture due to faster cooling of nearby rock. This is thus a self amplifying process; the fracture wall cools faster causing more thermal contraction, resulting in an increased permeability which causes even more water to flow through this particular fracture, causing more local cooling.

Displacements are either caused by thermal contraction or by the stress-regime. An initially stable reservoir (summation of forces on each node is zero) is deformed due to local cooling which causes a change in the stress-regime. Moreover the relation between fracture opening and fracture stress is of importance. Here the Gangi-model is used; as the joints close they become more stiff, and as they open they become softer. The fractional contraction of an element is the multiplication of the decrease in temperature times the thermal expansion factor.

Tests have been performed to obtain an impression of the consequences of short-circuiting. For these tests we use a simple heat exchanger containing two straight fracture planes. To prevent the solution being disturbed due to asymmetric initial conditions, it was chosen to use the mesh shown in figure C7, Appendix C. This figure shows the displacement boundary conditions as well; nodes are not allowed to move perpendicular to the boundary. This prevents the system from decreasing in volume, and ensures that all the thermal contraction will contribute to the growth of the fractures. A constant flow boundary condition of 1×10^5 kg/day has been implemented on the top at the vertical

fracture. There is a zero-heat-flux boundary condition on all edges. Further parameters are given in table 5.5.1.

Three cases have been tested. First of all a reference case (case I) has been simulated. In this system the left and right fracture have the same initial aperture and therefore the same initial flow rate. In case II the right fracture has twice the initial flow rate of the left one, caused by an initial aperture: $b_R = \sqrt[3]{2}\, b_L$. In the last case (case III) the aperture of the right fracture is twice the aperture of the left one causing the initial flow through the left one to be 8 times less ($q \sim b^3$).

For all three cases the flow rate, displacement and fluid temperature in both fractures is monitored. In an Excel-sheet the combined temperature decline of both output fluids has been calculated. The results can be found in figures 5.5.1 to 5.5.4.

a_0 = zero stress joint opening =
σ_c = stress at which joint is assumed to be closed = 100 MPa
m = Gangi constant = 0.33
α = thermal expansion = 0.92×10^{-5}
d = thickness heat exchanger = 40 m

Initial values	Case I		Case II		Case III	
	right	left	right	left	right	left
q (kg/day)	5×10^4	5×10^4	6.7×10^4	3.3×10^4	8.9×10^4	1.1×10^4
b (mm)	1	1	1.3	1	2	1

Table 5.4.1: Parameters.

It is remarkable that in case I, although both fractures have the same initial flow rate, after some time the flow rate in the right fracture (dotted curve in figure 5.5.1) increases at the expense of the left one. This is not what one expects as the initial and boundary conditions are totally symmetrical. This could be caused by small numerical errors. A small error in the displacement of a node on one of the fracture edges could have caused a change in evolution between left and right fracture. The other two cases show a fast increase in the flow rate of the dominant fracture. Both show that after a certain period a equilibrium is created. Two phenomena have to be considered. Due to increased flow-rates the thermal decay will increase. On the other hand, this increased thermal decay causes the curvature of the time-temperature graph of the dominant fracture to decrease faster. This implies that less and less heat is removed and finally the contraction will stop. In case II we even see that the flow rate of the dominant fracture decreases after 800 days. At this moment (see figure 5.3.3) the temperature curve of right fracture has become nearly horizontal indicating that very little heat is removed by the fluid. In other words; the aperture of the right fracture has reached has maximum size and the aperture of the left one is still growing. This phenomenon can not be find in the curves of case III. This is because in this case the left fracture has no or very minimal thermal contraction, which can be concluded from the fact that there is no temperature decay of the water in this fracture (fig. 5.5.4). We can conclude that distribution of fluid flow rates is severely affected by thermal contraction corresponding fracture opening. Figure 5.5.2 gives the temperature of the total volume of produced fluid (both fracture outputs) as function of time. It is clear that 'case I' has the smallest thermal decay. On the other hand this is also the most effective way of cooling of the block: after a certain period the case I-curve will drops below the other two curves.

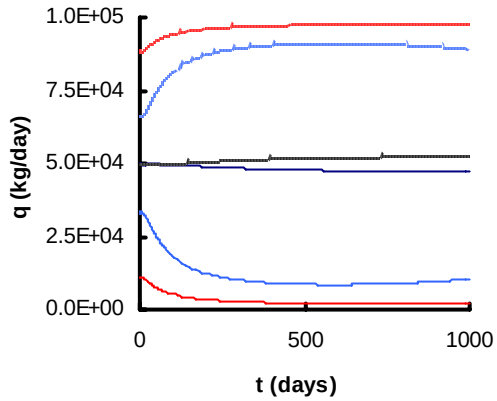

Fig. 5.5.1: Flow logs in right (dominant) and left fracture. Black curve = Case I, Blue curve = Case II, red curve = Case III. The little wiggles are plotting artefacts.

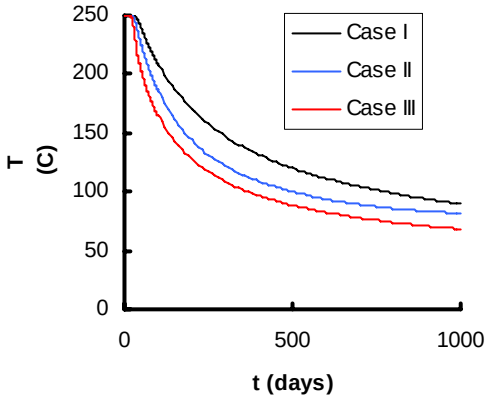

Fig. 5.5.2: Temperature decay curves of the three test cases.

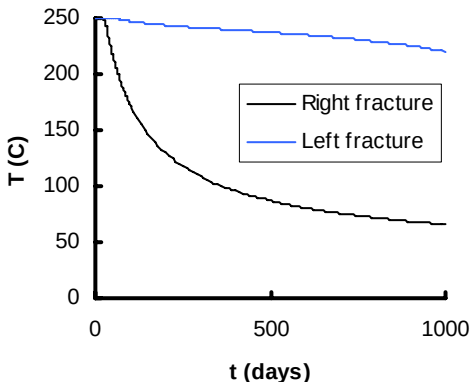

Fig. 5.5.3: Water temperature in right (dominant) and left output. Case II.

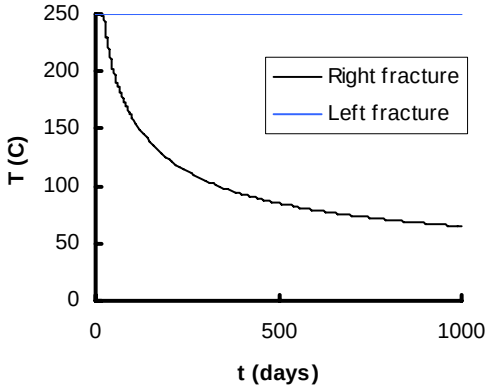

Fig. 5.5.4: Water temperature in right (dominant) and left output. Case III.

6. SOULTZ-SOUS-FORÊTS DATA

6.1. General Geology

The Soultz site is located close to the center of a wide geothermal anomaly (figure 1.4.1), on the western border of the Rhine Graben. A heat flow density of 140 mWm^{-2} , more than twice the European mean heat flow, is present. The three mayor tectonic events that structured this area are the Variscan orogeny, the subsequent late-tectonic extension, and the Cenozoic opening of the Rhine Graben rift system. The Rhine Graben can be considered as one of the best-documented basins in the West-European rift system. A cross-section (figure 6.1.1) shows a typical Graben-like structure, with sub-vertical, North-South (~ 170°) striking fractures. This is parallel to the direction of maximal horizontal stress. The granite (from depths of 1400m) is covered with sediment, with a classic Trias German subdivision, consisting of 'Bunt'sandstone , Muschelkalk and dolomite layers. The sediment has a severe geothermal anomaly of 100°C/km, while in the granite the temperature gradient varies from 10°C/km from 1.4 to 4 km depth and a gradient of 30 °C/km at depths between 4 and 5km. A natural convective flow system is expected in the granite rock, causing the relativly small gradient between 1.4 and 4km depth, although the permeability is very small.

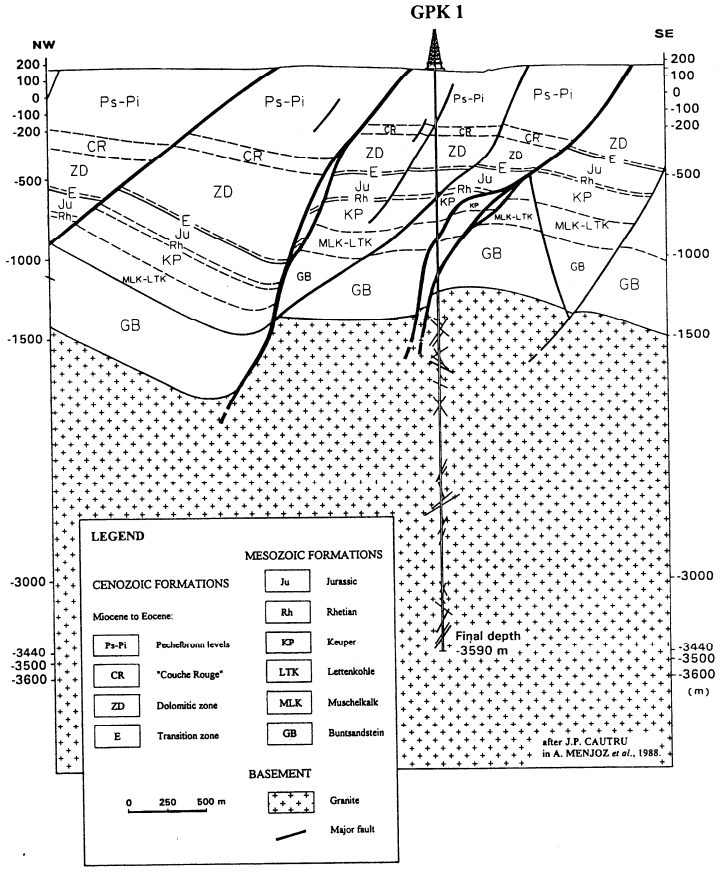

Fig. 6.1.1: NW-SE geologic cross-section.

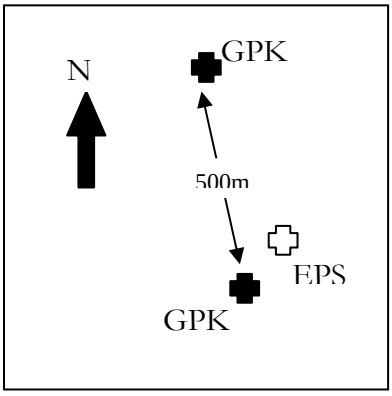

Fig. 6.2.2: Schematic location wells

6.2. Bore Hole Data

Various studies have been performed using geological samples (cuttings, cores) and numerous geophysical logs to obtain more information about the near well geology. This paragraph gives in short the most important results required for the numerical implementation.

Stresses

The geophysical imagery tools FMS (Formation Micro Scanner), BHTV (Bore Hole Tele Viewer) and UBI (Ultrasonic Bore hole Imager) provide not only images of the natural fracture system but also a very accurate definition of the mean azimuth of the maximum horizontal stress field. In the three wells (GPK1, GPK2 and EPS1) a general direction of 170°N was observed. The stress magnitude in the granite was obtained using hydro-fracture stress measurements methods and is a function of depth [A. Gérard, 1998]:

Least horizontal stress: $S_h = 15.8 + 0.0149 \times (Z - 1458)$

Max. horizontal stress: $S_H = 23.7 + 0.0336 \times (Z - 1458)$

Overburden stress: $S_Z = 33.8 + 0.0255 \times (Z - 1377)$

Fractures

According to reports by BRGM [A. Genter et al., 1997] fractures can be subdivided into three main categories based on the length scale of the fracture:

1. Large scale faults (pluri-hectometric to kilometric scale)
2. Fracture zones (10-100m)
3. Minor fractures (~ 1m)

The first group contains the large sub-vertical geologic faults as can be seen in figure 6.1.1. We expect these faults not to have a direct influence on the HFR reservoir. Thus, we actually assume that the reservoir is a closed system. Some other researchers (e.g. D. Pribnow) expect the reservoir to be connected with deeper structures with these large faults.

The second group is of more interest. Borehole imaging discovered several fracture zones; about once every 500m. These zones have a dominating strike N-S to NE-SW and have dipping angle from 70° to 90° either East or West (figure 6.2.1). Considering the dip of these fracture zones, we can estimate a mean normal distance between the fracture zones of about 200m to 250m.

During borehole imagery, lots of small scaled fractures (~ 1m) have been identified. They are rather randomly distributed but have a mean frequency of once every 2m. Only 1% of all measured fractures has a initial aperture suitable for fluid flow. The dimensions of these apertures are given in a fractal relation (see figure 6.2.2) and have a mean of 1mm. Again they show a general strike direction N-S to NE-SW, with dip-directions either East or West (figure 6.2.1).

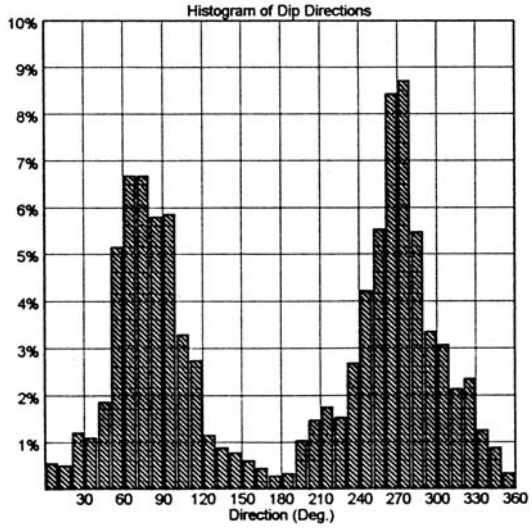

Fig. 6.2.1: Source: *Joint Network* [Tenzer et al.,1998]

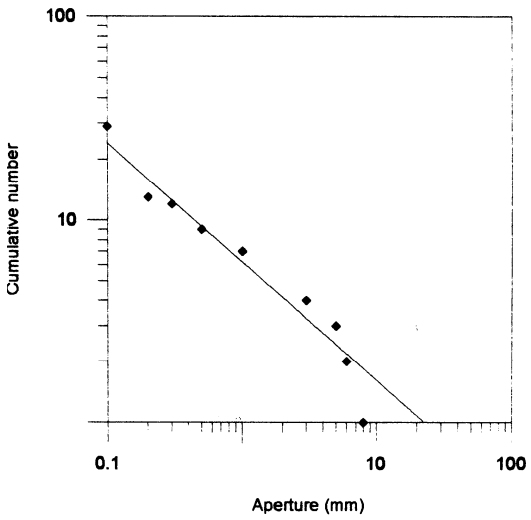

Fig. 6.2.2: Fractal relation between number of fractures and aperture (source: [BRGM staff, 1998])

6.3. Micro-seismic Data

During hydro-fracturing the propagation of the micro-seismic cloud is recorded. Micro-seismic events are related to the creation of a fracture network. Microseismic maps show a N-S expansion of the events. As expected, this is perpendicular to the direction of minimum horizontal stress. Figure 6.3.1 shows the vertical expanse of the micro-seismic events. It can be observed that most of the events generated during the GPK1 stimulation

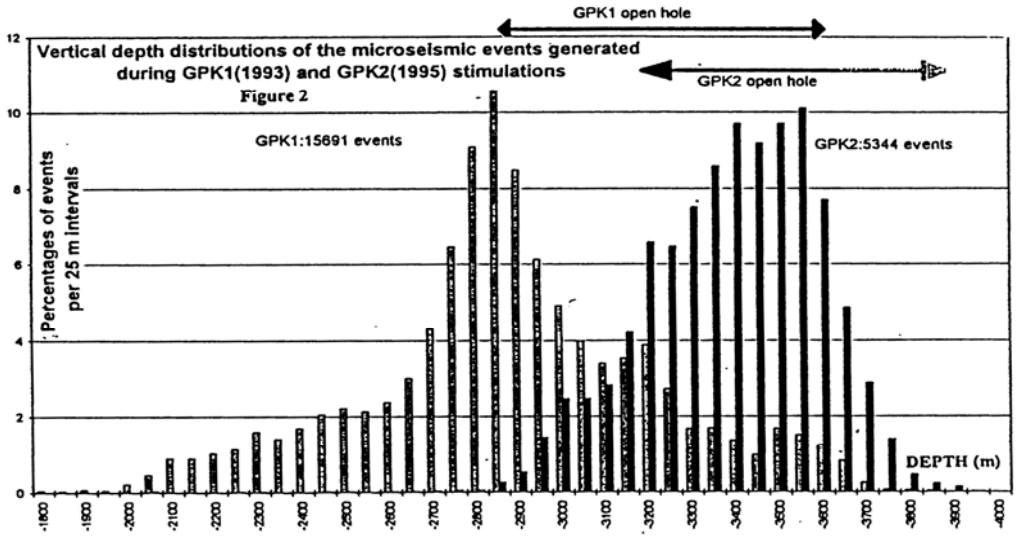

Fig. 6.2.3: Vertical distribution of seismic events of the hydraulic stimulation of GPK1 and GPK2, source: [Gérard et al., 1996]

are more or less symmetrically distributed down and above the casing shoe of GPK1 between 2500m to 3200m. We can identify one main impact zone direct at the casing shoe (2850m) and two additional impact zones at 3200m and 3500m. The distribution of GPK2 generated events is not dominated by a single major stimulated zone (due to the injection of fluid with a higher density to prevent upward migration). The main peak is translated downward 300m under the casing shoe at 3500m.

The overall seismicity can be divided into two groups. One forms a structure connecting a zone near 3500m in GPK1 with the 3470m level in GPK2. The second structure starts at around 3350m in GPK2 with an approximately NW-SE azimuth and dipping towards GPK1 [Gérard et al., 1996].

Further, the seismicity is characterized by two so-called super-stimulated volumes near the wells (each about 0.04 km^3) and a total stimulated volume, the 'reservoir-volume', of about 0.2 km^3.

6.4. Circulation tests

The most important data during circulation tests are the flow-rate profiles inside the wells. Figure 6.2.4 shows such a flow log, the logging depths have been transformed into depths

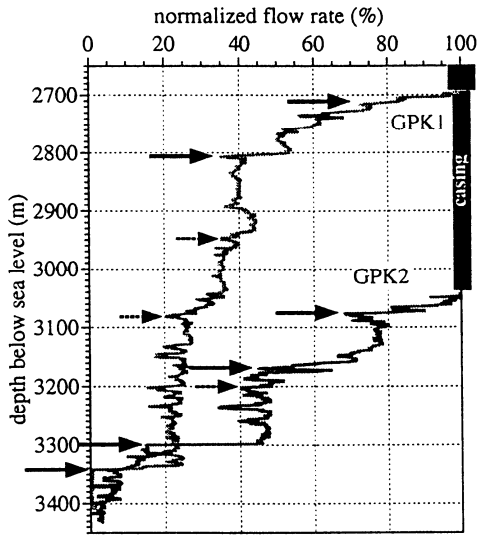

Fig. 6.2.4: Normalised flow-rates during circulation tests [Tenzer et al., 2000]

Table 6.4.1: Correlation between fractures observed by borehole televiewer and flowlogs. [Tenzer et al., 2000]

Well	Depth (mbwh)	Depths (mbsl)	Relative flow (%)	Strike	Dip	Intersection depth (m)
GPK1	2870	2710	25	N20	W70	-
	2960	2810	30	N05	W80	-
	3500	3340	25	N05	E85	-
GPK2	3250	3080	25	N150	E60	3500
	3350	3180	25	N140	E85	-
	3470	3300	25	N175	E70	3330

below sea level. To obtain depths below well head, one should add 170m (for comparison with the seismic data). In each well we can identify three separate flow zones which account for 25% or more of the total flow through that well (marked with the solid

arrows in figure 6.4.1). Table 6.2.1 gives these high output flow-rate-depths, as well as their expected direction through the granite (Borehole Televiewers) and possible intersection depth with the other well.

If we combine the flow-rate profiles with the microseismic data we can determine that the main link between the two wells is at a depth of around 3.5 km.

In GEOCRACK2D the possibility to perform tracer tests is implemented. Tracer test data from Soultz-sous-Forêts could be used to calibrate the proposed finite element models. First Tracer arrives 72 hrs after injection with a circulation rate of 25 l/s. The curve peaks at 300 hrs (12 days) after injection.

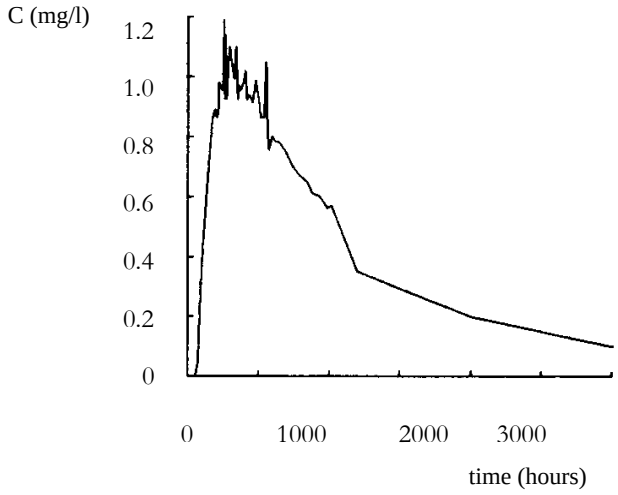

Fig. 6.2.5: Benzoic acid tracer data (source: [Audigane, 2000])

7. NUMERICAL IMPLEMENTATION

In chapter 6 the available geologic and geophysical data is summarised. The full implementation of these data in numeric models is not possible. Especially 2D-models require severe assumptions on geometry. In the following paragraphs we discuss a few possible 2D- and 3D-model implementations. As GEOCRACK is fracture oriented, we will focus on the implementation of the fracture network into the numeric solver. The physical parameters given in Appendix B1 are used.

7.1. Heat exchange surface and reservoir volume

Crucial factors in the thermal lifetime of a reservoir are the total heat exchange surface and total reservoir volume. The reservoir volume is especially of importance as it determines the total amount of heat present. It has been estimated from the micro-seismic data (chapter 6). It can be sub-divided in a total stimulated volume (= volume of total reservoir) and two regions close to the well-bore which are super-stimulated:

$V_{\text{Total}} = 0.25\ \text{km}^3$

$V_{\text{Super}} = 0.04\ \text{km}^3$ (2×)

All models, 2D and 3D, are based upon these values.

An estimation of the total heat exchange surface (fracture walls) is more difficult. It is of direct importance as it prescribes the rate at which heat will be removed. I have tried to estimate an upper and lower boundary of the heat exchange surface.

An upper boundary can be found by using a stereological law by Underwood [Underwood, 1970]. This relates the number of fractures (n_F) measured along a vertical line in a volume and the fracture surface (S_F) in that volume:

$$S_F = 2n_F$$

We use the ARI-borehole measurements. This device is able to characterize fractures over a certain distance relevant to fluid flow and thus only measures relevant fractures. ARI-data show a mean fracture density of 0.33 frac./m. This gives, for a total volume of 0.25 km^3, a heat exchange surface of 160 km^2.

Another way to estimate the heat exchange surface is to divide the total volume of water in the reservoir by the mean fracture aperture. During circulation tests the volume of water was estimated to be $25{\cdot}10^3\ \text{m}^3$. The mean fracture aperture is about 1mm (see figure 6.2.1). We can calculate for the total fracture surface:

$$S_F = 2 \times 25{\cdot}10^3/10^{-3} = 50\ \text{km}^2$$

This can be assumed as a lower boundary as the influence of smaller fractures has not been taking into account. The fact is that these give only a minor contribution to the total fluid-volume in the reservoir but they do give an equal contribution to the heat exchange-surface.

We can calculate a geometric mean from the calculated lower and upper boundaries:

$$S_{Mean} = \sqrt{160 \times 50} = 90 km^2$$

P. Audigane [Audigane, 2000] used in his Soultz-model a heat exchange area of 24 km^2. During the research we experienced that a total fracture surface area of 90 km^2 implied a numerical model that converged too slowly to be practicable. That is why it has been decided to proceed with smaller areas of order 10 km^2.

7.2. 2D-Model Implementation

2D interpretation of 3D structures involves severe limitations on the geometry. We have to choose a certain cross-section with optimum symmetry characteristics. The Soultz HFR reservoir has been designed such that the general fracture orientation and maximum horizontal stress are parallel to the line connecting GPK1 and GPK2. The wells have been located in such a way that the resistance between them is minimal and thus minimizing the necessary overpressure. We can either choose a (near) vertical cross-section through the wells or a (near) horizontal cross-section perpendicular to the main fracture planes. The first option would give us the facility to implement the depth dependent logs (figure 6.4.1) and seismic stimulation results, which vary with depth as well (figure 6.3.1). A near horizontal cross-section allows a better representation of the fracture geology, including the fracture-zones, as they are all near vertical.

7.3. Horizontally oriented models

The 2D-models (see figure D1, appendix D) assume symmetry in the horizontal plane at 3500m. According to the data given in chapter 6, at this depth the main link between the wells can be found. Further we assume vertical fractures, nearly inline with the line GPK1-GPK2. We expect a depth range of the reservoir to be 400m, extending from 3200m to 3600m. To obtain the correct model volumes the following sizes in x and y direction have been chosen:

Total stimulated volume: x × y = 800 m × 750 m

Super stimulated volumes: x × y = 200 m × 300 m

The total fracture network and mesh are given in appendix D (figure D1) as well as the parameter values (table D.1). All models have a fracture network consisting of connected fractures with a length of 100m. Fracture zones (high permeable fractures) are located at a normal distance of 200m from each other and directed North-South.

With this fracture model a series of runs with different background rock properties have been performed. One without any permeability in the background rock, one with a uniform permeability in the whole reservoir and one with an increased permeability close to the wells. From now on these cases will be called respectively the *non-permeable*, *constant permeability* and *variable permeability* cases. The precise permeability values can be found in table D.2 of Appendix D. In the *non-permeable* model all the flow is channelled through the fracture network; there is no porous flow through the rock. The *constant permeability* case has a isotropic background rock permeability of $1 \cdot 10^{-17}$ m^2. The *variable permeability* case consists of two so-called super-stimulated volumes close to the wells with a permeability of $1 \cdot 10^{-15}$ m^2 and a background permeability of $1 \cdot 10^{-17}$ m^2 in the rest of the reservoir. These values are summarised in table D1 in appendix D.

The line GPK1-GPK2 is a line of symmetry. By implementing a symmetry boundary condition on this line, calculation times were halved. All other boundaries have Neumann temperature boundary conditions ($\partial T/\partial z\big|_{z = zmax,\ zmin} = \partial T/\partial y\big|_{y = ymax,\ ymin} = \partial T/\partial x\big|_{x = xmax,\ xmin} = 0$) and Dirichlet fluid flow boundary conditions ($q\big|_{z = zmin,\ zmax} = q\big|_{y = ymin,\ ymax} = q\big|_{x = xmin,\ xmax} = 0$). Mechanical boundary conditions are defined in such a way that the outer knots are allowed to move a (small) finite distance (see appendix D). Another important item is the correct implementation of the relation between fracture opening and fracture stress. This is described in detail in appendix D and plotted in figure D6.

A fourth model representing the Soultz system has been used during the research. This model was added as verification if the use of the symmetry plane (GPK1-GPK2) in the models described above is valid. An artefact of implementing a symmetry boundary condition on this line is that the most central fracture does not carry any fluid since it lies exactly on the edge of the system. The added model (which from now on will be called *reference model*) does not make use of this symmetry plain. Therefore its calculation time will be twice as long (≈ 3 days). The *reference model* has the same parameter implementation (permeability, porosity, etc.) as the *variable permeability model.*

7.4. Vertically oriented models

A group of vertical 2D models representing the Soultz HFR reservoir have been tested. The implementation of these models was based on figure 6.4.1 and table 6.4.1. They give information where large fractures are along the borehole and how much fluid they absorb. The exact implementation is explained in Appendix D, figure D2.

During testing of the vertical models we detected that the steady-state solution converged correctly as well as the first transient steps. The strange phenomena occurred that always between 100 and 200 days after the start of circulation of water, the solution did not converge anymore. The reason for this remains unclear. Several tests have been performed (e.g. decreasing time step, decreasing flow rate, small changes in stress regime, less in- and output locations, etc.). None of them changed the result such that the calculations converged for times beyond 200 days.

At a certain moment, it was decided to omit further attempts to improve the vertical models. The reason was a lack of time and priority was give to the 3D model. The consequence is of course that no relevant results are available from the vertical models.

7.5. 3D-Model Implementation

At the beginning of November 2000 the 3D version of the GEOCRACK finite element code became available. This gave us the opportunity to build more realistic models. We have to mention here that the 3D version was a beta release at that time, with a number of restrictions. The most important restrictions are:

- Porous flow is *not* included.
- Rock mechanics are *not* included.

According to D. Swenson these points will be included by the beginning of the year 2001. In spite of the absence of these points, a 3D numerical model can be very useful, especially to determine if the 2D models are reasonable. Further the exact fit in the benchmark problem (§ 5.3) is promising.

For the implementation of the 3D model I have made use of circulation test data and data of the main hydraulic fractures. This data can be interpreted as six well-crossing fractures from which two cross both fractures. This is summarised in table 6.4.1 and figure 6.4.1. Table 6.4.1 gives the 6 identified main hydraulic fractures (depth, strike and dip), their relative part of absorption of fluid and their possible intersection with the other well. The two direct hydraulic connections are located at 3250m in GPK2 to 3500m in GPK1 and from 3500m depth in GPK2 to 3330m in GPK1. According to D. Pribnow [Pribnow, 2000] at least one direct hydraulic link is necessary to fit model data with observed data. The other fractures cross only one well; two fractures each well. The system created consists of a network of 6 interconnecting fractures in a 0.25 km^3 rock volume. The geometry of the model and the mesh discretisation can be found in appendix D (figures D3 and D4). It is actually quite similar as the Soultz HFR-conceptual model proposed by D. Pribnow [Pribnow, 1999]. He proposed a model consisting of 7 fractures. Towards the wells the surface mesh elements decrease in size to a minimum at the wells of 10m. The maximum element size, for as well surface as for volume elements, is about 150m.

All fractures absorb all more or less the same amount of fluid (25-30% of the total flow). That is why we have chosen to use a constant fracture aperture of 0.1 mm.

8. NUMERICAL RESULTS

8.1. Tracer tests

In figure 6.2.5 the tracer response of the HFR-system is plotted. The first particles arrive 3 days after injection. GEOCRACK2D offers the possibility to inject particles at a certain location and measure the concentration of particles at another location. We have thus performed a series of tracer tests with the different 2D-models. The results are plotted in figure 8.1.1. All models make use of the same fracture network, that is why tracer curves of all models are the same except for the *reference model*.

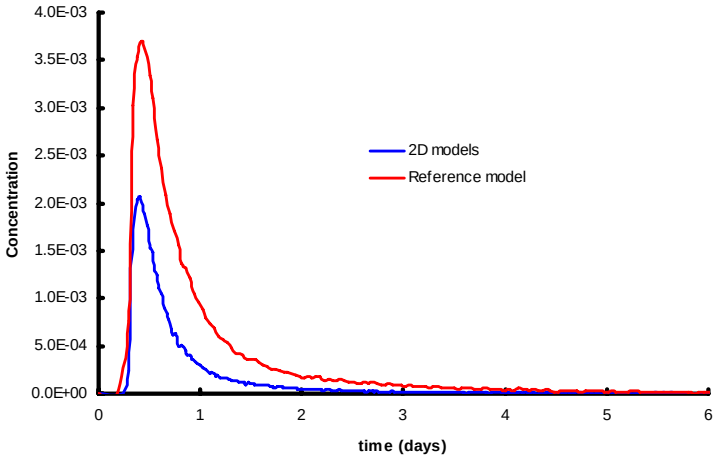

Fig. 8.1.1: Tracer results 2D models. A concentration of 100 % = 1.

Figure 8.1.1 shows that particle arrival times of the models are much faster than the observed arrival times. The peak is 12 hours after injection (injection at t = 0), 6 times as fast as the observed peak. Another difference with the observed data is the decline in particle content after the peak. The model-curves have a much steeper decline and the concentration is nearly zero after 4½ days. The observed curve shows a much slower decline in concentration. This is due to the fact that the models do not include fluid circulation between injected water and far-field water. This could cause particles to stay underground for a very long time. The *reference model* has a much higher peak, caused by the fact that twice as many particles are injected. The shape of its curve is the same as the other model curves.

8.2. Single well pressure tests

After stimulation of both wells, the effect of the stimulation tests on the hydraulic properties of the fracture system was investigated by single well injection tests. The GPK2 injection test was performed in september 1996. The main objective of this test was to determine the post-fracturing injectivity and the inlet impedance of the fracture system of GPK2. The test was performed as a step-injection test with flow rate ranging from 6 l/s to

37.5 l/s. The injection pressure was measured downhole in GPK2. GPK1 was shut-in throughout the test.

A similar test has been performed with the proposed numerical 2D-models. In figure 8.2.1 the numerical results of the three models are superimposed on the field data. The figure shows the downhole pressure increase due to increased injection flow rates. As can be seen in the figure, the pressure approaches a constant value at the end of each injection period indicating that steady state conditions are achieved. This behaviour can also be seen in the numerical results. The models have been calibrated for a flow rate of 24 l/s. This means that at this specific flow rate the numerical models will have the correct over-pressure (3.5-4 MPa). Figure 8.2.1 shows thus a good fit between field and numerical data when the flow rate is 25 l/s. In figure 8.2.1 the steady state pressure is plotted as function of the injection flow rate. The numerical data results in a linear pressure-flow rate relation, while a parabolic relation fits the field data. This indicates non-Darcy flow in the fracture system. Unfortunately this cannot be modeled with GEOCRACK2D.

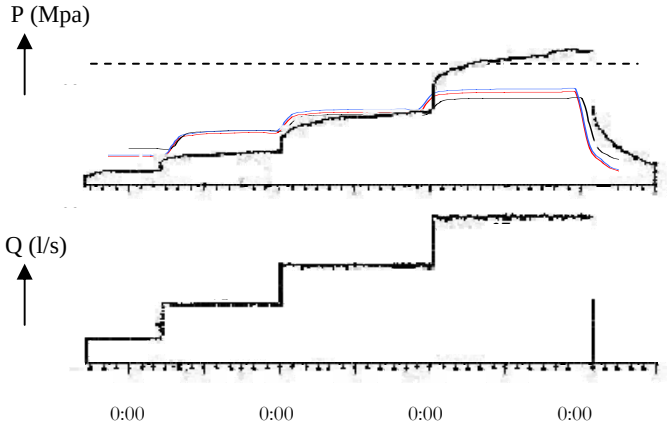

Fig. 8.2.1: Downhole pressure and flow rate of injection test Coloured lines are numerical results. (Source: *European HDR Geothermal Research Program 1996-1997, Final report.*)

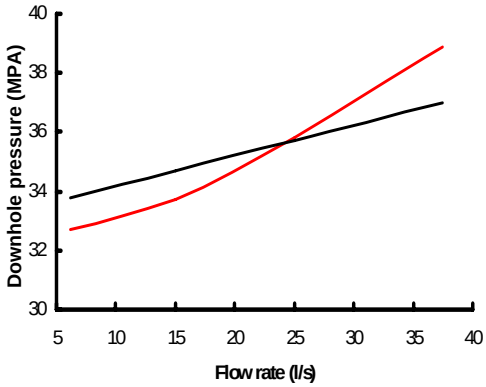

Fig. 8.2.2: Pressure vs. flow rate GPK2. Field data (red) and numerical data (black)

8.3. Temperature decay

As discussed in the previous chapter, three 2D numerical models have been tested as well as the 3D model. The 2D models have been tested for tracer data and single well test data in the previous paragraphs. Unfortunately these tests are not (yet) possible with the 3D version of the GEOCRACK finite element code.

First of all we will compare results obtained by the *reference model* with results from the *variable permeability* model. These models have the same geometry and parameter implementation but the *variable permeability model* works with a symmetry plane in the line GPK1-GPK2. This results in a zero flow through the fracture located exactly on this line. Figure 8.3.1 plot the two temperature curves of the two models.

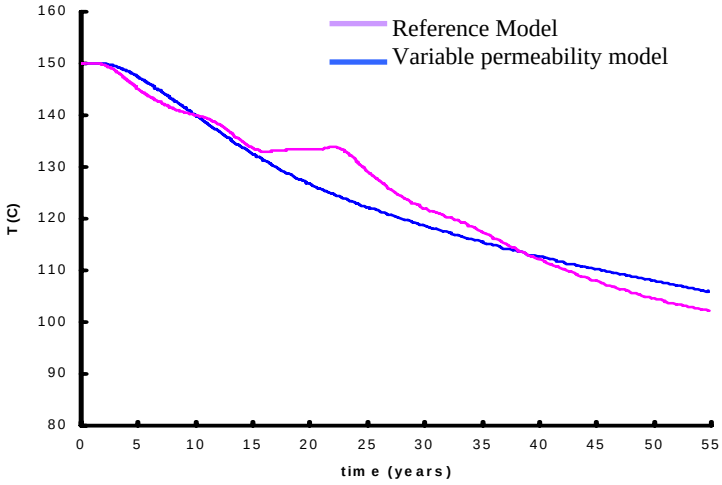

Fig. 8.3.1: Temperature decay of produced water.

The figure shows that over a period of 55 years the two models predict a similar drawdown (to 105 ^{0}C). In the first decade the *reference model* curve drops faster. This is because it has a shorter 'shortest link' (the fracture located on the symmetry line) between GPK1 and GPK2. After 16 years the *reference model* temperature curve start deviating from the *variable permeability model* curve. Even some thermal recovery occurs in the period 16 till 23 years. This can be explained by the fact that in the *reference model* the heat extraction is more focussed to the region located directly in between the wells. Due to a more focussed heat extraction thermal stresses will be greater, causing that thermal recovery can happen at earlier times. The phenomenon of thermal recovery due to changes in the stress field is described in § 5.5 *Rock deformation experiments*. After this period of small thermal recovery the fluid production temperature of the *reference model* shows a more rapid temperature drop. This is logical as until that time, more heat has been removed in the *reference model* (area below curve of the *reference model* is greater than below *variable permeability model*).

Figure 8.3.2 gives all temperature drop curves of the 2D models. As expected the *variable permeability model* gives the smallest temperature decay in the first decades due

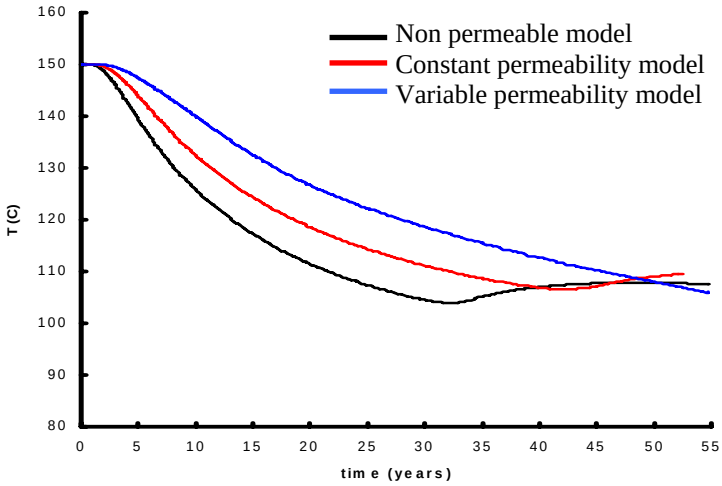

Fig. 8.3.2: Temperature decay horizontal 2D models.

to its greatest porous flow, followed by the *constant permeability model*. When a greater part of the flow is through porous rock then the heat extraction will be less focussed to the regions around fractures, causing the heat extraction will be more effective. In both *constant permeability model* and *non permeable model* thermal recovery occurs. In the *non permeable model* this occurs almost a decade earlier due to its more focussed heat extraction (no porous flow). The thermal recovery of the *non permeable model* is almost 4 degrees Celcius over a period of 15 years. In the *constant permeability model* this is only 2 degrees but the temperature is still increasing at 55 years after start of production. The increase in temperature is caused by the increase of fluid flow though the second and third vertical fracture (counting from the line GPK1-GPK2). The regions around these fractures have cooled far less because they have carried only very small parts of the total flow. Due to cooling and an accompanying change in thermal stresses, it is possible that fractures in the periphery of a system start getting more water after a certain period. This is what we see in figures 8.3.3 and 8.3.4. These figures give the flow rate of the three vertically oriented fractures (see figure D1, appendix D) at a vertical distance of 250m from both wells. The figures show that exactly at the times when the temperature of the production water increases, the fluid through the two far from the wells located fractures obtain more water. This is the reason for the thermal recovery.

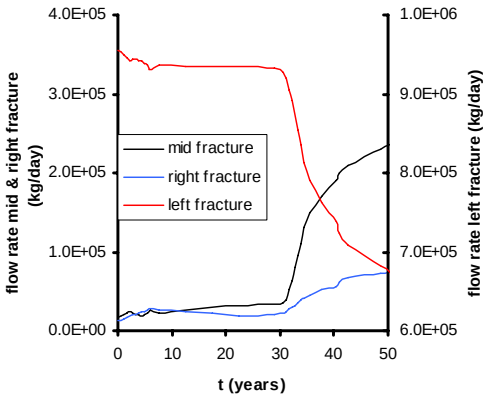

Fig. 8.3.3: Flow through the 3 vertical fractures (*non permeable model*).

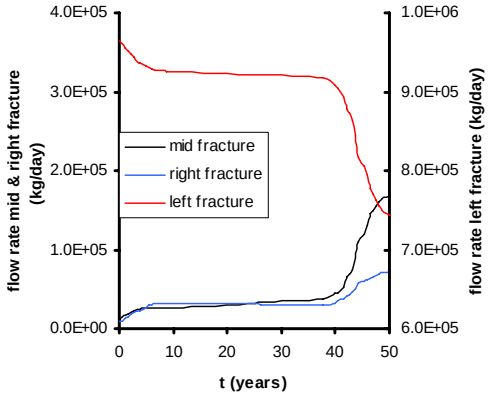

Fig. 8.3.4: Flow through the 3 vertical fractures (*constant permeability model*).

One of the research goals of this project was to compare the results from the GEOCRACK testcase models with those from other numeric codes. The most appropriate numerical model proposed for the Soultz HFR heat exchanger is the one by Pascal Audigane [Audigane, 2000]. First of all the model used by Audigane will be discussed shortly.

Audigane describes in his thesis *Caractérisation microsismique des massifs rocheux fracturés. Modelisation thermo-hydraulique. Application au concept géothermique de Soultz* three finite difference models representing the Soultz HFR reservoir. The first model consists of a hydraulic active porous medium interconnecting the two wells (*seismic*-model). It has an isotropic and constant permeability and no fractures are present. The second model consists of a couple of fracture disks in a permeable medium (*fracture*-model). The fracture disks are centred in the wells and have different extensions. The third model is a mixture of the *seismic*- and *fracture*-model (*mixture*-model). As expected the *seismic*-model has the smallest temperature decay and the *fracture*-model the greatest. The *mixture*-model is somewhat in between. These models do *not* take mechanics due to thermal contraction or the stress-regime into account.

Figure 8.3.5 compares temperature curves of the 2D and 3D models with the three model proposed by P. Audigane.

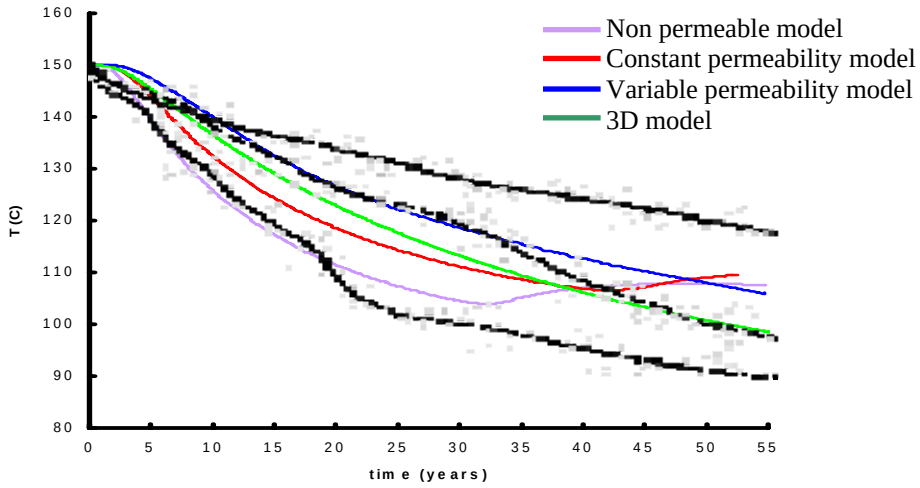

Fig. 8.3.5: Production temperatures. In black are the curves generated by P. Audigane [Audigane, 2000]. The upper black curve is the *seismic model*, the lower curve is the *fracture model* and the lowest black curve is generated with the *mixture model*.

We can observe that the newly proposed models all have a temperature decay which have values in between the values of the *fracture model* and the *mixture model* proposed by P. Audigane. This is thus in very good agreement as the *seismic model* of Audigane is not realistic as testing at Soultz indicated that the fluid flow is surely not porous dominated, but includes at least one direct hydraulic link. The *variable permeability model* curve fits the *mixture model* curve very well till about 35 years. These models both are based on the inclusion of porous flow in a network of fractures. Also the *non permeable model* and *fracture model* fit each other quite well till about 20 years. Both models only make use of a network of fractures for the transport of fluid. After 20 years the influence of the thermal contraction drives the *non permeable model* curve away from the curve by Audigane.

The good agreement of results between the proposed models and the *fracture* and *mixture model* of Audigane gives confidence in proposed models and numerical code. The 2D *variable permeability model* and the *3D model* are the most sophisticated models. When a 3D version becomes available including the possibility of porous flow, it would be very interesting to implement the parameter settings of the *variable permeability model* into the 6-fracture *3D model*. Until that time the two curves can be used as good estimations of the thermal drawdown during production the coming decades. For clarity, the two curves are plotted on their own in figure 8.3.6.

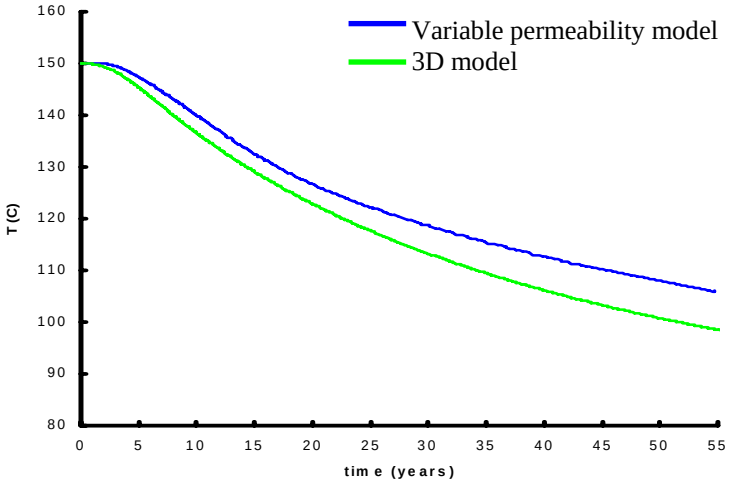

Fig. 8.3.6: Predicted thermal drawdown at an injection rate of 24 l/s.

9. 9. CONCLUSIONS

9.1. Analytic

The two analytic solutions, 'isotropic diffusion' and 'finite distance', found for the Lauwerier problem, will be discussed in this paragraph.

The isotropic diffusion solution (see §2.2.2 and appendix A.2) includes the diffusion in the x direction in the rock. The results (fig. 4.1.4 and 4.1.5) show, as expected, that the influence of diffusion in the x direction increases with decreasing fluid flow rate. At low flow rates (up to 0.8 m^3/day ≈ 1 l/min) the newly obtained solution fits the numerically generated results (2D diffusion) much better. At increasing flow rates the diffusion in x the direction can be neglected.

Results from the finite space analytic solution show that the first derivative with respect to x of the temperature indeed goes to zero when the boundary is approached. This is what we wanted. On the other hand, the influence of the boundary condition has an extend of only a few millimetres. This results in a great curvature of the function, thus a great second derivative with respect to x. This is in contradiction with the assumption made that the diffusion in the x direction (= $\partial^2 T/\partial x^2$) can be neglected. Future analytic work on this subject could include the search for the analytic solution of an isotropic diffusion finite spaced medium.

9.2. Numerical code

The accuracy of the numerical code used is described in chapter 5. The 2D as well as the 3D version has successfully been benchmarked. Especially the 3D version gave very good results; an exact fit with the analytic solution, for the Gringarten problem. This fit is less good, but still reasonable, in the 2D benchmark tests. It has to be mentioned that similar benchmark tests performed by Swenson [Swenson et al., 1997] gave exact fits between analytic and numerical solutions. The reason for this remains unclear to me.

Calculation times stayed within reasonable limits. Soultz 2D models took about 1 to 1½ day of calculation time. The executable with the Petrov-Galerkin discretisation method took about 1½ times longer than the standard Galerkin but improved results also significantly. All calculations were performed on a SUN Ultra Sparc 333MHz. Unfortunately only a windows version of the 3D code was available. Still the calculation time of the 3D Soultz model could be kept within 4 days on a Pentium III 700 MHz.

In GEOCRACK2D one can only change parameters, mesh and settings by clicking with the mouse on the right buttons. At first this seems a nice and clear method, but when working with large models it becomes very intensive and also irritating. The 3D version has improved a lot on this point. A number of strange unclear things within GEOCRACK have been noted. These are listed in Appendix E.

In general, the codes tested performed well. At this moment the program is still under development, though in the near future GEOCRACK can be a very suitable modeling

code. The following points should, and according to Swenson [Swenson, 2000] will be included in the 3D version:

- Porous flow.
- Active rock mechanics.
- Comprehensive manual.
- UNIX version.

It then could become a code of the calibre of TOUGH2 and could even be used to model hydrothermal systems. Other less crucial improvements of the numerical code include:

- Addition of a parameter to make up for the effect of non-Stokes behaviour in the flow path.
- Implementation of an easier method to change the type of continuum elements. (A very simple FORTRAN program has been written to do this for specifically generated meshes, see Appendix B)
- Possibility to switch off rock mechanics, e.g. stress-field etc..

9.3. Test case

One of the intentions of the research was to make recommendations on the production phase strategies of the Soutz-sous-Forêts HFR-project. Since a broad range of physical processes occur in a HFR system, a six months research is probably too short too make hard predictions. Still a number of interesting conclusions could be drawn from the research.

First of all, the results show that high permeability values are advantageously. Higher permeability values close too the wells increase the efficiency of the system. The effect of short-circuiting has been investigated as well. Results show that the occurrence of short-circuiting is probable when a dominant fracture is present. A striking discovery was however that it could have an advantageous effect. After a certain period a dominant fracture has cooled down so much that no rock contraction occurs any more. From that moment on other fractures will become increasingly dominant because their aperture still grows due to thermal stresses.

From the points mentioned above, one could conclude that drillers should *not* be too careful when stimulating a HFR reservoir; a high permeability is advantageous and the consequences of creating a dominant hydraulic link are probably not disastrous. The efficiency of conversion of heat in electricity plays a role here as well. The efficiency drops fast with decreasing temperature. An early drop of temperature, which will happen when a system has a short circuit, would therefor be more disadvantageous. This is discussed in more detail in Chapter 10.

The two most sophisticated of the proposed models give rise to optimism about their production temperature decay curves (fig. 8.3.6). They predict that after a period of 23 to 28 years of production (24 l/s) temperatures of around 120 ^{0}C will be reached. At these temperatures production of electricity is still possible. The numerical models thus predict that it is economically relevant to exploit the heat stored. In Chapter 10, an estimation of

the electricity production is calculated. The fact that the temperature decay curves from the proposed models are in good correlation with curves produced by P. Audigane [Audigane, 2000] (fig. 8.3.5), gives confidence on their reliability.

10. DISCUSSION

10.1. Porous flow

After 7 months of research the message came to us that a bug was present in the porous media version. According to Swenson wrong results *could* be generated when including porous flow. In the performed tests including porosity, no absurd results were found. All tests gave reasonable results. A simple test (a source and a sink that are not directly connected with a fracture) showed that flow paths generated with the old executable were indeed different from those generated with the new version. In figure 10.1.1 both porous flow paths are plotted. The magnitude of the porous flow seemed to be more or less correct.

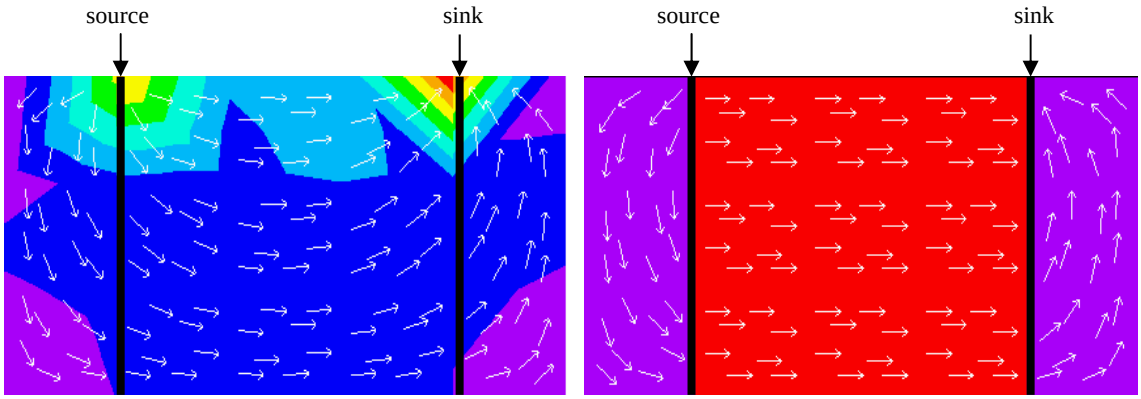

Fig. 10.1.1: Fluid flow through porous rock. Left: 'new' executable, right: 'old' executable.

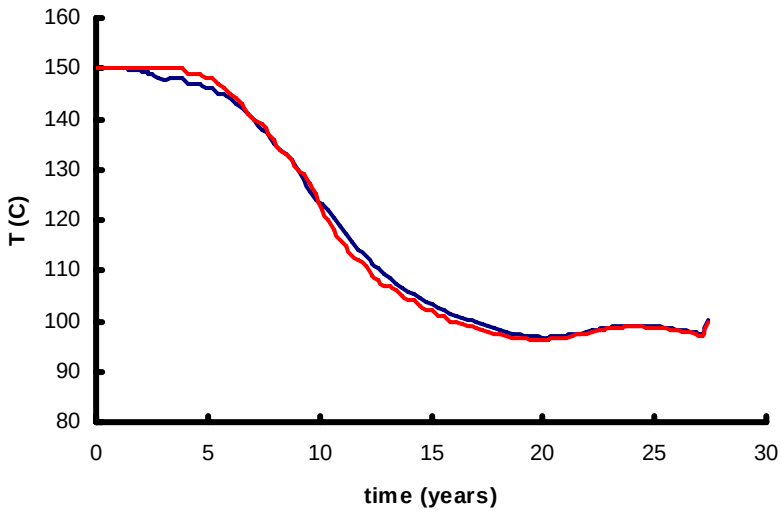

Fig. 10.1.2: Comparison of 'old' (blue) and new (red) executable.

Although very useful, no time was left to benchmark the porous flow part of the code. To ascertain that the obtained results are not irrelevant, a small test has been performed in which the old executable is compared with a bug-free executable. A mesh, consisting of 6 100×100 m^2 rock blocks (a small part of the three proposed 2D Soultz-models), has been used (see Appendix C, figure C.12). Figure 10.1.2 compares output temperature curves

generated by the two executables. The figure shows that the difference between the two curves is very small.

10.2. Sensitivity analyses

The parameterisation of the Gangi model has been a point of discussion. For this reason analyses have been performed on the sensitivity of the solution on these parameters. Figure D6 (Appendix D), plots the Gangi-curve with m = 0. 33 (used to perform the calculations of the test case models) and the Gangi-curve for m = 0.167. We can see that at the zero cross-section the second curve is steeper. This implies that, in this case, a fracture becomes rapidly softer when it opens up. This would accelerate the process of short-circuiting. We, thus, expect that output temperatures of a model with Gangi-parameter m = 0.166 will decrease faster than with a Gangi-parameter m = 0.33. The *variable permeability model* has been used to perform the sensitivity analyses. The temperature drop results are show in figure 10.2.1.

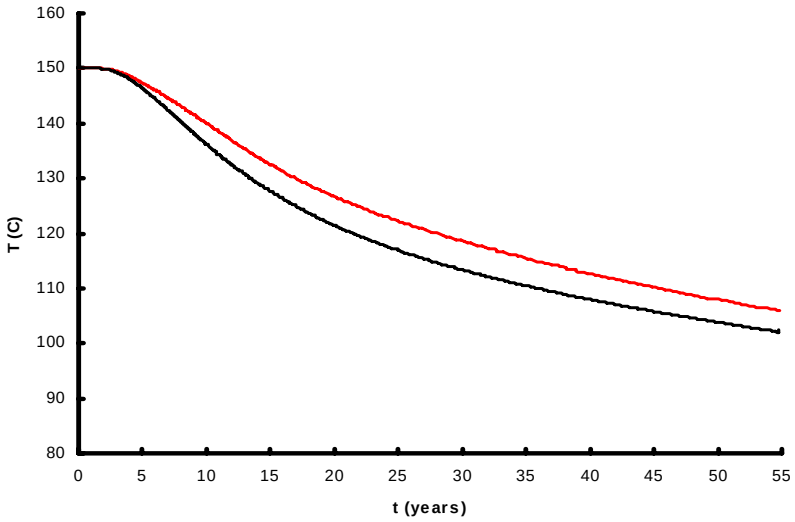

Fig. 10.2.1: *Variable permeability model* temperature drop. Red: m = 0.33, black: m = 0.167.

The temperature for m = 0.167, as expected, decreases faster. The maximum difference between the two curves is reached after 25 years. The maximum difference is about 4 ^{0}C. We can conclude that the Gangi-model does influence the solution, of course, but not dramatically.

10.3. Electricity production

The efficiency of converting heat energy to electricity is a strong function of the temperature of the produced water. It is known as the Carnot efficiency:

10.3.1.1.

$eff_C = (1 - T_0/T_{out})$ (all temperatures in Kelvin)

Where T_0 is a temperature at which the efficiency is supposed to be zero. According to Armstead and Tester [Armstead, 1987] T_0 is about 75^0C. The actual efficiency is however much lower than the theoretical Carnot efficiency. Commonly in the business is to take 2/3 of the Carnot efficiency. The fact that efficiency decreases with decreasing temperature gives an extra disadvantage when short circuiting and accompanying increasing temperature drop occurs.

From the water temperature and efficiency factor we can calculate the expected electricity production:

$$P_E = (T_{\text{production}} - T_{\text{injection}}) \times c_w \times q \times (eff_C \times 0.666)$$

In figure 10.3.1 the electricity production in MWe has been plotted against years of production for the models *variable permeability* and *3D.*

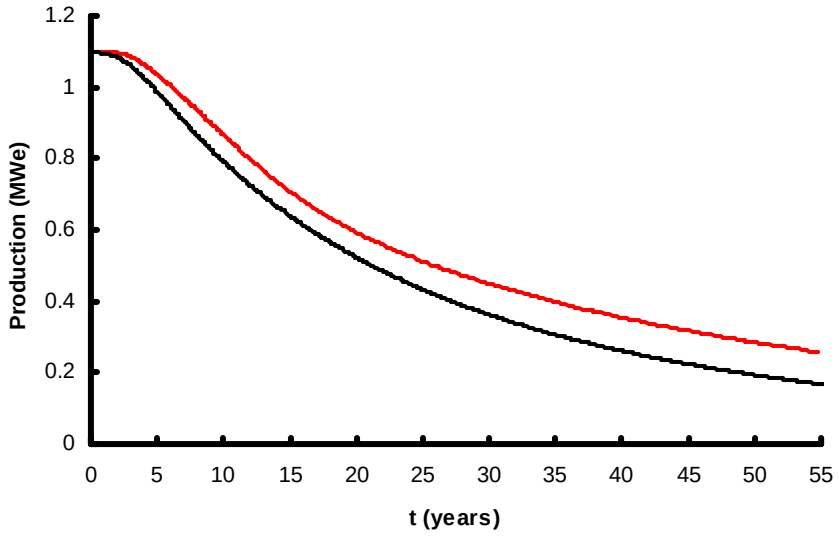

Fig. 10.3.1: Estimated electricity production of the shallow reservoir. Red: *Variable permeability* model. Black: *3D* model.

Compared with the temperature drop curves, these curves show a steeper decline due to the decrease in efficiency with decreasing temperature.

10.4. Deep reservoir

In the first months of the year 2000, the wells GPK1 and GPK2 have been deepened to a depth of 5 km. During the months February till September, a reservoir has been created using the hydrofracturing-technique. In this project the deep reservoir has not been studied because no sufficient data was available in time. The expectations are, however, that this reservoir has similar geological characteristics as the shallow one at 3500 m. The main difference is the fact that the temperature at this depth has increased to 200 ^{0}C. We could

apply a simple temperature conversion to obtain a first estimation on the thermal behaviour of the deep reservoir during production. The following formula has been used to calculate production temperature curves of the deep reservoir.

$$T^{DEEP} = \left(T_{prod.} - T_{inj.}\right) \times \frac{200 - T_{inj.}}{150 - T_{inj.}} + T_{inj.}$$

T_{prod} is the production temperature of the shallow reservoir and $T_{inj.}$ is the injection temperature (60 ^{0}C). Figure 10.4.1 shows the in this way obtained temperature decline curves of the deep reservoir at a production rate of 24 l/s. The method described in § 10.3 can be used to calculate the efficiency and the estimated electricity production. The estimated electricity production for a production time of 55 years is plotted in figure 10.4.2.

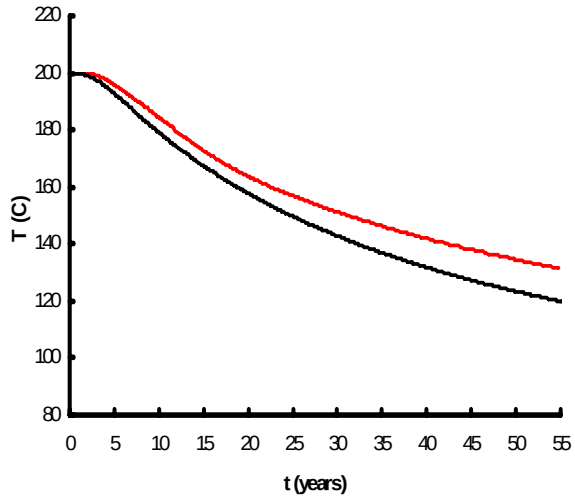

Fig. 10.4.1: Estimated temperature decay of deep reservoir (two well system).

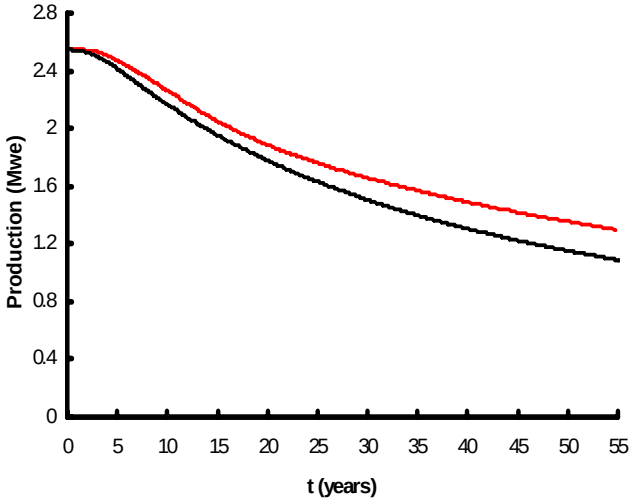

Fig. 10.4.2: Estimated electricity production of deep reservoir (two well system).

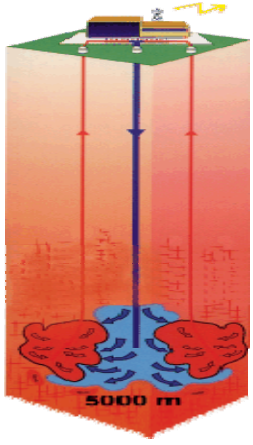

Fig. 10.4.3: Scientific pilot plant

We observe that at the start of production the deep reservoir will produce 1.5 MW more electricity than the shallow reservoir. After 55 years this difference is still more than 1 MWe.

The next aim of the HFR project in Soultz is to create a pre-industrial, scientific pilot plant consisting of three wells; one injection and two production wells (see figure 10.4.3). Such a system can be interpreted as two systems discussed in this rapport, situated next to each other. The injection flow rate would be twice that of the shallow reservoir (48 l/s). This would result in a doubled electricity production. Thus, a rough estimation on the electricity production would be about 5 MWe at the start of production to 3.9 MWe after 20 years of production. This is a hopeful result as it correlates well with the objectives and expectations of the Soutz-sous-Forêts project. An industrial power plant would consist of several three-well systems, producing at least 25 MWe at a temperature of 200^{0}C.

10.5. Closed system or not?

It has to be mentioned that all proposed Soultz models, 2D and 3D, are based upon a closed system. Thus, zero-flow boundary conditions have been implemented for fluid and heat transport. P. Audigane also assumed the reservoir to be a closed system. This assumption results in pessimistic temperature predictions; no heat is coming in.

In January 2001, D. Pribnow [Pribnow, 2000] argued that this assumption is probably not valid for the shallow reservoir. His conceptual model of Soultz starts from the idea that there is a link between the shallow reservoir and deeper geologic structures. This enlarges the total volume of the reservoir substantially. This could, for example, explain the bad tracer tests results we have obtained with our models. Temperature predictions by D. Pribnow are consequently more optimistic.

New flow-pressure data from the deep reservoir indicates that this reservoir, in contrast with the shallow reservoir, probably is a closed system.

10.6. Future work

All research objectives have been reached. Of course much work can still be done in the area of modelling HFR systems. This paragraph lists the most relevant and achievable work to be done in the near future:

Analytical

- An analytical solution could be found for the temperature field of a 2 dimensional finite spaced medium with a constant diffusion.
- A 2D or 3D analytical solutions for thermal contraction of a medium. An analytical solution could easily be found when assuming uniform temperature decay (the Lauwerier solution could be taken for the temperature) on one side of a 2D rock block.
- Attempt to incorporate a geologic stress regime in the analytic solution referred to above.

Numerical

- Benchmarks: The above-proposed analytic solutions can be used to benchmark GEOCRACK. Also a porous flow benchmark would be useful.
- Implementation of an open system. The boundary conditions could also have an influence on the predicted thermal recovery. Tests on the influence of the boundary conditions would be useful.
- Addition of porous rock in the proposed 3D model when a suitable executable becomes available.
- Build a 3D model for the deep reservoir (5 km depth) at Soultz-sous-Forêts.
- Test GEOCRACK for possible use in hydrothermal systems. This should, of course, be deferred until the porous flow benchmark has been successfully completed. So far,

GEOCRACK does not incorporate phase changes. This can be an obstacle in modelling hydrothermal systems.

11. ACKNOWLEDGEMENTS

I would like to thank a number of people who have been of great support during this project. Firsts of all my acknowledgments go to my two supervisors; Dr. A.P. v.den Berg from the faculty of Earth Science at the Utrecht University and C.K. Harris MA DPhil from EPT-AN at Shell Rijswijk. Especially I would like to thank Chris and the rest of the Geothermal Team to offer me the oppurtunity to do this research. I strongly appreciate the support given and the pleasant work environment. Finally, I would like to thank D. Pribnow for his useful and critical comments on the proposed models and the report.

12. REFERENCE LIST

[Armstead, 1987] Armstead and Tester, *Heat Mining,* E. & F.N. Spon Ltd

[Audigane,2000] *Caractérisation microsismique des massifs rocheux fracturés. Modélisation thermo-hydraulique. Application au concept géothermique de Soultz.*

[Bresee, 1992] *Geothermal Energy in Europe. The Soultz Hot Dry Rock Project.* Gordon and Breach Science Publishers.

[BRGM staff, 1998] *Geological aspects,* part of *Summary document for the Scientific Meeting (30th & 31st March 1998) held at Soultz.*

[Carslaw, 1960] H.S.Carslaw and J.C Jaeger. *Conduction of heat in solids.* Oxford University Press.

[Duchane, 1998] *The history of HDR research and development.* International Conference-4th HDR Forum.

[Elsworth, 1989] *Theory of thermal recovery from a spherically stimulated hot dry rock reservoir.* J. Geophysical Research 94 B2, p. 1927-1934.

[Genter et al., 1997] A. Genter, C. Castaing, C. Dezayes, H. Tenzer, H. Traineau and T. Villemin. *Comparative analysis of direct (core) and indirect (borehole imaging tools) collection of fracture data in the Hot Dry Rock Soultz reservoir (France).* Journal of Geophysical Research, Vol. 102, NO. B7, p. 15419-15431, july 10, 1997.

[Geothermex et al.] *Assesment of the State-of-art of Numerical Simulation of Enhanced Geothermal Systems, Nov. 1999.*

[Gérard et al., 1996] A. Gérard, J. Baumgärtner, R. Baria, R. Jung. *An attempt towards a conceptual model derived from 1993-1996 hydraulic operations at Soultz.* part of *Summary document for the Scientific Meeting (30th & 31st March 1998) held at Soultz.*

[Gérard, 1998] A. Gerard, R. Baria, J. Baumgärtner. *Elements for the design of a future scientific pilot plant.*

[Harris, 2000] *Hot Fractured Rocks. A new business for Shell ?* Exploration and Production newsletter- Feb. 2000.(restricted).

[Heuer, 1991] *Mathematical model of a Hot Dry Rock system.* Geophysical J. Int. 105, p. 145-150

[Jupe et al., 1995] *Numerical Modelling of HDR reservoirs.* Proceedings of the World Geothermal Congress, Florence, 18th-31st May, p. 2571-2574.

[Kolditz, 1995] *Modelling Flow and Heat in Fractured Rocks: Dimensional Effects of Matrix Heat Diffusion.* Geothermix, Vol. 24, NO. 3, p421-437

[Kolditz, 1997] *Stromung, Stoff- und Warmetransport im Kluftgestein.* Borntraeger

[Lauwerier, 1955] *The transport of heat in an oil layer caused by the injection of hot fluid.* Appl. Scientific Research, A5, 145-150.

[Oates, 2000] Private communication.

[Pribnow, 1999] *Thermal evolution of the HDR wells GPK1 and GPK2 in Soultz between 1993 and 1998.* http://www.bgr.de/gga_inst/index.html

[Pribnow, 2000] Private communication.

[Schaum, 1965] M.R. Spiegel. *Schaum's outline series: Laplace Transforms.* McGraw-Hill Book Company

[Swenson, 1995] D. Swenson, B. Duteaux, T. Sprecker. *Modelling fluid flow in a jointed geothermal reservoir.* Proceedings of the World Geothermal Congress, Florence, 18th-31st May, p. 2571-2574.

[Swenson, 1996] D. Swenson, B. Duteaux, B. Hardeman. *Insight from modelling discrete fractures using GEOCRACK.* Proceedings of the World Geothermal Congress, Stanford University, Stanford, CA.. Jan. 22-24, 1996.

[Swenson et al., 1997] D. Swenson, B. Hardeman, B. DuTeaux, T. Sprecker, M. Beikmann, R. Martineau, M. James and S. Su. *User's Manual for GEOCRACK: A Coupled Fluid Flow/Heat Transfer/Rock Deformation program for Analysis of Fluid Flow on Jointed Rock.* http://www.engg.ksu.edu/~geocrack

[Swenson, 1997b] D.Swenson and B. Hardeman. *The Effects of Thermal Deformation on Flow in a Jointed Geothermal Reservoir*. Int. J. of Rock Mechanics & Min. Sci., Vol. 34, p. 445, paper no. 308, 1997.

[Swenson et al., 1999] D. Swenson, R. Schroeder, N. Shinohara, T. Okabe. *Analyses of the Hijiori long term circulation test.*

[Swenson, 2000] *Very brief user Instructions for Geocrack3D*, 2000-9-5. http://www.engg.ksu.edu/~geocrack

[Tenzer et al.,1998] *Joint network*, part of *Summary document for the Scientific Meeting (30th & 31st March 1998) held at Soultz.*

[Tenzer et al., 2000] Tenzer, H., U. Schanz, and G. Homeier. *Development and characterization of a HDR test site at Soultz-sous-Forêts: flow logs, joint systems and hydraulic active fractures* Proc. World Geothermal Congress 2000, Kyushu-Tohoku, Japan, 2000.

[Watanabe, 1995] Wanatable and Takahashi. *Fractal Geometry Characterisation of Geothermal Reservoir Networks*. J. Geophysical Research,.100 B1, 521-528.

[Underwood, 1970] *Quantitative stereology* . Addison-Wesley

APPENDIX A1: LAUWERIER SOLUTION

In this appendix the total derivation of the Lauwerier [Lauwerier, 1955] solution will be explained. During the whole derivation we are working with the followingdimensionless parameters:

$$t_D = \frac{v}{b}t, \qquad x_D = \frac{z}{b}, \qquad z_D = \frac{z}{b}, \tag{A1}$$

$$\alpha = \frac{\lambda^r}{c^r \rho^r}\frac{1}{bv}, \qquad \beta = \frac{\lambda^r}{c^w \rho^w}\frac{1}{bv}$$

Heat-equations in the time-domain (with assumptions by Lauwerier, see § 2.2.1):

$$\frac{\partial T_D}{\partial t_D} = \alpha \frac{\partial^2 T_D}{\partial z^2} \qquad x_D \geq 0, z_D > \frac{1}{2} \tag{A2}$$

$$\frac{\partial T_D}{\partial z_D} = 2\beta \frac{\partial T_D}{\partial z_D} - \frac{\partial T_D}{\partial x_D} \qquad x_D \geq 0, z_D = \frac{1}{2} \tag{A3}$$

The boundary conditions of the problem are:

$$T_D(0, x_D, z_D) = 0 \quad , \quad T_D(t_D, 0, \frac{1}{2}) = 1 \tag{A4}$$

$$\lim_{x\to\infty} T_D(t_D, x_D, z_D) = 0 \quad , \quad \lim_{z\to\infty} T_D(t_D, x_D, z_D) = 0$$

Converting equations (A2 & A3) to the Laplace-domain, we obtain:

$$s\overline{T}_D = \alpha \frac{\partial^2 \overline{T}_D}{\partial z_D^2} \tag{A5}$$

$$s\overline{T}_D = 2\beta \frac{\partial \overline{T}_D}{\partial z_D} - \frac{\partial \overline{T}_D}{\partial x_D} \tag{A6}$$

The solution of the differential equation (A5) can be written as:

$$\overline{T}_D = F(x) e^{-\sqrt{\frac{s}{\alpha}}(z+c)} \tag{A7}$$

Substituting this into equation (A6) will eliminate the exponential-term

$$sF(x) = -2\beta\sqrt{\frac{s}{\alpha}}F(x) - \frac{\partial F(x)}{\partial x} \tag{A8}$$

With a general solution of:

$$F(x) = Be^{-(s+2\beta\sqrt{\frac{s}{\alpha}})x} \tag{A9}$$

Implementing the boundary conditions results in:

$$B = 1$$
$$c = -\frac{1}{2}$$

This gives us the final result for the temperature in the Laplace-domain:

$$\overline{T}_D = \frac{1}{s}e^{-\sqrt{\frac{s}{\alpha}}(s+2\beta\sqrt{\frac{s}{\alpha}})x-\sqrt{\frac{s}{\alpha}}(z-\frac{1}{2})} \tag{A10}$$

Which can be inverted analytically to the time-domain according to Carslaw & Jeager [Carslaw, 1960]:

$$T_D = H(t_D - x_D)erfc\left\{\left\{\frac{\beta}{\sqrt{\alpha(t_D - x_D)}}\left[x_D + \frac{1}{2\beta}(z_D - \frac{1}{2})\right]\right\}\right\} \tag{A11}$$

With *H(t)* the Heavyside function.

APPENDIX A2: LAUWERIER SOLUTION WITH LATERAL DIFFUSION

In this appendix the total derivation of 2D-diffusion through the rock of the problem addressed in the theory section (§ 2.2.2) is worked out. The problem describes lineair flow through a rectangular fracture in an infinite half-space. To include x-diffusion through the rock we write the heat-equation through the rock as a summation. The heat equation along the fracture is the same as Lauwerier uses. The heat-equations become:

$$\sum_{k=0}^{\infty}\frac{\partial T_k}{\partial t}\varepsilon^k = \alpha\sum_{k=0}^{\infty}\left(\frac{\partial^2 T_k}{\partial z^2}\varepsilon^k + \frac{\partial^2 T_k}{\partial x^2}\varepsilon^{k+1}\right) \qquad x \geq 0, z > \frac{1}{2} \tag{A12}$$

$$\frac{\partial T}{\partial z} = 2\beta\frac{\partial T}{\partial z} - \frac{\partial T}{\partial x} \qquad x \geq 0, z = \frac{1}{2} \tag{A13}$$

To improve clarity, dimensionless signs have been omitted. The boundary conditions are the same as presented in the Lauwerier solution (Appendix A.1, eq. (A4)). In the Laplace-domain for k=2 equation (A12) becomes:

$$s\overline{T_0} + s\overline{T_1}\varepsilon + s\overline{T}\varepsilon^2 = \alpha\left(\frac{\partial^2\overline{T_0}}{\partial z^2} + \frac{\partial^2\overline{T_0}}{\partial x^2}\varepsilon + \frac{\partial^2\overline{T_1}}{\partial z^2}\varepsilon + \frac{\partial^2\overline{T_1}}{\partial x^2}\varepsilon^2 + \frac{\partial^2\overline{T_2}}{\partial z^2}\varepsilon^2 + \frac{\partial^2\overline{T_2}}{\partial x^2}\varepsilon^3\right) \tag{A14}$$

Neglecting 2nd and 3rd powers in ε, will give the following equation: (A15)

$$\left(s\overline{T_0} - \alpha\frac{\partial^2\overline{T_0}}{\partial z^2}\right) + \varepsilon\left(s\overline{T_1} - \alpha\frac{\partial^2\overline{T_1}}{\partial z^2}\right) = \varepsilon\left(\alpha\frac{\partial^2\overline{T_0}}{\partial x^2}\right) \tag{A16}$$

$\overline{T}_0 = \overline{T}_L$ is the Lauwerier solution (A10), so the first term in the left-hand side of equation (A16) becomes zero. The solution of $\overline{T}_0$ is given in Appendix A.1 (A10).

- $$\overline{T_0} = \frac{1}{s}e^{-(s+2\beta\sqrt{\frac{s}{\alpha}})x-\sqrt{\frac{s}{\alpha}}(|z|-\frac{1}{2})} \tag{A17}$$

This is makes (A16) a differential equation of the second order, which can be solved given the correct boundary conditions. The differential equation can be written as follows:

$$s\overline{T_1} - \alpha \frac{\partial^2 \overline{T_1}}{\partial z^2} = g(x) e^{-\sqrt{\frac{s}{\alpha}} z} \tag{A18}$$

Which has a solution:

$$\overline{T_1} = \frac{g(x)}{2\sqrt{s\alpha}} z e^{-\sqrt{\frac{s}{\alpha}} z} = \left(\frac{z(s + 2\beta\sqrt{\frac{s}{\alpha}})^2}{2s\sqrt{\frac{s}{\alpha}}} + a(x,s) \right) \overline{T_0} \tag{A19}$$

Substituting this into equation (A18), and making use of the boundary conditions, we find the value for *a(x,s)*:

$$a(x,s) = \frac{\beta(s + 2\beta\sqrt{\frac{s}{\alpha}})^2}{\sqrt{\frac{s}{\alpha}}} x \tag{A20}$$

For the final solution of $\overline{T_1}$ in the Laplace-domain we get, with $\gamma = 2\beta x + z - 1/2$:

$$\overline{T_1} = \gamma e^{-sx} \left\{ \overbrace{\frac{\sqrt{s\alpha}}{2} e^{-\sqrt{\frac{s}{\alpha}}\gamma}}^{1} + \overbrace{2\beta e^{-\sqrt{\frac{s}{\alpha}}\gamma}}^{2} + \overbrace{\frac{2\beta^2}{\sqrt{s\alpha}} e^{-\sqrt{\frac{s}{\alpha}}\gamma}}^{3} \right\} \tag{A21}$$

The term in front of the brackets turns into a delta-pulse function when translating to the time-domain. Terms 2 and 3 can be inverted directly, using the formula's from Carslaw & Jeager[1]. Term 1 can be inverted when write it as a derivative:

$$L^{-1}\left(\frac{\sqrt{s\alpha}}{2} e^{-\sqrt{\frac{s}{\alpha}}\gamma} \right) = L^{-1}\left(\frac{\partial}{\partial\gamma}\left(-\frac{\alpha}{2} e^{-\sqrt{\frac{s}{\alpha}}\gamma}\right) \right) = \frac{\partial}{\partial\gamma}\left(-\frac{\alpha\gamma}{4\sqrt{\pi\alpha t^3}} e^{-\frac{\gamma^2}{4\alpha t}} \right) = -\frac{\alpha}{4\sqrt{\pi\alpha t^3}}\left(1 - \frac{2\gamma^2}{4\alpha t}\right) e^{-\frac{\gamma^2}{4\alpha t}} \tag{A22}$$

Terms 2 and 3 invert respectively into the time-domain as follows:

$$L^{-1}\left(2\beta e^{-\sqrt{\frac{s}{\alpha}}\gamma}\right)=\frac{\beta\gamma}{\sqrt{\pi\alpha t^3}}e^{-\frac{\gamma^2}{4\alpha t}} \tag{A23}$$

$$L^{-1}\left(\frac{2\beta^2}{\sqrt{s\alpha}}e^{-\sqrt{\frac{s}{\alpha}}\gamma}\right)=\frac{2\beta^2}{\sqrt{\pi\alpha t}}e^{-\frac{\gamma^2}{4\alpha t}} \tag{A24}$$

The multiplication in equation (A21) results in a time shift in the final solution according to the convolution theorem:

$$L^{-1}\big(f(s)g(s)\big)=\int_0^t F(t')G(t-t')dt' \tag{A25}$$

This results in an integral of a delta-pulse, giving a heavyside function. Altogether the final outcome of the temperature in the time-domain will be:

$$T=T_0-H(t-x)\frac{\gamma}{\sqrt{\pi\alpha(t-x)^3}}\left(-\frac{\alpha}{4}+\frac{\gamma^2}{8(t-x)}+\beta\gamma+2\beta^2(t-x)\right)\cdot e^{-\frac{\gamma^2}{4\alpha(t-x)}} \tag{A26}$$

With *H(t)* the heavyside function and T_0 the Lauwerier solution, given in Appendix A.1 equation (A11).

APPENDIX A3: LAUWERIER SOLUTION IN FINITE SPACE

In this appendix the full derivation of a special form of the Lauwerier solution is performed. . The classic Lauwerier solution assumes a infintite space in both the x and the z direction. Since computers always make use of a finite space solution, it is useful to have a analytic solution of a finite bounded region. Here we seek the solution of a single plane fracture in a region with finite x boundaries ($0 < x < L$) and infinite z boundaries ($-\infty < z < \infty$). We start with the formulas used by Avdonin (1964):

$$\frac{\partial T_D}{\partial t_D} = \alpha \frac{\partial^2 T_D}{\partial z^2} \qquad x_D \geq 0, z_D > \frac{1}{2} \tag{A27}$$

$$\frac{\partial T_D}{\partial z_D} = 2\beta \frac{\partial T_D}{\partial z_D} - \frac{\partial T_D}{\partial x_D} + \gamma \frac{\partial^2 T_D}{\partial x_D^2} \qquad x_D \geq 0, z_D = \frac{1}{2} \tag{A28}$$

Boundary conditions are:

$$T_D(0, x_D, z_D) = 0, \qquad T_D(t_D, 0, \frac{1}{2}) = 1, \qquad \left.\frac{\partial T_D}{\partial x_D}\right|_{x=L} = 0. \tag{A29}$$

From equation (A27) and (A28) we find that in the Laplace domain the Temperature is given by:

$$\overline{T} = e^{-\sqrt{\frac{s}{\alpha}}(z-\frac{1}{2})} F(x) \tag{A30}$$

$$s\overline{T} = e^{-\sqrt{\frac{s}{\alpha}}(z-\frac{1}{2})} \left\{ -2\beta \sqrt{\frac{s}{\alpha}} F(x) - \frac{\partial F(x)}{\partial x} + \gamma \frac{\partial^2 F(x)}{\partial x^2} \right\} \tag{A31}$$

Substituting equation (A30) into equation (A31) yield the following differential equation for $F(x)$

$$\left\{ \left(-2\beta \sqrt{\frac{s}{\alpha}} - s \right) F(x) - \frac{\partial F(x)}{\partial x} + \gamma \frac{\partial^2 F(x)}{\partial x^2} \right\} = 0 \tag{A32}$$

This differential equation is of a standard form and can be solved:

$$F(x) = Ae^{\alpha_1 x} + Be^{-\alpha_2 x} \tag{A33}$$

Implementing the boundary conditions gives:

$$\left.\frac{\partial F(x)}{\partial x}\right|_{x=L} = 0 \tag{A34}$$

$$F_0 = F(s,0,\frac{1}{2}) = \frac{1}{s} \tag{A35}$$

A and B can now be determined:

$$A = \frac{F_0}{\left(1+\frac{\alpha_1}{\alpha_2}e^{(\alpha_1+\alpha_2)L}\right)} \tag{A36}$$

$$B = \frac{F_0}{\left(1+\frac{\alpha_2}{\alpha_1}e^{-(\alpha_1+\alpha_2)L}\right)} \tag{A37}$$

To obtain α_1 and α_2 we can insert the following general solution into equation (A33):

$$F(x) = e^{\alpha' x} \tag{A38}$$

Which results in:

$$\left(s + 2\beta\sqrt{\frac{s}{\alpha}} + \alpha' - \gamma\alpha'^2\right)e^{\alpha' x} = 0 \tag{A39}$$

Which means that the pre-factor has to be zero. We can now solve α' by writing the first term of (A39) as a square function:

$$s + 2\beta\sqrt{\frac{s}{\alpha}} + \alpha' - \gamma\alpha'^2 = 0 \Rightarrow (\alpha' - \frac{1}{2\gamma})^2 = \frac{1}{4\gamma^2} + \frac{s + 2\beta\sqrt{\frac{s}{\alpha}}}{\gamma} \tag{A40}$$

$$\alpha' = \frac{1}{2\gamma} \pm \sqrt{\frac{1}{4\gamma^2} + \frac{s + 2\beta\sqrt{\frac{s}{\alpha}}}{\gamma}} \approx \frac{1}{2\gamma}\left(1 \pm \left(1 + 2\gamma(s + 2\beta\sqrt{\frac{s}{\alpha}})\right)\right) \tag{A41}$$

The approximation on the right-hand side of equation (A41) holds because γ is very small. This equation gives us the values of α_1 and α_2.

$$\alpha_1 = \frac{1}{\gamma} + s + 2\beta\sqrt{\frac{s}{\alpha}} \tag{A42}$$

$$\alpha_2 = s + 2\beta\sqrt{\frac{s}{\alpha}} \tag{A43}$$

Finally this results in the following function of the temperature in the Laplace domain:

$$\overline{T} = \overbrace{\frac{1}{1 + \frac{\alpha_1}{\alpha_2} e^{(\alpha_1+\alpha_2)L}}}^{\text{I}} \left[\frac{\overbrace{e^{-\sqrt{\frac{s}{\alpha}}(z-\frac{1}{2})+\alpha_1 x}}^{\text{II}}}{s} + \frac{\alpha_1}{\alpha_2} \frac{\overbrace{e^{-\sqrt{\frac{s}{\alpha}}(z-\frac{1}{2})+(\alpha_1+\alpha_2)L-\alpha_2 x}}^{\text{III}}}{s} \right] \tag{A44}$$

This formula cannot be inverted to the time-domain immediately. It has to be converted by part. First I will derive the inversion of the multiplication of the terms *IxIII*. This part of equation (A44) can be written as:

$$L^{-1}(I \times III) = L^{-1}\left(\frac{1}{s} e^{-\sqrt{\frac{s}{\alpha}}k_1 - sx} - \frac{\left(s + 2\beta\sqrt{\frac{s}{\alpha}}\right)}{s\left(\frac{1}{\gamma} + s - 2\beta\sqrt{\frac{s}{\alpha}}\right)} e^{-\sqrt{\frac{s}{\alpha}}k_2 - (x+2L)s - \frac{L}{\gamma}} \right) \tag{A45}$$

with,

$$k_1 = z - \frac{1}{2} + 2\beta x \tag{A46}$$

$$k_2 = z - \frac{1}{2} + 2\beta x + 4\beta L$$

We see that the 1st term on the right-hand side of equation (A45) matches the Lauwerier solution (A10). With a solution (as explained in Appendix A.1, eq. (A11)) of:

$$T_L = H(t-x)erfc\left(\frac{k_1}{2\sqrt{\alpha(t-x)}}\right) \tag{A47}$$

The term in front of the exponential in the 2nd term on the right-hand side of equation (A45) should be expanded. A first order Taylor expansion will give:

$$\frac{s+2\beta\sqrt{\frac{s}{\alpha}}}{s\left(\frac{1}{\gamma}+s-2\beta\sqrt{\frac{s}{\alpha}}\right)} \approx \frac{\gamma(s+2\beta\sqrt{\frac{s}{\alpha}})(1-\gamma(s+2\beta\sqrt{\frac{s}{\alpha}}))}{s} \tag{A48}$$

This approximation holds as γ is very small and thus $1/\gamma$ is very large. The first term formula of the right part of equation (A45) becomes:

$$\begin{aligned} &L^{-1}\left((\gamma+\frac{2\gamma\beta}{\alpha}\frac{1}{\sqrt{\frac{s}{\alpha}}})e^{-\sqrt{\frac{s}{\alpha}}k_2-(x+2L)s-\frac{1}{\gamma}}\right)-L^{-1}\left(\frac{\gamma^2(s+2\beta\sqrt{\frac{s}{\alpha}})^2}{s}e^{-\sqrt{\frac{s}{\alpha}}k_2-(x+2L)s-\frac{l}{\gamma}}\right)= \\ &H(t')e^{-\frac{L}{\gamma}}\left(\gamma\frac{k_2}{2\sqrt{\pi\alpha t'^3}}+\frac{2\gamma\beta}{\sqrt{\alpha\pi t'}}\right)e^{-\frac{k_2^2}{4\alpha t'}}-L^{-1}\left(\frac{\gamma^2(s+2\beta\sqrt{\frac{s}{\alpha}})^2}{s}e^{-\sqrt{\frac{s}{\alpha}}k_2-(x+2L)s-\frac{l}{\gamma}}\right) \end{aligned} \tag{A49}$$

With $t' = t - (x + 2L)$.

The right term of (A49) cannot be evaluated immediately. To do this, some terms need to be differentiated in advance to obtain terms suitable for inversion. The right part of equation (A49) can be subdivided into three terms:

$$L^{-1}\left(se^{-\sqrt{\frac{s}{\alpha}}k_2}\right)=\frac{\partial^2}{\partial k_2^2}\left(L^{-1}\left(\alpha e^{-\sqrt{\frac{s}{\alpha}}k_2}\right)\right)=\frac{\partial^2}{\partial k_2^2}\left(\frac{\alpha k_2}{2\sqrt{\alpha\pi t^3}}e^{-\frac{k_2^2}{4\alpha t_2}}\right)=\frac{\alpha}{2\sqrt{\alpha\pi t^3}}e^{-\frac{k_2^2}{4\alpha t_2}}\left(-\frac{3k_2}{2\alpha t}+\frac{k_2^3}{4\alpha^2t^2}\right) \quad \text{(A50)}$$

$$L^{-1}\left(4\beta\sqrt{\frac{s}{\alpha}}e^{-\sqrt{\frac{s}{\alpha}}k_2}\right)=\frac{\partial}{\partial k_2}\left(L^{-1}\left(-4\beta e^{-\sqrt{\frac{s}{\alpha}}k_2}\right)\right)=\frac{\partial}{\partial k_2}\left(\frac{-4\beta k_2}{2\sqrt{\alpha\pi t^3}}e^{-\frac{k_2^2}{4\alpha t_2}}\right)=-\frac{4\beta}{2\sqrt{\alpha\pi t^3}}e^{-\frac{k_2^2}{4\alpha t_2}}\left(1-\frac{k_2^2}{2\alpha t}\right) \quad \text{(A51)}$$

$$L^{-1}\left(\frac{4\beta}{\sqrt{\alpha}}e^{-\sqrt{\frac{s}{\alpha}}k_2}\right)=\frac{4\beta k_2}{2\sqrt{\alpha}\sqrt{\alpha\pi t^3}}e^{-\frac{k_2^2}{4\alpha t_2}} \quad \text{(A52)}$$

The equations (A47), (A49),(A50),(A51) and (A52) together give us the inverse solution of equation (A45).

$$\begin{aligned}T_{\text{I}\times\text{III}} &= H(t-x)erfc\left(\frac{k_1}{2\sqrt{\alpha(t-x)}}\right)- \\ &H(t')e^{-\frac{L}{\gamma}}e^{-\frac{k_2^2}{4\alpha t'}}\left(\gamma\frac{k_2}{2\sqrt{\pi\alpha t'^3}}+\frac{2\gamma\beta}{\sqrt{\alpha\pi t'}}+\gamma^2\left(-\frac{3k_2}{2t'}+\frac{k_2^3}{4\alpha t'^2}-4\beta+\frac{4\beta k_2^2}{2\alpha t'}+\frac{4\beta k_2}{\sqrt{\alpha}}\right)\right)\end{aligned} \quad \text{(A53)}$$

Now the second part of equation (A44) still has to be solved. The second part of this equation (*L^{-1}(IxII)*) will be somewhat harder to solve. It can be written as follows:

$$L^{-1}\left(\text{I}\times\text{II}\right)=L^{-1}\left(\frac{\alpha_2}{\alpha_1}e^{-(\alpha_1+\alpha_2)L}\left(1-\frac{\alpha_2}{\alpha_1}e^{-(\alpha_1+\alpha_2)L}\right)\frac{1}{s}e^{-\sqrt{\frac{s}{\alpha}}(z-\frac{1}{2})+\alpha_1 x}\right) \quad \text{(A54)}$$

With k_3 and k_4 given by:

$$k_3=z-\frac{1}{2}-2\beta x+4\beta L+4\beta L \quad \text{(A55)}$$

$$k_4=z-\frac{1}{2}-2\beta x+8\beta L$$

Writing α_1 and α_2 in their components (A42) and (A43), and performing a first order Taylor linearization in the pre-factor (the same as we did in (A51), we obtain:

$$L^{-1}(\mathrm{I}\times\mathrm{II}) = L^{-1}\left(\overbrace{\gamma(s+2\beta\sqrt{\frac{s}{\alpha}})(1-\gamma(s+2\beta\sqrt{\frac{s}{\alpha}}))\frac{e^{-\frac{L-x}{\gamma}-(2L-x)s-k_3\sqrt{\frac{s}{\alpha}}}}{s}}^{\bar{T}'}\right) - L^{-1}\left(\underbrace{\left(\gamma(s+2\beta\sqrt{\frac{s}{\alpha}})(1-\gamma(s+2\beta\sqrt{\frac{s}{\alpha}}))\right)^2\frac{e^{-\frac{2L-x}{\gamma}-(4L-x)s-k_4\sqrt{\frac{s}{\alpha}}}}{s}}_{\bar{T}''}\right) \quad \text{(A56)}$$

The first term in this equation is exactly the same as equation the 2nd term of equation (A45). The inverse solution of this term will thus be similar to this solution, given by equation (A53), only with different values for *k* (see above) and t" = t-(2L+x).

$$T' = H(t'')e^{-\frac{k_3^2}{4\alpha t''}}e^{-\frac{L-x}{\gamma}}\left(\gamma\frac{k_3}{2\sqrt{\pi\alpha t''^3}}+\frac{2\gamma\beta}{\sqrt{\alpha\pi t''}}+\frac{\gamma^2}{2\sqrt{\alpha\pi t''^3}}\left(-\frac{3k_3}{2t''}+\frac{k_3^3}{4\alpha t''^2}-4\beta+\frac{4\beta k_3^2}{2\alpha t''}+\frac{4\beta k_3}{\sqrt{\alpha}}\right)\right) \quad \text{(A57)}$$

The second term can be written as:

$$\bar{T}'' = \gamma^2\left(\left(c_1 s + c_2\sqrt{\frac{s}{\alpha}} + c_3 s^2 + c_4 s\sqrt{\frac{s}{\alpha}} + c_5 s^3 + c_6 s^2\sqrt{\frac{s}{\alpha}}\right)e^{-\frac{2L-x}{\gamma}-(4L-x)s-k_4\sqrt{\frac{s}{\alpha}}}\right) \quad \text{(A58)}$$

With

$$c_1 = 1-\frac{24\gamma\beta^2}{\alpha}+\frac{16\gamma^2\beta^2}{\alpha^2} \quad \text{(A59)}$$

$$c_2 = 4\beta-\frac{16\gamma\beta^2}{\alpha}$$

$$c_3 = -2\gamma+\frac{24\gamma^2\beta^2}{\alpha}$$

$$c_4 = -12\gamma\beta+\frac{32\gamma^2\beta^3}{\alpha}$$

$$c_5 = \gamma^2$$

$$c_6 = 8\beta\gamma^2$$

These terms can subsequently be inverted by taking the first, second or higher order derivatives.

1st term:

$$L^{-1}\left(c_1 s e^{-k_4\sqrt{\frac{s}{\alpha}}}\right) = L^{-1}\left(\frac{\partial^2}{\partial k_4^2}\left(c_1\alpha e^{-k_4\sqrt{\frac{s}{\alpha}}}\right)\right) = \frac{\partial^2}{\partial k_4^2}\left(\frac{\alpha c_1 k_4}{2\sqrt{\alpha\pi t^3}} e^{-\frac{k_4^2}{4\alpha t}}\right) = \frac{\alpha c_1}{2\sqrt{\alpha\pi t^3}} e^{-\frac{k_4^2}{4\alpha t}}\left(-\frac{3k_4}{2\alpha t} + \frac{k_4^3}{4\alpha^2 t^2}\right) \quad \text{(A60)}$$

2nd term:

$$L^{-1}\left(c_2\sqrt{\frac{s}{\alpha}} e^{-k_4\sqrt{\frac{s}{\alpha}}}\right) = L^{-1}\left(\frac{\partial}{\partial k_4}\left(-c_2 e^{-k_4\sqrt{\frac{s}{\alpha}}}\right)\right) = \frac{\partial}{\partial k_4}\left(-\frac{c_2 k_4}{2\sqrt{\alpha\pi t^3}} e^{-\frac{k_4^2}{4\alpha t}}\right) = -\frac{c_1}{2\sqrt{\alpha\pi t^3}} e^{-\frac{k_4^2}{4\alpha t}}\left(1 - \frac{k_4^2}{2\alpha t}\right) \quad \text{(A61)}$$

3rd term:

$$L^{-1}\left(\frac{4\beta^2}{\alpha} e^{-k_4\sqrt{\frac{s}{\alpha}}}\right) = \frac{4\beta^2}{\alpha}\frac{k_4}{2\sqrt{\alpha\pi t^3}} e^{-\frac{k_4^2}{4\alpha t}} \quad \text{(A62)}$$

4th term:

$$L^{-1}\left(c_3 s^2 e^{-k_4\sqrt{\frac{s}{\alpha}}}\right) = L^{-1}\left(\frac{\partial^4}{\partial k_4^4}\left(c_3\alpha^2 e^{-k_4\sqrt{\frac{s}{\alpha}}}\right)\right) = \frac{\partial^4}{\partial k_4^4}\left(\frac{\alpha^2 c_3 k_4}{2\sqrt{\alpha\pi t^3}} e^{-\frac{k_4^2}{4\alpha t}}\right) = \frac{\alpha^2 c_3}{2\sqrt{\alpha\pi t^3}} e^{-\frac{k_4^2}{4\alpha t}}\left(\frac{15k_4}{4\alpha^2 t^2} - \frac{5k_4^3}{4\alpha^3 t^3} + \frac{k_4^5}{16\alpha^4 t^4}\right) \quad \text{(A63)}$$

5th term:

$$L^{-1}\left(c_4 s\sqrt{\frac{s}{\alpha}}e^{-k_4\sqrt{\frac{s}{\alpha}}}\right)=L^{-1}\left(\frac{\partial^3}{\partial k_4^3}\left(-c_4\alpha e^{-k_4\sqrt{\frac{s}{\alpha}}}\right)\right)=\frac{\partial^3}{\partial k_4^3}\left(-\frac{\alpha c_4 k_4}{2\sqrt{\alpha\pi t^3}}e^{-\frac{k_4^2}{4\alpha t}}\right)= \\ -\frac{\alpha c_4}{2\sqrt{\alpha\pi t^3}}e^{-\frac{k_4^2}{4\alpha t}}\left(-\frac{3}{2\alpha t}+\frac{6k_4^2}{4\alpha^2 t^2}-\frac{k_4^4}{8\alpha^3 t^3}\right) \tag{A64}$$

6th term:

$$L^{-1}\left(c_{15}s^3 e^{-k_4\sqrt{\frac{s}{\alpha}}}\right)=L^{-1}\left(\frac{\partial^6}{\partial k_4^6}\left(c_5\alpha^3 e^{-k_4\sqrt{\frac{s}{\alpha}}}\right)\right)=\frac{\partial^6}{\partial k_4^6}\left(\frac{\alpha^3 c_5 k_4}{2\sqrt{\alpha\pi t^3}}e^{-\frac{k_4^2}{4\alpha t}}\right)= \\ \frac{\alpha^3 c_5}{2\sqrt{\alpha\pi t^3}}e^{-\frac{k_4^2}{4\alpha t}}\left(\frac{105k_4^3}{16\alpha^4 t^4}-\frac{21k_4^5}{32\alpha^5 t^5}+\frac{k_4^7}{64\alpha^6 t^6}-\frac{105k_4}{8\alpha^3 t^3}\right) \tag{A65}$$

7th term:

$$L^{-1}\left(c_6 s^2\sqrt{\frac{s}{\alpha}}e^{-k_4\sqrt{\frac{s}{\alpha}}}\right)=L^{-1}\left(\frac{\partial^5}{\partial k_4^5}\left(-c_6\alpha^2 e^{-k_4\sqrt{\frac{s}{\alpha}}}\right)\right)=\frac{\partial^5}{\partial k_4^5}\left(-\frac{\alpha^2 c_6 k_4}{2\sqrt{\alpha\pi t^3}}e^{-\frac{k_4^2}{4\alpha t}}\right)= \\ -\frac{\alpha^2 c_6}{2\sqrt{\alpha\pi t^3}}e^{-\frac{k_4^2}{4\alpha t}}\left(-\frac{45k_4^2}{8\alpha^3 t^3}+\frac{15k_4^4}{16\alpha^4 t^4}-\frac{k_4^6}{32\alpha^5 t^5}\frac{15}{4\alpha^2 t^2}\right) \tag{A66}$$

These equations have to summed to obtain the solution for $L^{-1}(IxII)$. This ends up with the following equation, with $t''' = t - (4L + x)$

$$T_{I\times II}=H(t'')e^{-\frac{k_3^2}{4\alpha t''}}e^{-\frac{L-x}{\gamma}}\left(\gamma\frac{k_3}{2\sqrt{\pi\alpha t''^3}}+\frac{2\gamma\beta}{\sqrt{\alpha\pi t''}}+\frac{\gamma^2}{2\sqrt{\alpha\pi t''^3}}\left(-\frac{3k_3}{2t''}+\frac{k_3^3}{4\alpha t''^2}-4\beta+\frac{4\beta k_3^2}{2\alpha t''}+\frac{4\beta k_3}{\sqrt{\alpha}}\right)\right) \\ -H(t''')e^{-\frac{2L-x}{\gamma}}\gamma^2\frac{e^{-\frac{k_4}{4\alpha t'''}}}{2\sqrt{\pi\alpha t'''}}G(t''') \tag{A67}$$

With:

$$
\begin{aligned}
G(t) = &\left(-c_2 + \frac{3c_4}{2t} - \frac{15c_6}{4t^2}\right) + k_4\left(-\frac{3c_1}{2t} + \frac{4\beta^2}{\alpha} + \frac{15c_3}{4t^2} - \frac{105c_5}{8t^3}\right) \\
&+ k_4^2\left(\frac{c_2}{2\alpha t} - \frac{6c_4}{4\alpha t^2} + \frac{45c_6}{8\alpha t^3}\right) + k_4^3\left(\frac{c_1}{4\alpha t^2} - \frac{5c_3}{4\alpha t^3} + \frac{105c_5}{16\alpha t^4}\right) \\
&+ k_4^4\left(\frac{c_4}{8\alpha^2 t^3} - \frac{15c_6}{16\alpha^2 t^4}\right) + k_4^5\left(\frac{c_3}{16\alpha^2 t^4} - \frac{21c_5}{32\alpha^2 t^5}\right) \\
&+ k_4^6\left(\frac{c_6}{32\alpha^3 t^5}\right) + k_4^7\left(\frac{c_5}{64\alpha^3 t^6}\right)
\end{aligned}
\tag{A68}
$$

Finally we can obtain the full solution for the temperature (summing (A53) and (A67)since $T = T_{IxIII} + T_{IxII}$ giving:

$$
\begin{aligned}
T = &H(t-x)erfc\left(\frac{k_1}{2\sqrt{\alpha(t-x)}}\right) \\
&- H(t')e^{-\frac{L}{\gamma}}e^{-\frac{k_2^2}{4\alpha t'}}\left(\gamma\frac{k_2}{2\sqrt{\pi\alpha t'^3}} + \frac{2\gamma\beta}{\sqrt{\alpha\pi t'}} + \gamma^2\left(-\frac{3k_2}{2t'} + \frac{k_2^3}{4\alpha t'^2} - 4\beta + \frac{4\beta k_2^2}{2\alpha t'} + \frac{4\beta k_2}{\sqrt{\alpha}}\right)\right) \\
&+ H(t'')e^{-\frac{k_3^2}{4\alpha t''}}e^{-\frac{L-x}{\gamma}}\left(\gamma\frac{k_3}{2\sqrt{\pi\alpha t''^3}} + \frac{2\gamma\beta}{\sqrt{\alpha\pi t''}} + \frac{\gamma^2}{2\sqrt{\alpha\pi t''^3}}\left(-\frac{3k_3}{2t''} + \frac{k_3^3}{4\alpha t''^2} - 4\beta + \frac{4\beta k_3^2}{2\alpha t''} + \frac{4\beta k_3}{\sqrt{\alpha}}\right)\right) \\
&- H(t''')e^{-\frac{2L-x}{\gamma}}\gamma^2\frac{e^{-\frac{k_4}{4\alpha t'''}}}{2\sqrt{\pi\alpha t'''}}G(t''')
\end{aligned}
\tag{A69}
$$

APPENDIX B: FORTRAN CODE

This appendix contains the source code of a program that changes the material type of specified rock elements. This is necessary if one wishes to generate systems with different types of rock, e.g. not-stimulated and stimulated regions. So far the only way to change the element types was to toggle each element with the mouse, quite a time consuming job. This program should be used together with the mesh generator *level3_mesh.exe*. This program generates meshes as plotted on this page. Indicated in red is the first block, consisting of 52 elements. The program *rockchanger.f* enables the rock material of any of the blocks of the mesh to be changed. The blocks are counted starting from 1 at the bottom left up (plotted) to the last on the right top of the mesh. If three or more different materials need to be included in the mesh, this can be done by running the program several times and using the output of one run as the input of the next one.

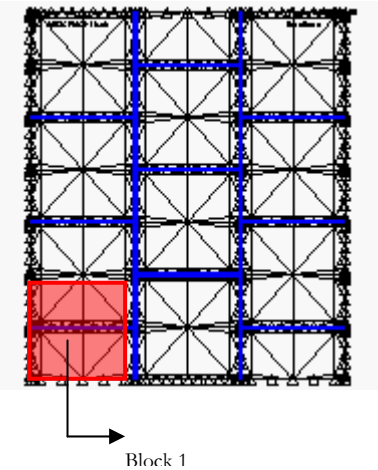


```
c23456    rockchanger.f, D. Coumou, Oct. 26, 00
      PROGRAM rockchanger
      IMPLICIT NONE
c-----------------------------------------------------------------------
c     DECLARATIES
c-----------------------------------------------------------------------
      double precision el,k1,k2,k3,k4,k5,k6,tf,mat,l,m,n
      double precision x,y
      integer Nelem,Nnodes,Ncontmat,Nfluidelem,i,j,knr
      integer nrblocks,blocknr(100),min(100),max(100)
      character*80 c80,t80
c-----------------------------------------------------------------------
c     OPEN FILES
c-----------------------------------------------------------------------
      print*,'Which file has to be changed, output to: output.f'
      read*,t80
      open(10, file = t80)
      open(20, file = 'output.geo')
```

```
c-----------------------------------------------------------------------
c                                                  INPUT          PARAMETERS
c-----------------------------------------------------------------------
      print*,'How many blocks would you like to change ?'
      read*, nrblocks
      print*,'Give the block numbers, counting from bottom-left to
top-
     .right.'
c-----------------------------------------------------------------------
c              DETERMINE   CORRECT   ELEMENT   NUMBERS   (max   &   min)
c-----------------------------------------------------------------------
      do i = 1,nrblocks
         print*,'number ',i,', please...'
         read*,blocknr(i)
         min(i) = (blocknr(i)-1)*52 + 1
         max(i) = blocknr(i)*52
      enddo
c-----------------------------------------------------------------------
c     READ, CHANGE & WRITE DATA
c-----------------------------------------------------------------------
      read(10,*) c80
      write(20,*) c80
      read(10,*) Nelem, Nnodes, Ncontmat, Nfluidelem
      Ncontmat = Ncontmat + 1
      write(20,*) Nelem, Nnodes, Ncontmat, Nfluidelem
      do  i = 1, Nnodes
          read(10,*) knr, x,y
          write(20,*)knr, x,y
      enddo
      do  j = 1, Nelem
          read(10,*) el,k1,k2,k3,k4,k5,k6,tf,mat,l,m,n
          do   i = 1, nrblocks
               If (el.LE.max(i) .AND. el.GE.min(i)) then
               mat = mat+1
               goto 200
               Endif
```

```
          enddo
200       write(20,*) el,k1,k2,k3,k4,k5,k6,tf,mat,l,m,n
      enddo
      end
```

APPENDIX C: MESHES

In both GEOCRACK2D and 3D, all elements consist of 6 nodes. Rock or continuum elements have a triangular shape. Fluid and interface elements are rectangularly shaped. The figures below show the nodal numbering and coordinate systems for respectively rock, interface and fluid elements {Swenson et al, 1997].

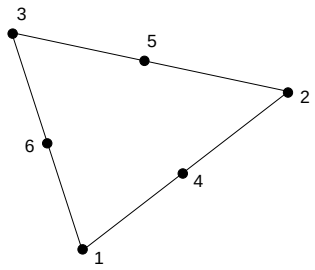

Fig. C.1: Rock element.

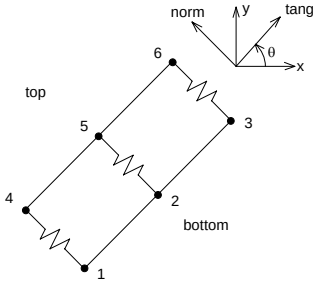

Fig. C.2: Interface element .

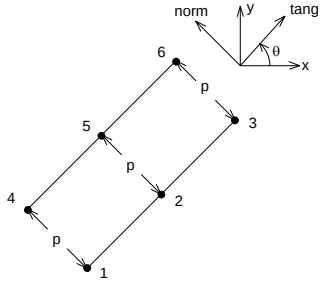

Fig. C.3: Fluid element.

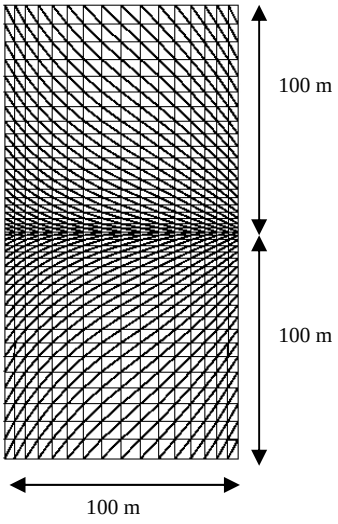

Several meshes have been used during the course of this research. The ones mentioned in the rapport (apart from the ones used for the Soultz-thermal reservoir, these can be found in Appendix E) are described below. Interface elements are indicated by small triangles. Fluid elements are plotted as thick black or yellow lines.

Fig. C4: (left) Single plane fracture, variable element size.
Δx_{min} = 4.2
Δy_{min} = 1.7
Δx_{max} = 8.3
Δy_{max} = 8.3

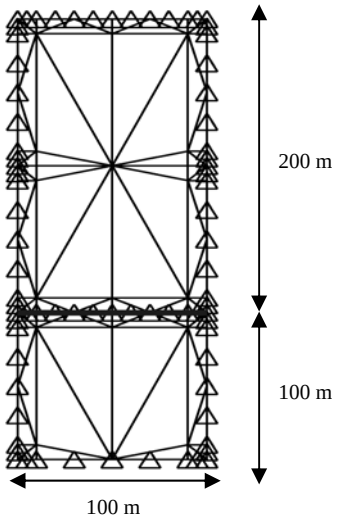

Fig. C5: (left) Single plane fracture, variable element size.
Δx_{min} = 10 m
Δy_{min} = 10 m
Δx_{max} = 40 m
Δy_{max} = 90 m

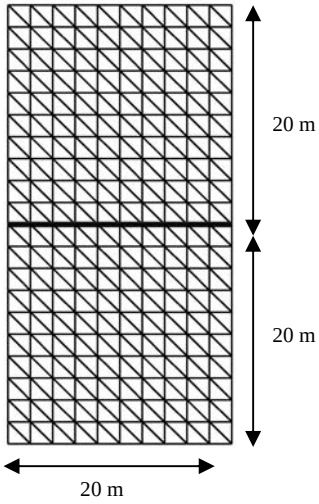

Fig. C6: (left) Single plane fracture, constant element size
$\Delta x_{min} = \Delta y_{min} = \Delta x_{max} = \Delta y_{max} = 2$ m

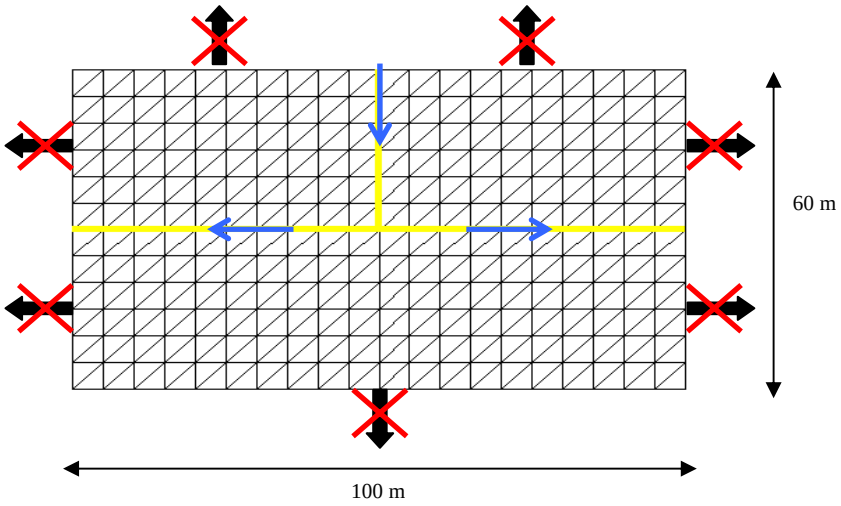

Fig. C7: (left) Splitting fracture, constant element size
$\Delta x_{min} = \Delta y_{min} = 5$ m
$\Delta x_{max} = \Delta y_{max} = 5$ m

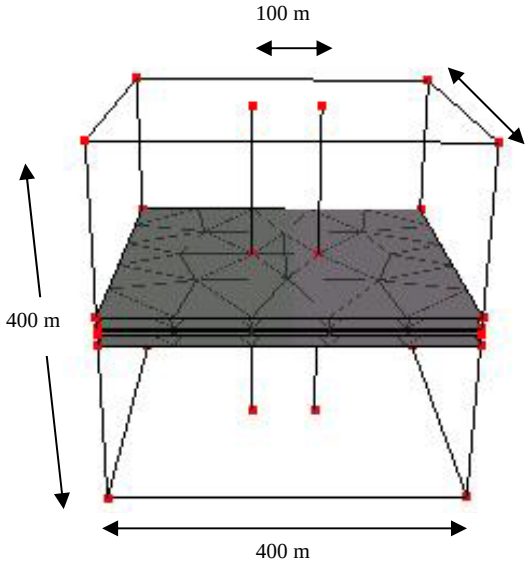

Fig. C8: 'Gringarten' system
Of the horizontal planes only the most centred one is a fracture (at z = 200m). The other three (at z = 180, 195, 205 and 220) are implemented to allow mesh refinement near the fracture. They do not contain any fluid transport.
$\Delta x_{min} = \Delta y_{min} = 5$ m
$\Delta x_{max} = \Delta y_{max} = 80$ m

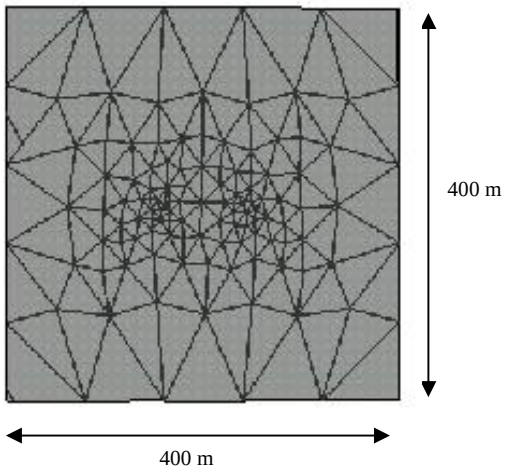

Fig. C9: Surface discretisation of fracture in system shown in figure C8.
$\Delta x_{min} = \Delta y_{min} = 5$ m
$\Delta x_{max} = \Delta y_{max} = 80$ m

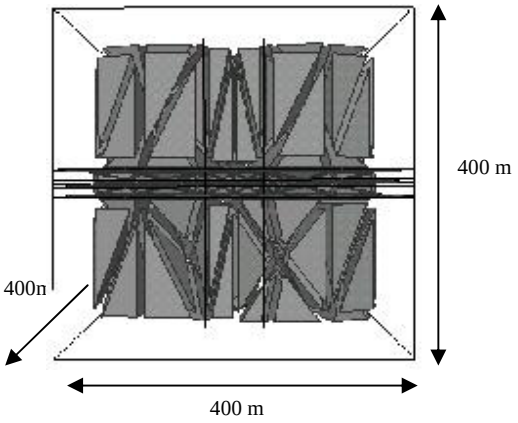

Fig. C10: Volume elements in system shown in figure C.8.
$\Delta x_{min} = \Delta y_{min} = \Delta z_{min} = 5$ m
$\Delta x_{max} = \Delta y_{max} = 80$ m
$\Delta z_{max} = 150$ m

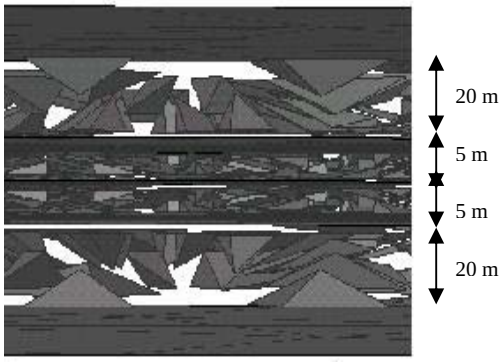

Fig. C.11: Close up of figure C.10. Mesh refinement of the volume elements.

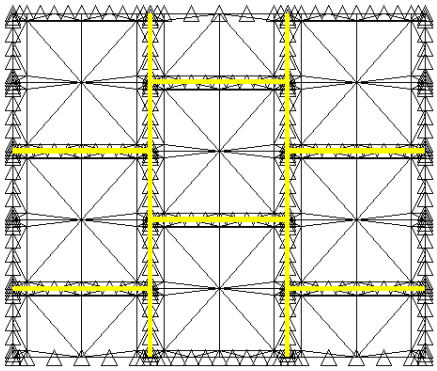

Fig. C.12:

APPENDIX D: IMPLEMENTATION

This appendix describes all proposed models in detail. First of all the exact geometry including fracture network and mesh discretisation is given. Further a table containing all standard parameters used in every test-run and a table with parameters with different values in each test-run are given. Finally the boundary conditions and the important relation between fracture opening and fracture stress are discussed.

Geometry

Horizontal Models

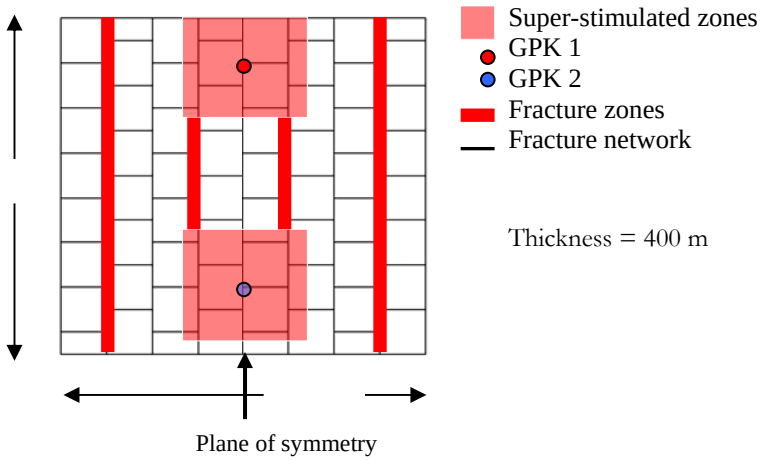

Fig. D1: Geometry of the horizontal models.

Vertical Models

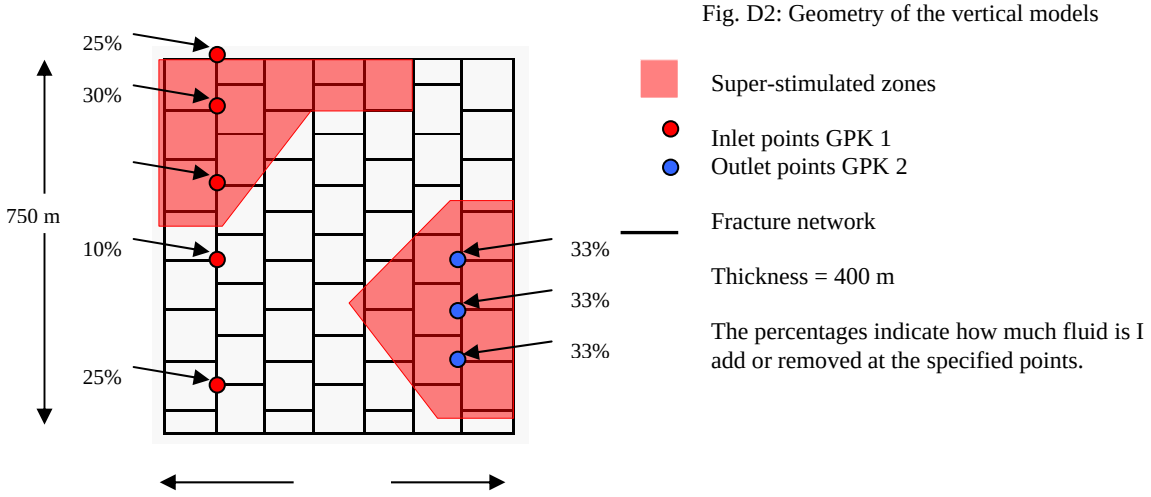

Fig. D2: Geometry of the vertical models

3D Models

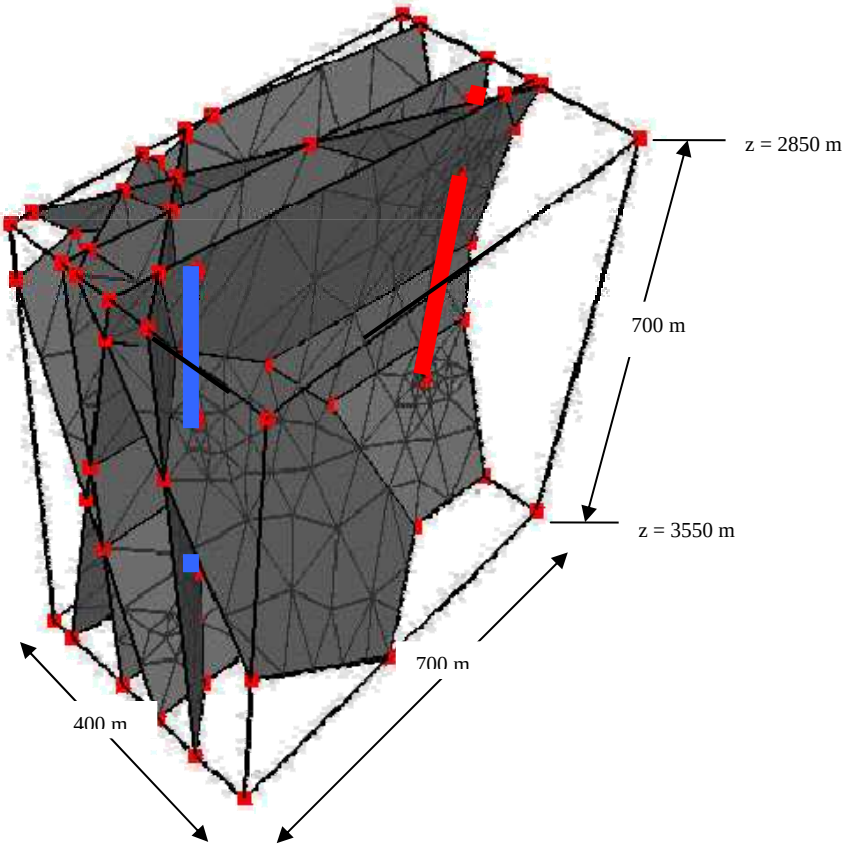

Fig. D3: 6 fracture model. Surface elements. The red and blue Lines respectively indicate the visible parts of GPK1 and GPK2.

Δh_{min} = 10m
Δh_{max} = 150m

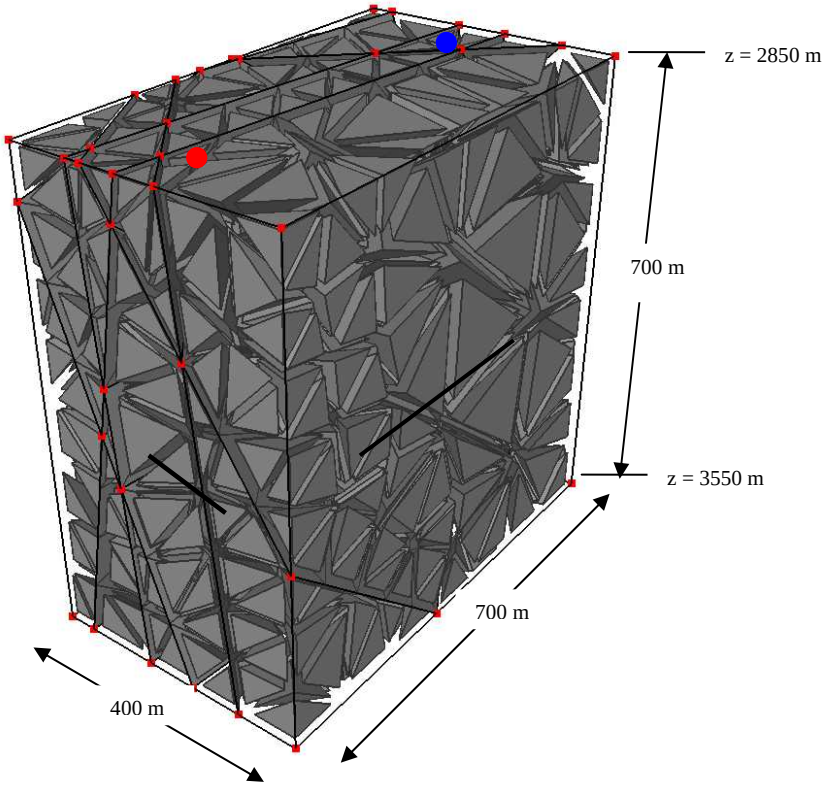

Fig. D4: 6 fracture model, volume elements. The red end blue dot indicate the wells of GPK2 and GPK1.

Mesh

Horizontal and vertical models have the same mesh discretisation. Below the mesh elements of one block bounded by four fractures is plotted. Fluid elements are indicated with yellow lines.

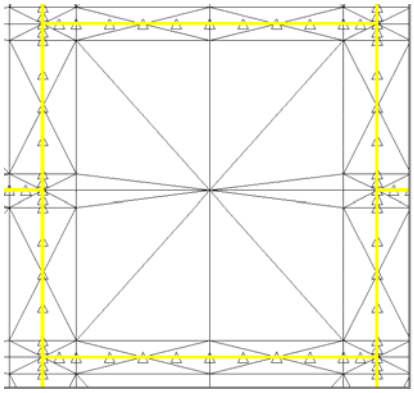

Fig. D5: Mesh of 2D models

Granite properties	Young's modulus E	67 Gpa
	Poisson ratio ν	0.28
	Density ρ	2660 kg/m^3
	Specific heat capacity c	1098 J/kgK
	Thermal conductivity λ	2.58 W/mK
	Thermal expansion coefficient β_T	$0.92 \cdot 10^{-5}$ K^{-1}
Fluid properties	Dynamic viscosity μ	$2.0 \cdot 10^{-4}$ Pa·s
	Density ρ	950 kg/m^3
	Specific heat capacity c	4300 J/kgK
	Thermal conductivity λ	0.66 W/mK
	Convection coefficient h	660
Mechanical properties (at 3200m)	Max. horizontal stress S_H	41.7 MPa
	Min. Horizontal stress S_h	82.2 Mpa
	Vertical stress S_Z	80.3 MPa
Thermal properties (at 3200m)	Initial temperature T	150 ^{0}C
	Vertical gradient $\partial T/\partial z$	$12.5 \cdot 10^{-3}$ K/m

Table D.1: Standard parameters (2D and 3D models).

	Parameters		Model		
			Non-permeable	*Constant permeability*	*Variable permeability*
Stimulated zone	Porosity		0 %	1.0 %	1.0 %
	Permeability		0 m^{-2}	1E(-17) m^{-2}	1E(-15) m^{-2}
	Fracture aperture		1.0 mm	1.0 mm	1.0 mm
Non-stimulated zone	Porosity		0 %	1.0 %	1.0 %
	Permeability		0 m^{-2}	1E(-17) m^{-2}	1E(-17) m^{-2}
	Aperture	Fracture zones	0.1 mm	0.1 mm	0.1 mm
		Fracture network	0.05 mm	0.05 mm	0.05 mm

Table D.2: Variable parameters (2D models).

Boundary conditions

- Structure: On the model boundaries interface elements were implemented. This gave the possibility to specify a finite maximum displacement instead of a totally fixed boundary. The maximum displacement was set to +/- 0.1 mm in all models.
- Temperature: $\partial T/\partial \chi = 0$ on all boundaries. At injection points the temperature was set to a constant value of 60 ^{0}C.
- Fluid: $q = 0$ on all boundaries unless otherwise specified (e.g. an injection or production point).

Relation fracture opening / fracture stress

GEOCRACK2D offers the possibility to define the joint opening / joint stress relation. This can either be done with a multi-linear curve or by the Gangi equation:

$$a = a_0 - a_{disp.} = a_0 - a_0\left(\frac{\sigma}{\sigma_c}\right)^m$$

With a_0 the zero-stress fracture opening, σ the effective stress and σ_c the critical stress at which the fracture is assumed to be closed, and m the Gangi constant. The correct value of these parameters was one of the main difficulties of the implementation part. After several discussions with G. Siddiqi, the following points appeared to be reasonable:

- Fractures mechanically grow maximally by one 10th of their original aperture before tip propagation occurs
- To completely close a fracture, a nearly infinite stress is needed, due to the roughness of fracture surfaces.
- The relation between fracture opening and fracture stress is non-linear. When joints close they become more stiff, when they open they become softer.

Based on these points, it has been decided to use the Gangi model with the following parameters:

m = 0.33

σ_c = 500 Mpa

The value of a_0 is given in the table above.

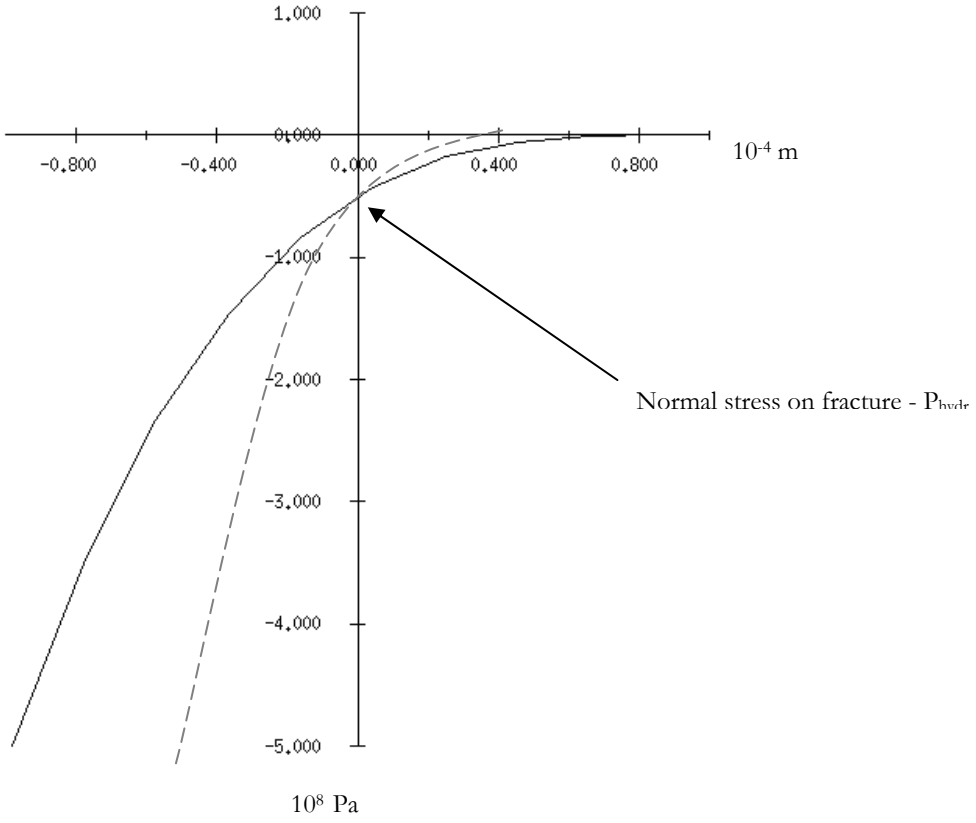

Fig. D6: Gangi's fracture opening / fracture stress relation. Dotted line: m = 0.166 (used for sensitivity analyses).

APPENDIX E: NOTES ON GEOCRACK2D

This appendix contains useful practical information on the use of GEOCRACK2D. As this finite element code is continuously under (re) construction, several strange things can happen. During the research two different GEOCRACK executables have been used, one with a Standard Galerkin (SG) iteration scheme (compiled march 1997) and one with a Petrov-Galerkin (PG) solver (compiled May 2000). The numeric artefacts of these different solvers are discussed in § 5.4. Another major difference between the two executables is the possibility in the PG-version to implement porous flow through the rock. The list below contains bugs and peculiarities of the two executables. It can be useful for future researchers using GEOCRACK.

1. Dimensions (PG & SG).

   Both manual and program-menu do not clarify which dimensions to use for the parameters. In general parameters should be implemented according to SI-units. This is not the case for temperature; all temperature units are ^{0}C. Time dependent parameters should all be set with the same time unit (s/hours/days/years). Time dependent GEOCRACK-parameters are:

   - $[\lambda_R, \lambda_F] = J/sm^0C$ (conductivity)
   - $[\mu] = Pa\ s$ (dynamic viscosity)
   - $[\beta] = J/sm^2kg$ (convection coefficient)

2. Adding elements (PG & SG).

   When elements need to be added, one needs to start with a 'clean' mesh. This means it is not possible to add elements in a restart file. If one attempts this, problems will occur, probably due to problems in the counting of elements.

3. Adding fluid and/or interface elements (2) (Pg)

   Several times I have been confronted with strange behaviour in GEOCRACK when implementing fluid or interface elements. Sometimes, after adding a certain number of elements, it does not want to add any new ones or the elements are placed at a completely different location to that desired.

4. Stress-field (PG & SG).

   One cannot turn off the stress-field. If ones wishes to do tests in which the aperture of the fracture is constant (e.g. Lauwerier problem) it is best to implement no-displacement boundary conditions on the nodes on the two fracture edges. To do this, one needs to separate the nodes first (menu: *pre-process/drag node*), then fix both edges (menu: *pre-process/boundary conditions/structure/edge displacement*) and finally overlay the nodes again (menu: *pre-process/drag node*).

5. Porous-flow plotting (PG).

   The program crashes when trying to plot porous-flow with directional arrows when the porous flow through the medium is zero. When you have implemented two rock types, one porous and one non-porous, plotting of the porous flow is not possible either.

6. λ_F (PG).

   The fluid conductivity cannot be set to zero. This is not the case for the SG-version.

7. Node info (PG).

   Both executables contain the possibility to print on the screen information about a specified node (*main menu/node info*). In the PG-version this function gives incorrect node-numbers. If it is desired to monitor a node, one can find the correct node number in the data file, or one must open the file in the SG-version.

8. Node numbers (PG).

   Another button (*main menu/node numbers*) plots all node numbers (correctly) on the screen, next to its location. In the PG-version this button cannot be turned off, resulting in the forced execution of the program.

9. Monitoring displacements (SG & PG).

   Monitored values of node displacements (menu: *plot/structure/monitor*) cannot be saved in a data file, whereas this is possible for monitored values of the flow rate or temperature.

10. Monitoring flow rates (PG).

    When using meshes generated with *level3_mesh.exe*, only nodes located on the mesh edges can correctly be monitored for flow rates. Nodes located on the fractures inside the system give unrealistic results when monitored.

11. Tracer analyses (PG).

    With the PG-version presently no tracer-calculations can be performed (menu: *pre-process/tracer/*).